

## INFORMATION TO USERS

This reproduction was made from a copy of a document sent to us for microfilming. While the most advanced technology has been used to photograph and reproduce this document, the quality of the reproduction is heavily dependent upon the quality of the material submitted.

The following explanation of techniques is provided to help clarify markings or notations which may appear on this reproduction.

1. The sign or "target" for pages apparently lacking from the document photographed is "Missing Page(s)". If it was possible to obtain the missing page(s) or section, they are spliced into the film along with adjacent pages. This may have necessitated cutting through an image and duplicating adjacent pages to assure complete continuity.
2. When an image on the film is obliterated with a round black mark, it is an indication of either blurred copy because of movement during exposure, duplicate copy, or copyrighted materials that should not have been filmed. For blurred pages, a good image of the page can be found in the adjacent frame. If copyrighted materials were deleted, a target note will appear listing the pages in the adjacent frame.
3. When a map, drawing or chart, etc., is part of the material being photographed, a definite method of "sectioning" the material has been followed. It is customary to begin filming at the upper left hand corner of a large sheet and to continue from left to right in equal sections with small overlaps. If necessary, sectioning is continued again—beginning below the first row and continuing on until complete.
4. For illustrations that cannot be satisfactorily reproduced by xerographic means, photographic prints can be purchased at additional cost and inserted into your xerographic copy. These prints are available upon request from the Dissertations Customer Services Department.
5. Some pages in any document may have indistinct print. In all cases the best available copy has been filmed.

**University  
Microfilms  
International**

300 N. Zeeb Road  
Ann Arbor, MI 48106



8224230

Lowry, Mark E.

MAGNETIC RESONANCE STUDIES OF REACTIVELY SPUTTERED  
AMORPHOUS SILICON-HYDROGEN ALLOYS

*Iowa State University*

PH.D. 1982

University  
Microfilms  
International 300 N. Zeeb Road, Ann Arbor, MI 48106

Copyright 1982

by

Lowry, Mark E.

All Rights Reserved



Magnetic resonance studies of reactively sputtered  
amorphous silicon-hydrogen alloys

Mark E. Lowry

A Dissertation Submitted to the  
Graduate Faculty in Partial Fulfillment of the  
Requirements for the Degree of  
DOCTOR OF PHILOSOPHY

Department: Physics  
Major: Solid State Physics

Approved:

Signature was redacted for privacy.

In Charge of Major Work

Signature was redacted for privacy.

For the Major Department

Signature was redacted for privacy.

For the Graduate College

Iowa State University  
Ames, Iowa

1982

Copyright© Mark E. Lowry, 1982. All rights reserved.

"The Government has reserved for itself and for others acting on its behalf, a royalty-free, non-exclusive, irrevocable, world-wide license to publicly distribute and translate, duplicate, exhibit and perform any data copyrighted by the contractor."

## TABLE OF CONTENTS

	Page
DEDICATION	vi
I. INTRODUCTION	1
A. The Growth of Amorphous State Research	1
B. Disorder in the Amorphous State Defined	2
1. Long-range disorder	3
2. Short-range disorder	3
3. Topological disorder	3
4. Quantitative disorder	4
5. Chemical disorder	4
6. Intermediate-range disorder--inhomogeneity	4
7. General remarks on disorder	5
C. Electronic and Nuclear Structure of Amorphous Semiconductors	6
1. Energy bands and extended electronic states	6
2. Electron localization: The Anderson theorem	7
3. The density of electronic states distribution in the presence of disorder	8
4. Charge transport, the DES distribution, and Fermi level pinning	11
5. Electron correlation effects and Fermi level pinning	14
D. Hydrogen Alloyed with the Tetrahedrally Coordinated (group IV) Amorphous Semiconductors: a-Si(H) and a-Ge(H)	15
E. Magnetic Resonance Studies of a-Si(H)	23
1. Electron Paramagnetic Resonance (EPR) studies	23
2. EPR under conditions of sample illumination	25
3. Nuclear Magnetic Resonance studies of a-Si(H)	27
II. MAGNETIC RESONANCE THEORY	30
A. Fundamental Theory: Isolated Spins	31
B. Classical Precession: The Transition Process from the Classical Point of View	33

	Page
C. The Quantum Mechanical Description of the FID Experiment	39
D. The Interaction of the Spin System with its Surroundings: Density Matrix Formalism	46
E. The FID and Adiabatic Slow Passage Experiments	55
F. Relaxation of the Magnetization: Beyond the Bloch Equations	57
III. EXPERIMENTAL METHODS	64
A. Sample Preparation	64
1. Sputtering parameters	64
2. Bulk sample preparation	65
3. Documentation of contamination levels	67
B. The Magnetic Resonance Probe	68
1. The quality factor (Q) of the probe	68
2. The pulse NMR probe	68
3. The EPR probe	71
C. Pulse NMR Experimental Techniques	72
1. The spectrometer	72
2. The FID as a magnetization sampler: Bionic	76
3. The FID as a source of lineshape information: Alvin	79
4. Temperature variation, control, and measurement	81
5. Sources of error: Field inhomogeneities, instabilities, and sensitivity	86
D. Continuous Wave EPR Experimental Methods	89
1. The ASP experiment	89
2. EPR spin counting	95
3. EPR spin-lattice relaxation time estimations	96
4. Temperature variation and control	98
5. Sources of error: Microwave frequency instability, errors in Zeeman field strength and field inhomogeneity	99

	Page
IV. RESULTS AND DISCUSSION	101
A. NMR Results	101
1. FFT absorption lineshapes	101
2. Proton NMR spin-lattice relaxation times	131
B. EPR Results	163
1. Narrow scan EPR results	163
2. Wide scan EPR results	171
V. CONCLUSIONS, ANOMALOUS RESULTS, AND SUGGESTIONS FOR FUTURE WORK	184
A. Summary	184
B. Consequences for Transport Measurements and Device Properties	185
C. New Directions	186
VI. LITERATURE CITED	189
A. Experimental Works: Sample Preparation, General Structural Determinations and Transport Measurements of Amorphous Semiconductors (Mostly Group IV)	189
1. Sample preparation, infrared absorption, x-ray diffraction, Photoluminescence, Conductivity, Photoconductivity, Field Effect, Optical Absorption, and sundry methods of determining the electronic and nuclear structure of amorphous semiconductors	189
2. Magnetic Resonance Spectroscopies applied to amorphous semiconductors	192
B. Amorphous Materials: Models, Theory, and Philosophy	194
C. Communications Dealing with or Relating to Devices Made from Amorphous Semiconductors	196
D. Review Articles and Books Dealing with Amorphous Semiconductors	198
E. Fundamental Solid State Physics References	198



	Page
F. References Related to the Theory of Magnetic Resonance	199
G. Magnetic Resonance Experimental Methods References	199
H. Miscellaneous Magnetic Resonance and Amorphous Materials References	200
VII. ACKNOWLEDGEMENTS	202
VIII. APPENDICES	204
A. Thin Film Deposition Techniques for Amorphous Silicon- hydrogen Alloys [a-Si(H)]	204
1. Reactive Sputtering (RS)	204
2. Glow Discharge (GD)	208
3. Chemical Vapor Deposition (CVD)	208
4. Evaporation	209
5. Ion plating	209
B. Mass Spectroscopic Analysis of Several RS a-Si(H) Samples	209
C. Results of the Nonexponential Spin-lattice Relaxation Analysis	213

DEDICATION

To my Grandfather Tysdal, whose inquiring mind and patient diligence have always influenced me, and to his wife, my Grandmother, who has never ceased to encourage me in my academic pursuits . . .

To my Mother and Blaine, who have believed in me throughout and have given me the strength of character to persevere . . .

## I. INTRODUCTION

Gaining understanding of the structure and physical properties that characterize the amorphous state of condensed matter may advance one of the last frontiers of fundamental knowledge in solid state physics. The amorphous state occupies a unique position in the phase spectrum of condensed matter: that nebulous region between the two extremes of the perfect crystal and the liquid. This disordered solid state has many properties that approach those of the crystal, yet its interatomic ordering more closely resembles that of a "snapshot" taken of the liquid. Only recently have these twilight phases of condensed matter fallen under much successful scrutiny; it is somewhat ironic, albeit understandable, that the disordered phases of the solid, which are by far Nature's most abundant, are also the last to give up their secrets.

### A. The Growth of Amorphous State Research

The amorphous state is yielding to the efforts mounted by investigators from often diverse fields. Experimentalists with backgrounds in solid state physics, chemistry, metallurgy, and many engineering disciplines have recently joined forces to characterize the nuclear and electronic structure, and physical properties of amorphous materials (1-83). Theorists, too, have recently shown much interest in the physical phenomena unique to the amorphous state (84-116). It must be pointed out that most of this work would not have been carried out had it not been for the promise and demonstration of exciting practical device applications for many amorphous materials (117a-139c). With the perception by many in

the scientific community that the world energy crisis was with us to stay, came an intensified resolve to produce an inexpensive large-area solar photovoltaic energy converter. As we shall see, the possibility that this could be realized with the use of amorphous materials may have been the single most important motivation behind the surge of interest in answering the questions posed by disorder.

The total amount of such work extant in the literature is staggering (the references cited here are merely those few which have a direct bearing on the present work), often confusing, and sometimes contradictory. Fortunately there are a number of good reviews and books (140-150) which serve to put much order into an often "disordered" literature. A reasonable measure of recent progress made, particularly in the subfield of amorphous semiconductors, can be obtained by comparing an early review article due to Brodsky (142) to the recent and authoritative review book (149) edited by him.

#### B. Disorder in the Amorphous State Defined

The presence of long-range periodic structure, characteristic of the perfect crystal, simplifies the quantum mechanical problem immensely (151-154). This simplification accounts for much of the success enjoyed by solid state physics investigations of crystalline material. The obvious question that arises is: How much of traditional solid state theory may one salvage in order to explain the phenomena unique to the disordered state? To answer this question and to facilitate accurate discussions of structural characterization of these materials it is necessary to define and classify disorder.

### 1. Long-range disorder

In a perfect crystal in the ground state every attribute of the material is periodic. Quantitatively, any property, say  $F$ , which is a function of position,  $\vec{r}$ , obeys the following prescription (147):

$$F(\vec{r}) = F(\vec{r} + \vec{l}) , \quad (1)$$

where  $\vec{l}$  is a lattice vector. In the presence of long-range disorder this great simplification does not hold at all over large  $\vec{l}$ .

### 2. Short-range disorder

In the presence of short-range disorder Equation 1 above does not hold for arbitrarily small  $\vec{l}$ . Most amorphous materials of interest here do have short range order, i.e. Eq. 1 approximately holds for  $\vec{l}$  sufficiently small.

### 3. Topological disorder

Topological order presumes that there exists a set of vectors,  $\vec{l}$ , in Eq. 1 above that describe a network, not necessarily a "lattice" in the crystalline sense, such that for each point in the network there exists the same number of vectors,  $\vec{l}$ . Topological order then describes a network in which each component (molecule or atom) is "connected" to the same number of other components. This sense of "connectivity" is usually physically realized by covalent bonding. An example of topological disorder would be the absence of this connectivity exemplified by the dangling bond in Fig. 1. A word of warning: The phrase "topological disorder" often appears in the literature used in the sense of what is called here topological order; we shall not use the phrase in that confusing sense.

#### 4. Quantitative disorder

Quantitative disorder describes the distribution in length and angle of the set of vectors,  $\vec{l}$ , in Eq. 1 for nearest neighbors. It then is a measure of bond stretching and bond bending in a perfectly topologically-ordered network (sometimes called a continuously-connected random network or CRN).

#### 5. Chemical disorder

This describes the situation most often realized in alloys, where the bonding of the network is disrupted by the inclusion of some "impurity." In the case of substitutional chemical disorder the impurity does not affect the topological order of the network in the sense of disruption of the connectivity, however the kind of connectivity is now disordered. If the impurity is not of the same chemical valence as the host then, of course, real topological disorder results.

#### 6. Intermediate range disorder--inhomogeneity

This type of disorder is the most common, yet the most difficult to precisely define. Inhomogeneity in the order of a material on the scale of many interatomic spacings is intermediate-range disorder. A material which is an aggregate such as concrete has much intermediate-range disorder, if one looks at small enough regions the material may look locally homogeneous. An example of this kind of disorder will be given later for the case of amorphous silicon hydrogen alloys.

## 7. General remarks on disorder

Disorder is mainly the absence of symmetry. Long-range disorder is the absence of the translational symmetry of Eq. 1. Topological disorder is the absence of the symmetry of local connectivity. In the ideal covalently bonded glass or amorphous CRN topological symmetry is preserved, long-range translational symmetry is not. This distinction will prove to be an aid in understanding many aspects of the physics of amorphous materials compared to the well-understood physics of their crystalline counterparts; to see this, one may reflect upon the great role symmetry has played in condensed matter physics (154).

An interesting phenomenological classification of disordered material exists in the work done on the entropy of disordered solids by Johari (107). He considers three classes: Glasses that are vitrified by supercooling from a melt, those that are created by supercooling an orientationally disordered crystal (quantitatively disordered in the present vernacular) below the disorder-order transition temperature, and those that are formed by some kind of vapor deposition onto a cool substrate. This work is concerned primarily with material in the last category.

Occasionally, in the literature, there is a distinction made between "glassy" and "amorphous" materials. This distinction holds that true glasses have the interatomic orientation and bonding of the liquid state and are "solid" by virtue of extremely high viscosity; while the amorphous state is characterized by the same covalent bonding as the crystal with quantitative disorder in the bonding. This distinction is not often accepted any more and will not be used here. Glassy and amorphous will be

used interchangeably. It should be recognized, however, that most disordered materials are indeed metastable (107). This metastability implies a very long time constant for "nonexcited" structural change in most cases and is not readily describable by a viscosity.

Finally, this section on disorder is by no means an exhaustive survey of the current ideas. A reference with a decidedly mathematical, but not obscure, bent is to be found in the very complete recent work by Ziman (151). Other works from complementary points of view are those of Waseda (150), Kramer and Weaire in ref. (149), and Mott and Davis (148).

### C. Electronic and Nuclear Structure of Amorphous Semiconductors

#### 1. Energy bands and extended electronic states

Among the physical phenomena that characterize the amorphous semiconducting state are two that are of particular physical interest and much practical concern. They are, respectively, the existence of thermally activated extended state electronic band transport and the coexistence of localized electronic states. It is surprising that the extended electronic band states are permitted in a disordered material; while the existence of localized states seems quite appropriate, though detrimental to device electronic transport.

In the elementary theory of the solid state one learns, for instance from the "tight binding" approximation (151-153), that when individual atoms are brought together in close enough proximity to form a solid, the otherwise discrete atomic levels become a continuous band (in the limit of an infinite cluster of atoms). There is no assumption in this model which



precludes the amorphous state forming electronic energy bands. However, an extended state requires a periodic potential, via the Bloch theorem (152). Further, the existence of a band gap in the usual sense (necessary for thermally activated conduction) is predicated upon there being long range order in the material; the long range order is necessary for the internal Bragg reflections of the electrons which set up the energy gap (153). It would seem that the traditional theories of solid state physics are at odds with the observed behavior of some amorphous solids.

## 2. Electron localization: The Anderson theorem

Anderson (84) was the first to address this dilemma from the theoretical side. In his now famous paper is found the theoretical groundwork of the theory of electronic states in disordered materials. Therein is addressed the question of how far one may relax the requirement of periodicity and still be permitted extended states; or, turning the question around, as disorder is increased at what point do these extended states begin to localize? His characterization of that point is called the Anderson criterion. There have been many recent contributions to the problem of Anderson localization (for a review see Kramer and Weaire in ref. 149, Ziman (147) is also helpful). Unfortunately, there is no universal agreement on either the precise type or amount of randomness that is required to induce Anderson localization; this remains an area of spirited theoretical work.

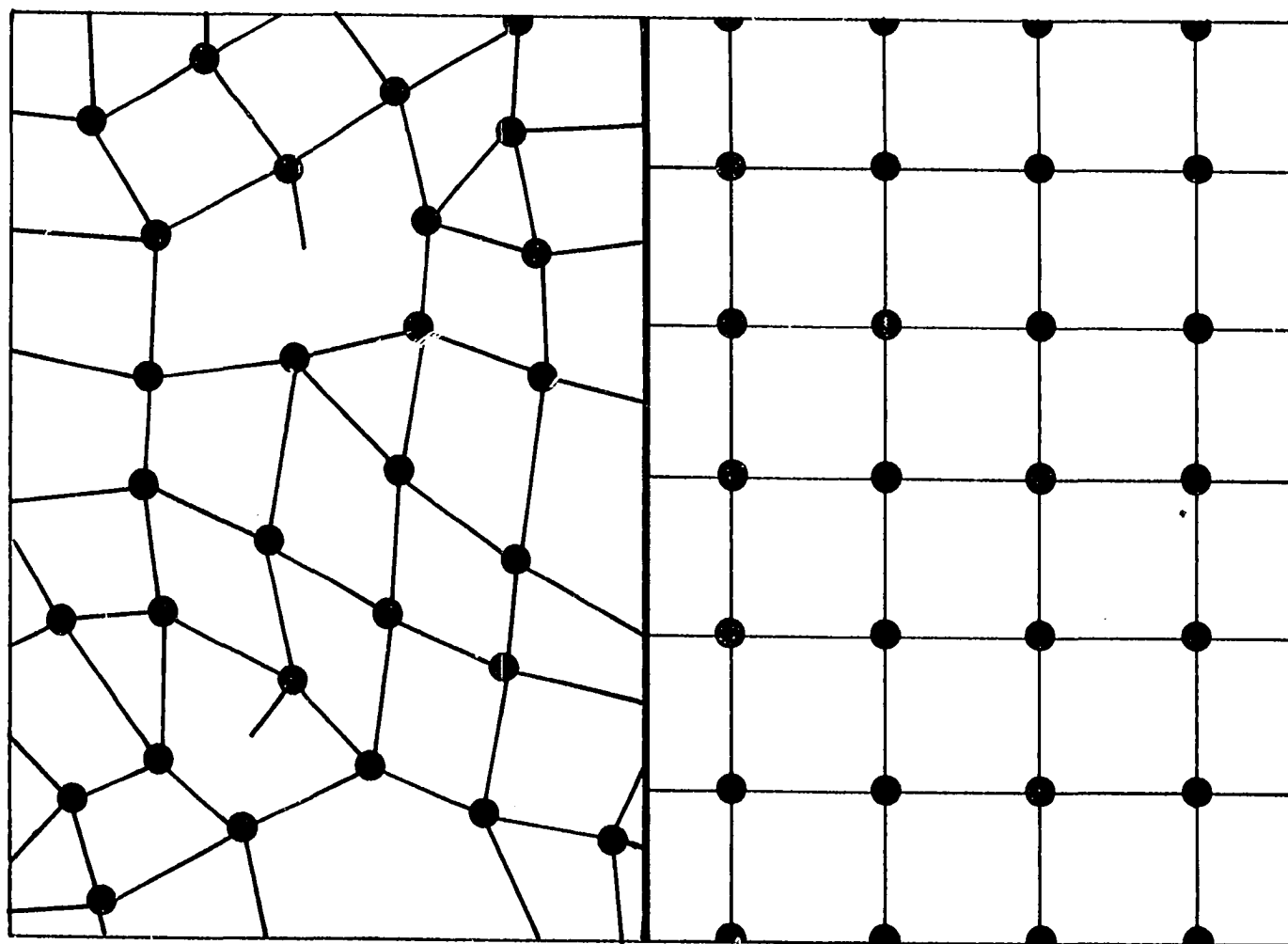
### 3. The density of electronic states distribution in the presence of disorder

It is generally agreed (147-149) that, somehow, randomness of the potential seen by the electrons leads to localized states whose energies fall in the semiconducting energy gap (or more properly--mobility gap), see Fig. 2a. As the disorder is increased the tails of these localized states presumably begin to "fill in the gap." It is easy to understand the tailing of the bands into the gap on very general grounds. A fundamental result of group theory (154) requires that the spatial symmetry of the potential term in the Schrodinger equation lead to degeneracies in the solutions. As the symmetry of the potential decreases (through quantitative disorder, for instance) the degeneracies are lifted, producing a spread or tailing of the energy distribution of states. That these states become localized requires much more strenuous effort to understand; at this point it becomes necessary to invoke the localization theory of Anderson. Localization at the band edges, producing the famous "mobility gap," is discussed thoroughly in the literature (147-149). The above cursory argument for band tailing on the basis of quantitative disorder is supported by more sophisticated reasoning (101, 108).

The density of electronic states (DES) distribution that has so far been described was historically the first DES model for amorphous semiconductors, put forward by Cohen, Fritzsche, and Ovshinsky (CFO) (85). There exists another type of localized state that occurs deep in the gap. These are states due to some sort of drastic disruption of topological order such as the dangling bond of Fig. 1. That these would lie deep in

Fig. 1. Disordered and Crystalline networks are compared

- (a) Here is a schematic two-dimensional representation of a real 4-fold coordinated amorphous network, of which a-Si is an example. The two "dangling bonds" shown are instances of topological disorder in the CRN. The various bond lengths and angles are manifestations of quantitative disorder. See text for details
- (b) The analogous perfect crystal network (or lattice) is shown for comparison



(a)

(b)

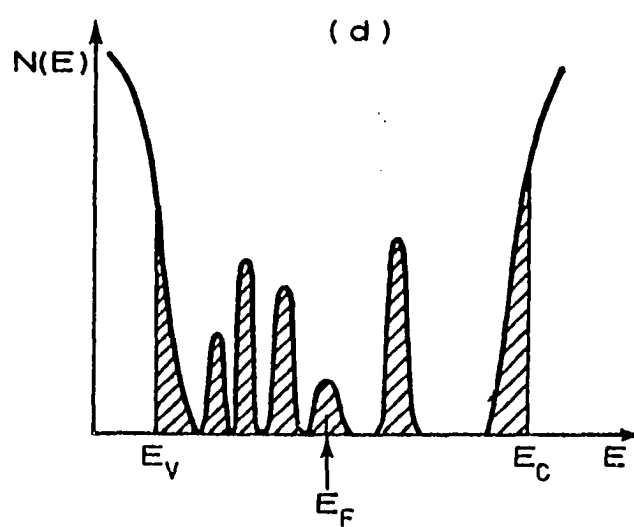
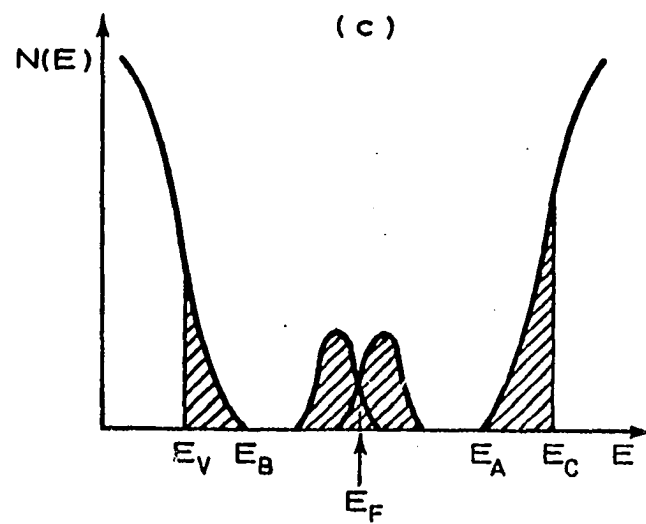
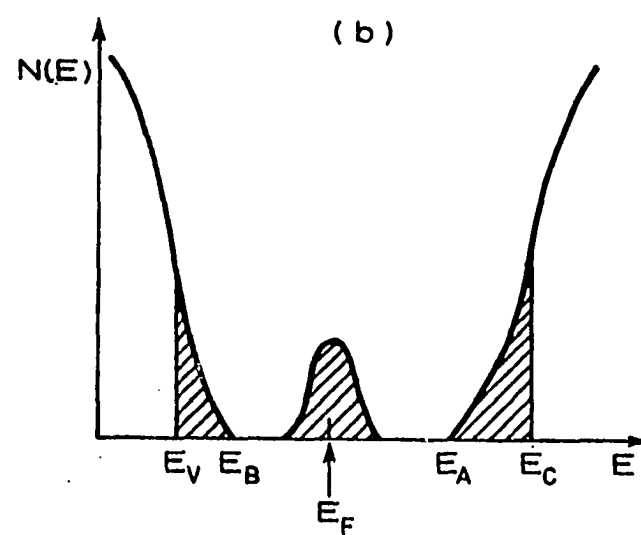
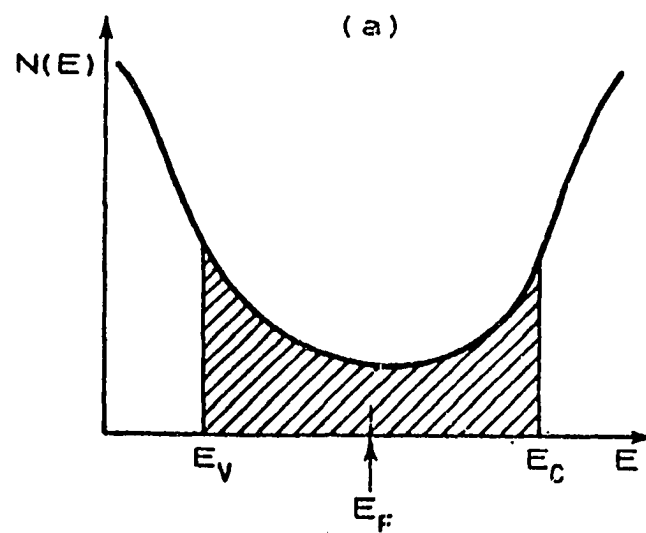
the gap is not surprising. One can visualize the band structure in terms of bonding orbitals (valence band) and antibonding orbitals (conduction band). As the separation between the nuclear centers of the bond increases the energy difference between the bonding (singlet) and antibonding (triplet) states decreases, until finally the bond is broken and the energies of the resulting dangling bonds fall at the gap center. This additional type of localized state was first introduced by Davis and Mott (P. Nagels in ref. 149 and Fig. 2b) and later modified by allowing the defects to become charged (88), Fig. 2c. Finally, the precise energies of these defect center states will depend on the local structural details of the defect. Therefore, in real amorphous semiconductors, especially group IV, the accepted picture of the DES distribution is given in Fig. 2d which depicts several deep distributed levels (148, 149).

#### 4. Charge transport, the DES distribution, and Fermi level pinning

In the currently accepted DES model there are three types of states: those outside of the mobility gap are the traditional extended Bloch-like states, those in the band tails are Anderson localized states, and finally those in the deep levels are localized states much like impurity bands. Each of these three kinds of electronic states have transport effects that are unique. Transport in the extended states is the traditional Boltzmann activated conductivity (152, 153); while transport in the localized states occurs via electron hopping. The band tail states conduct through the mechanism of thermally activated hopping (see P. Nagels in 149) and in the deep states transport proceeds via variable range hopping at the Fermi level (148). Each of these mechanisms has a different temperature

Fig. 2. (adapted from ref. 149) This depicts the historical progression of models dealing with the "energy gap" in amorphous semiconductors (all shaded regions denote localized states):

- (a) The CFO model. Here the idea of the "mobility gap,"  $E_{mg}$ , first surfaced. The mobility gap is defined as the minimum excitation energy necessary to produce extended state carriers - here  $E_{mg} \equiv E_c - E_v$
- (b) The discovery of an appreciable optical gap,  $E_{og}$ , prompted this modification. The band tails (of localized states) are thought to arise from quantitative disorder in the network. The distribution of DES in the gap center is due to dangling bonds
- (c) If the dangling bonds are allowed to become charged the distribution at center gap splits into two bands (much like donor and acceptor bands)
- (d) Finally, this model recognizes the possibility of defects with drastically differing local environments; hence, several levels deep within the gap are permitted. See text for details



dependence and it is possible to see each of the mechanisms in the appropriate temperature range (148, 149). The variable range hopping at the Fermi level can be a pronounced effect when there is a large DES there; this is the case with appreciable concentrations of dangling bond type defects in the CRN. These large concentrations of defects effectively pin the Fermi level coincident with the defect level. Material with an intrinsically pinned Fermi level is virtually useless for most device applications, since junctions with the necessary band bending can not be formed. There are other mechanisms of Fermi level pinning that don't require a large dangling bond concentration; they will be discussed shortly.

#### 5. Electron correlation effects and Fermi level pinning

Finally, any current discussion of electronic properties in disordered materials should include a few words about electron correlation. Intersite correlation has been shown by Pollak and Knotek (104) to be an extremely helpful concept in the understanding of AC hopping conductivity, while intersite correlation has profound implications for the doping characteristics (Fermi level moment) of amorphous semiconductors. Localization of carriers can also come about as a result of a Mott transition in electron occupancy, which results when correlation energies become comparable to the bandwidth (148).

The deep levels discussed above and depicted in Fig. 2d are assumed to be described by a positive effective Hubbard correlation energy,  $U$  (intra-site correlation). Basically, this means that it is energetically favorable for electrons with energies in the gap to remain unpaired, i.e. in the case of the dangling bond the defect remains chargeless and has a free spin. Beginning with another important paper due to Anderson (86) the notion of a negative  $U$  (brought about by local structural deformations, that favor the



pairing of electrons) had gained acceptance for the case of chalcogenide glasses (87,89b,94,148,149). The negative U concept is still a matter of some controversy for the group IV semiconductors, mainly because the ubiquitous dark electron paramagnetic resonance (EPR) naturally favors unpaired electrons. However, the weight of current work (30,94,93,95,102, 113,57) is in favor of negative U electronic correlation also existing in the tetrahedrally coordinated amorphous semiconductors. The presence of negative U correlation effects has been demonstrated by Adler and Yoffa (89a) to be remarkably effective at Fermi level pinning. An interesting discussion of this effect is given by Davis in ref. 149.

It is hoped that this short discourse on the electronic structure of amorphous materials has demonstrated that: topological disorder in the network of nuclear centers has important consequences for deep localized electronic levels; while the effects of quantitative nuclear disorder are manifested by localization at the band edges. Thus it obtains that details of the nuclear network structure have a very direct bearing upon the device properties of these materials.

#### D. Hydrogen Alloyed with the Tetrahedrally Coordinated (group IV) Amorphous Semiconductors: a-Si(H) and a-Ge(H)

It was perhaps the demonstration by Ovshinsky (117b) of switching effects in chalcogenide glasses that initiated the current interest in amorphous semiconductors as electronic device materials (these switching effects have been considerably refined of late (139a)). Subsequent to Ovshinsky's efforts, attempts were made to dope the chalcogenides. This

was unsuccessful, and the currently understood reason lies with the presumed negative Hubbard U mentioned above, which effectively pins the Fermi level. This led to investigations of the doping viability of the amorphous group IV semiconductors. Chittick et al., 1969 (1) were the first to successfully dope amorphous silicon deposited from a glow-discharge (GD) plasma of silane gas,  $\text{SiH}_4$  (at this point it may be helpful to refer to Appendix A, for a summary of the various preparation techniques for amorphous silicon). The doping effect they obtained was not as dramatic as that later gleaned by the efforts of the Dundee group (Spear and Le Comber, 1975 (118b)). The Dundee group was able to move the Fermi level from within 0.1 eV of the conduction band edge to 1.4 eV away from the edge (28, 118b). They were subsequently able to produce the first p-n junction diodes from amorphous silicon (119), and have expanded upon this work much more recently (135). This doping effect was immediately confirmed by the Xerox group (Knights, 1976 (134)) on films prepared using a capacitively coupled GD system.

Meanwhile characterizations of sputtered and evaporated glassy silicon samples were compared to the same characterizations of GD material, most notably by the IBM group (Brodsky et al., 1970 (2)). They found differences which they speculated could be due to the inclusion of hydrogen in the GD case only. The IBM group followed up on these ideas and demonstrated that H, not surprisingly, was indeed alloyed with Si in the GD samples, and absent, of course, in the material prepared by the other methods (17). The now almost universally accepted reason that H incorporation into the CRN of amorphous silicon (from now on the material will

be referred to as a-Si(H)) has such a dramatic effect on electronic properties is that the H bonds to and satisfies what would otherwise be "dangling bonds." The most important evidence of this will be found in the work by the IBM group (52,2,21) for a-Si and work by the Harvard group (10,11) on a-Ge; this is the underlying theme of much of the review edited by Brodsky (149). We will look at this evidence and more in section I.D.1, from the magnetic resonance point of view. As mentioned in section I.C.4, these dangling bonds (or defects in topological order) create deep levels that pin the Fermi level and cause hopping conduction which masks photoconductive effects. Thus, an amorphous CRN with point topological disorder and miserable electronic properties (from the usual device point of view) may be transformed by H passivation into a material with almost crystalline electronic properties.

The work of the Dundee group must have been viewed with much excitement by the workers at RCA; Carlson and Wronski (120) of RCA produced the first a-Si(H) solar cell in 1976, using a p-i-n structure requiring doping procedures similar to those demonstrated by their colleagues at Dundee. The RCA group attained an efficiency of 2.4% with a device having a square millimeter of collection area. For a point of reference, it is interesting to note that the first crystalline silicon solar cell made by Chapin et al. in 1954 (117a) had an efficiency of 6%. Furthermore, crystalline silicon cells now attain efficiencies of about 19% (118a); while the talk of 8% efficient a-Si(H) cells with square centimeters of area is taken by most to represent the true state of the art (139c). A good general review of GD a-Si(H) solar cell characteristics is given by Carlson et al. (122).

The Harvard group soon demonstrated the feasibility of producing cells by the reactive sputtering (RS) process (see Appendix A), in which the all important H passivation is achieved by leaking hydrogen gas into the chamber with the argon sputtering vehicle. The Ames group (35) later fabricated films with desirable photoconductive properties, and demonstrated some important advantages (to be discussed below) that the RS process has over the GD fabrication technique. It now appears that virtually any method of producing amorphous silicon that incorporates bonded H will manifest transport properties somewhat akin to the crystalline material; the chemical vapor deposition (CVD) processes also appear to produce promising material (139c). The prospects of further increasing solar cell efficiencies were given a boost with the disclosure by the Energy Conversion Devices group (Ovshinsky and Madan, 1978 (125)) that the incorporation of fluorine into a silicon hydrogen plasma would produce films of much better quality. However, the viability of this fluorinated material has not been widely substantiated.

The applications of a-Si(H) are not limited to solar photovoltaic cells. This amorphous material has been demonstrated to be of value in the fabrication of: fast recovery photodetectors (136), ferroelectric image scanners (137), Schottky barrier diodes for rectification (121), metal-oxide-semiconductor field effect transistors (138), solar thermal energy absorbers (124), optical storage devices (126), and vidicon/Xerographic devices (131).

What can be done to further improve the electronic qualities of these films? We will be closer to the answer when the specific nature of the

transport deficiencies are understood and their ultimate relationships to structural configurations clearly delineated. For the important case of solar cell efficiencies the most probable gremlin is photocarrier recombination. The most important cause of this effect is the presence of residual deep levels in the gap (132,127,98,91) which leads to carrier trapping (139b,143); hydrogen passivation is not yet completely effective. This was recognized by the Dundee group early on, and they provided one of the first DES measurements using the field effect technique (8b). They measured  $10^{18} \text{ eV}^{-1} \text{ cm}^{-3}$  states at the Fermi level. More recently, the Xerox group measured  $10^{17} \text{ eV}^{-1} \text{ cm}^{-3}$  at the Fermi level (38). Measurements have been made using photoemission results correlated with photoconductivity measurements to obtain a DES of  $10^{20} \text{ eV}^{-1} \text{ cm}^{-3}$  (42) (the authors in that work caution that the resolution is only .3 eV). Other methods of obtaining the DES that have been applied to a-Si(H) include the use of thermally stimulated currents (41) and electron tunneling (3). There is much controversy still surrounding the magnitudes and detail of the DES distributions obtained by any of these techniques (149). However, the existence of them is agreed upon.

The next step is to gain an understanding of the structural defects that lead to these deep levels and the sample preparation conditions responsible for their occurrence. The simplest type of structural characterization of consequence may be the determination of H concentration. This has been done by: the nuclear reaction rate method (9, 44a), calculations of areas under infrared (ir) absorption peaks (47a), and intensities of proton NMR signals (68,71,72). The last method will be expounded later.

A great deal of information relating to the bonding of H in the a-Si network has been obtained by ir measurements and their interpretation (13, 36, 47a, 19, 35, 23, 109, 34, 40). The conclusions derived from these measurements were sometimes tainted by dissension (109), however the work of Shanks et al. (79) to be discussed in detail in Chapter IV goes a long way toward clearing up ambiguities in the interpretation of the ir results. The infrared absorption measurements show that GD material produced at substrate temperatures below 200°C have significant amounts of H bonded to Si in a dihydride configuration (36, 27). Much evidence exists to support the contention that these dihydride bonding configurations act as recombination trapping centers (7a, 35, 139b). Further studies (13, 34, 37, 27) in correlation with transmission electron microscopy (TEM) work and other methods have shown that this dihydride bonding leads to intermediate range disorder or inhomogenieties in the form of a columnar morphology in which material that incorporates H through monohydride bonding only forms columns. The regions in between are made up of crosslinked, highly topologically disordered,  $(\text{SiH}_2)_n$  polymer chains. It is not difficult to understand how this type of disorder could lead to poor transport. Hydrogen gas evolution studies as a function of temperature (33) have confirmed the presence of dihydride bonds. However, the work of Shanks and Ley (47b) urges caution with the interpretation of these results in light of their work with hydrogen yields and bubbling effects. Just as elevation of the substrate temperature in the GD case leads to decreases in dihydride bonding, Jeffrey et al. (35a) were able to demonstrate that similar and perhaps enhanced dihydride elimination can be obtained by sputtering with very

high rf power levels. Reactive sputtering has the added advantage that H concentrations can be easily varied while maintaining excellent control over the type of bonding. This, so far, has not been achieved with any other process. Largely as a result of this success, the Ames Lab has applied for a patent to recognize their unique approach to a-Si(H) device film fabrication; it now seems likely that the patent will be granted. Evidence for the columnar morphology present in low temperature GD films also exists for the case of RS a-Si(H) (46). Lowry et al. (71) were able to interpret proton NMR results in a manner which was consistent with this morphology in the low power RS films made by the Ames group. Thus it seems that the intermediate range disorder of columnar morphology in bonding type may be attributed to the preparation parameters of substrate temperature for the GD case and rf power for the RS case.

This simple picture of H bonding in a-Si(H), as so far presented, may not be the whole story. An ample body of evidence exists supporting the presence of unconventional H bonding centers (146,40,113,33,110a,105). These models usually take the form of some sort of Si-H-Si bridge bond. The existence of such bonding centers would no doubt necessitate rethinking the currently accepted ir interpretations, unless the concentration of these centers is not required to be very high. More will be said about this type of bonding later in the main body of this work.

Another feature of H incorporation into the a-Si network is revealed by various measurements of the energy gap as a function of H concentration (26,14,31,30). These works conclude that the gap increases with increasing H concentration. Theoretical explanations of this effect (105, 106) exist.

A naive interpretation of the effect results by considering network relaxation to be a result of H incorporation. As H is incorporated at points in the network that would have otherwise been very strained (i.e. a high degree of quantitative disorder) band tailing decreases, thus increasing the optical gap. If this is carried too far, though, it is conceivable that H clustering could result at highly strained points in the network. Hydrogen clustering has been hinted at in the ir literature (19,47a,35,112), and we shall directly address this question in more detail later. This topological, intermediate range disorder may produce deep levels. Indeed, there is evidence that as the H concentration is increased above certain levels, the concentration of defects associated with recombination centers increases (29, 36).

Finally, it is appropriate here to comment on the Staebler-Wronski effect (15, 39) and the major theory that claims to explain it (100). This is a manifestation of the metastability of disordered materials mentioned in section I.B.7. When a-Si(H) is exposed to light for long periods of time (several days) very large changes in the photoconductivity occur. This effect is reversible by annealing the sample at moderate temperatures. The theory of the Staebler-Wronski effect holds that the Fermi level is actually moved by the photo-production of defects in the material. These defects are believed to have such a large effect on the DOS distribution that considerable Fermi level movement becomes possible. The solar cell performance of a-Si(H) is apparently not affected appreciably (39); while the fluorinated material apparently shows no Staebler-Wronski effect (25).



## E. Magnetic Resonance Studies of a-Si(H)

### 1. Electron paramagnetic resonance (EPR) studies

The IBM group, headed by Brodsky, provided one of the first electron paramagnetic resonance studies of a-Si (for details of EPR and NMR methods and terminology please see Chapters II and III). This early study featured measurements on sputtered samples with no hydrogen; the passivation properties of H were not yet appreciated. They found a resonance at about  $g=2$  that was an effect due to the bulk of the material, but which resembled the signals that were earlier attributed to a cleaved Si(111) surface. They naturally speculated that this signal in the amorphous material was due to dangling bonds on the surface of microvoids within the material. In a follow-up study in which the effects of contamination were scrupulously avoided (54) the nature of the signal seemed to favor singly distributed dangling bonds rather than the clustering suggested by the microvoid picture.

Hasegawa and Yazaki (53) suggested a relationship between this EPR signal and the hopping conductivity associated with unpassivated samples. Many studies comparing the EPR signal as a function of temperature with the temperature dependence of the hopping conductivity were then performed; for a thorough review see ref. 149. An important one of these (58) clearly established that part of the linewidth was temperature dependent. The lineshape and width dependence upon temperature was clearly a result of motional narrowing (155), the motion correlating very well with that expected for the case of hopping conductivity (92, 96).

This complication in the lineshape of the EPR signal has made analysis of the temperature independent portion difficult and somewhat controversial. The view that seems to be favored at present is (56,90,99): Unpassivated films (no H) have a tendency to form with clusters of dangling bonds, while films prepared by the GD or RS technique tend to have their remaining dangling bonds randomly distributed. The main source of controversy is a new study of EPR on clean silicon surfaces which suggests that all of the cleaved bonds form "backbonds" with their nearest neighbors (7b); it seems unlikely that clustered dangling bonds in a-Si(H) voids would not also pair up.

It should be emphasized here that EPR has played a crucial part in establishing the role of H in a-Si(H) films. Early experiments by the Harvard group (11) involved monitoring the EPR signal in RS a-Ge(H) as a function of H concentration. Their results clearly indicated that the concentration of dangling bonds, as measured by the EPR signal intensity, decreased with increasing H concentration. Similar experiments were carried out with RS a-Si(H) (8a) producing analogous results. The IBM group has done a series of post-deposition hydrogenation experiments in which films which have little or no hydrogen are monitored for dangling bonds using EPR and then hydrogenated to various degrees while monitoring the EPR signal (21). They noticed, however, that the increases in H concentration were an order of magnitude higher than the corresponding decreases in EPR signal intensity. This they took as evidence for weak bonds in the material that are not dark EPR active but will incorporate H. Such complications notwithstanding, these experiments have conclusively demonstrated that H passivates dangling bonds.

Annealing studies of a-Si(H) have also been aided by the use of EPR. The early IBM work (2) demonstrated a large decrease of the EPR signal with increasing annealing temperature. The in situ studies (54) found a similar, but milder annealing effect, while a recent study (59a) has confirmed the annealing effect. This can be understood in terms of network restructuring which results in fewer dangling bonds.

## 2. EPR under conditions of sample illumination

This area of magnetic resonance spectroscopy may eventually prove to be the most direct way of probing the defect structures that have the most important influence upon photovoltaic performance. An excellent discussion is given by Solomon in ref. 149. He refers to the dark EPR active centers as hard centers (having  $U > 0$ , and strongly localized), while the defects that are the subject of this section are dubbed soft centers ( $U < 0$  and small, but weakly localized). It is probably appropriate to think of at least some of these soft centers as weak bonds. The experiments may be conveniently broken down into three categories, on the basis of the experimental detection used.

a. Simple light-induced EPR (LEPR) This phenomenon has been widely observed in a-Si(H) (63a,64,57,65). The signal is obtained by shining super band gap light onto the sample while an EPR experiment is underway. The signal is sometimes lock-in detected from the modulation of the light source or the dark EPR signal may be subtracted from the normally (see Ch. III) detected EPR signal in other cases. Typical results indicate a density of  $10^{15} \text{ cm}^{-3}$  for these light-induced centers.

b. Photoconductively detected EPR (PEPR) This experiment is very much different from the conventional EPR investigation. Here the experimental arrangement is the same as a, above except that a voltage is applied to the sample, in addition. The current passing through the sample is then lock-in detected, instead of detecting the absorbed microwave energy. This effect was first observed by Lepine (61) on Si surfaces (Solomon later expanded upon this work and actually observed these effects in a p-n junction (62)). Solomon et al. (63b) first observed the effect in a-Si(H). The theory of the phenomenon has been largely worked out (97, 111). The gist of the theory holds that the photoconductivity is drastically affected by passing through an EPR resonance because of spin-dependent recombination effects. Thus, photocarrier recombination may be intimately investigated by magnetic resonance techniques.

c. Photoconductive resonance (PCR) This experiment involves the conditions of a, above. When operated at appropriate power levels the signal that is detected by the lock-in amplifier is inverted (180 degrees out of phase). Mendz et al. have observed this sort of signal on Si surfaces and have developed a theory (66). This signal is a result of changes in the cavity Q of the opposite sense to that normally encountered in EPR. As the sample passes through resonance a reduction in photoconductivity takes place due to the spin-dependent recombination mentioned in b, above; this forces a change in Q which is of the sense opposite to the Q change caused by microwave absorption.

### 3. Nuclear Magnetic Resonance studies of a-Si(H)

a. Proton NMR      The use of NMR to study a-Si(H) has just begun. Reimer et al. (68) were the first to report proton NMR studies on GD material. They found that the width of the absorption resonance was due predominantly to dipolar broadening and concluded that there were large inhomogeneities in the H distribution. They were not able to distinguish bonding type (monohydride or dihydride) on the basis of NMR data. Lowry et al. (71) were able to analyze NMR data on high and low rf power RS samples; differences were attributed to bonding. Jeffrey and Lowry (72) analyzed the absorption spectra of a series of high rf power RS samples with varying H concentration. They found evidence of intermediate range disorder similar to ref. 68. The analysis presented in ref. 72, which will be discussed in detail in this work, found that H is distributed in two distinct phases in this RS material (containing only monohydride bonding according to the currently accepted interpretations of ir data). There is a clustered configuration of H suggesting a microvoid passivation model, and a randomly distributed phase of H incorporation. The local densities of H have been calculated for these two phases; these densities are the same from one sample to the next in the H concentration series. Reimer et al. (77) have come to analogous conclusions for their GD samples. As a result of this NMR work some rather surprising conclusions for film growth were hinted at in ref. 72, these will be expanded later in this work.

Carlos and Taylor (69, 73) presented the first measurements of spin-lattice relaxation times in GD material. They proposed a model in which

the temperature and frequency dependence of the proton NMR relaxation was explained by the existence of "disorder mode" proton motion. This mechanism requires the hopping or tunneling of a proton between the wells in a double well potential. This produces the most effective relaxation, hence a spin-lattice relaxation time minimum, at the temperature that forces the proton motion to be at the same frequency as the Larmor precession. Reimer et al. found evidence in support of this view (82). Movaghar and Schweitzer argued (114, 115) that this was not so because the number of such disorder mode centers that would be required should be directly visible in the NMR spectra—they have not been seen to date. Conradi and Norberg (116) speculated that the relaxation data could be explained by requiring that molecular hydrogen exist in the films in ~500 ppm concentrations. Carlos and Taylor have reported strong evidence for this in GD samples. The Ames group has speculated (70a, 75) that relaxation effects in some of their RS samples could have electronic origins. The relaxation data from the RS samples of the Ames group will be analyzed with these and other models in Chapter IV.

There have been at least two studies of annealing effects upon NMR spectra in this material (76, 80a); both of these dealt with GD samples. Both report that H evolution begins from the clustered phase. The NRL group (80a) also reports that no significant change in the observed spin-lattice relaxation time minimum was observed—even up to annealing temperatures that had driven off half of the incorporated H.

For a somewhat broader view, it is interesting to note that Reimer et al. (70b, 81) have conducted proton NMR experiments on amorphous films

of silicon, silicon/carbon, carbon, boron, and silicon/nitrogen alloyed with hydrogen. They observe motional narrowing in the a-Si/N:H, a-B:H, and a-C:H films which they attribute to disorder mode proton motion.

b.  $^{29}\text{Si}$  NMR studies Reimer et al. (80b) have reported silicon NMR spectra for GD samples. Very little was concluded. Jeffrey et al. (70c) have done some silicon NMR work on RS samples. They have analyzed data using the theoretical model of Guttman et al. (110b) to draw conclusions about the charge density variations in a-Si(H).

Although the NMR of a-Si(H) is a very young branch of a new and exciting field of research into the disordered states of condensed matter, it has already spawned a short review article (78). Much of it was out of date the day after it was written--nonetheless, it may serve as a focal point to order one's thoughts.

Finally, this rather lengthy introduction to magnetic resonance studies of reactively sputtered amorphous silicon hydrogen alloys is brought to a close. It is hoped that the reader has gained some appreciation for the attributes of the disordered state: its many structural possibilities--the 'freedom of bonding' as Ovshinsky (103) has put it--that are inherent to the amorphous phase, the consequences that these many degrees of freedom have for electronic properties, the burdens of reproducibility that they necessarily place upon the material preparation techniques, and (most importantly for what follows) the many challenges this freedom implies for structural characterization.

## II. MAGNETIC RESONANCE THEORY

The phenomenon of magnetic resonance was first observed by Rabi et al. in the 1930s, a few years after Heisenberg and Schrodinger had developed their quantum theory. Rabi's experiments were done on spin  $1/2$  particles in a beam. Particles in the ideal beam do not collide, and interact otherwise only very weakly; thus, the beam experiments provide the best approximation to the observation of completely isolated spinning particles. Stern and Gerlach had earlier demonstrated that spin  $1/2$  particles in a beam may be made to assume the wavefunction of the pure state; either "spin up" or "spin down."

Bloch, in 1946, was then the first to successfully observe magnetic resonance in the, much more complicated, condensed matter environment. As shall be seen, the wavefunction of the individual spin in this situation is not a pure state.

Much of what will follow in this chapter is a synthesis of the treatments given the theory by several authors. This account will only, however, give a brief outline of the theoretical ideas; much of the mathematical detail will be omitted. This outline reflects the spirit and much of the content of the book by Macomber (155). His book should be consulted for references to the works already mentioned; they figure prominently in his discussion. The magnetic resonance book by Slichter (156), the statistical mechanics book by Feynman (157), the spin temperature book of Goldman (158), the magnetic resonance book of Pake and Estle (159), the quantum mechanics book by Merzbacher (160), the quantum



mechanics book of Landau and Lifshitz (161), the pulsed magnetic resonance book of Farrar and Becker (162) and, of course, the "Magnetic Resonance Bible" by Abragam (163) have all contributed to the present brief discussion.

#### A. Fundamental Theory: Isolated Spins

As previously mentioned, beams of spinning particles offer the closest approximation to the isolated spin system. The Hamiltonian for such a system is

$$H_0 = -\vec{\mu} \cdot \vec{H}_0, \quad (2)$$

$$\vec{\mu} = \gamma \vec{J} \quad (\gamma > 0 \text{ for positive charges,}$$

$$\gamma < 0 \text{ for negative charges),}$$

where  $\gamma$  is the magnetogyric ratio of the particle in question, in our case a nucleus or an electron.  $\vec{H}_0$  is a static or slowly varying applied magnetic field and usually taken to define the  $+\hat{z}$  direction, and is called the Zeeman field. It is no accident that we deal with the magnetic field, as opposed to the magnetic induction,  $\vec{B}$ . The former has as its source 'external' or 'free' currents, and does not incorporate any magnetization due to 'internal' or 'bound' currents. In the case of condensed matter, which we shall address shortly, this is an important distinction, see Schwartz (164). For the electron it is customary to refer to the  $g$  value which also takes into account angular momentum contributions other than pure particle spin (orbital motion of some type, Pake and Estle (159)). This 'catch all' value is given by

$$\gamma_e = -g\beta$$

$$\beta = \frac{e\hbar}{2m_e c} . \quad (3)$$

The eigenvalues of the Hamiltonian are

$$E_m = -\gamma \hbar H_0 m \quad (4)$$

$$m = -J, -J+1, \dots, J .$$

For dipole transitions (the only kind dealt with here),  $|\Delta m| = 1$ . Therefore, a transition between states corresponds to the absorption or emission of a photon of energy,

$$\hbar|\omega_0| = \hbar|\gamma H_0|, \quad (5a)$$

$$\text{and } \nu = |\gamma H_0|, \quad \gamma \equiv \gamma/2\pi \quad (5b)$$

$$\omega_0 = -\gamma H_0,$$

where  $\nu$  is the frequency of the laboratory oscillator that initiates the transition. The last equation is often called the resonance condition. (Note that  $\omega_0$  is allowed to be positive or negative depending upon the sign of  $\gamma$  and  $H_0$ . This will be convenient for specifying the sense of the precessional motion to be described below.)

Before we proceed to the details of the transition process, it is appropriate to list the parts of the Hamiltonian that we have left out. Actually, if the particle is not isolated, then,

$$H = H_0 + H_1 + H_R; \quad H_R = H_{SS} + H_{SL} \quad (6)$$

The Zeeman term,  $H_0$ , is by far the largest,  $H_1$  represents any excitation from outside the sample,  $H_{SS}$  represents the interactions between individual spin systems, and  $H_{SL}$  represents the interaction of the ensemble of spin systems with the lattice. These last two Hamiltonians are collectively termed relaxation interactions.

#### B. Classical Precession: The Transition Process from the Classical Point of View

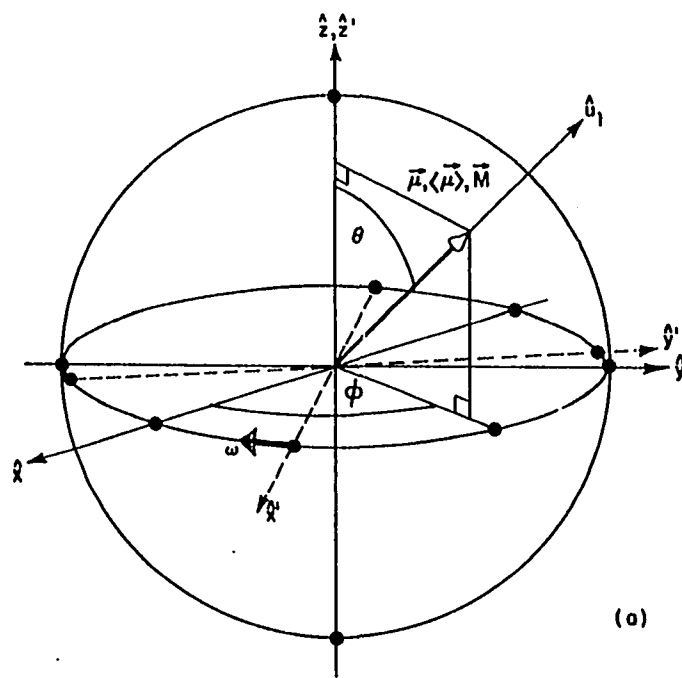
If one combines the classical equations governing the rate of change of angular momentum and the expression that gives the torque on a classical magnetic dipole, the result is (see Pake and Estle (159))

$$\frac{d\vec{\mu}}{dt} = -\gamma \vec{H} \times \vec{\mu} = \omega_0 \hat{z} \times \hat{y}. \quad (7)$$

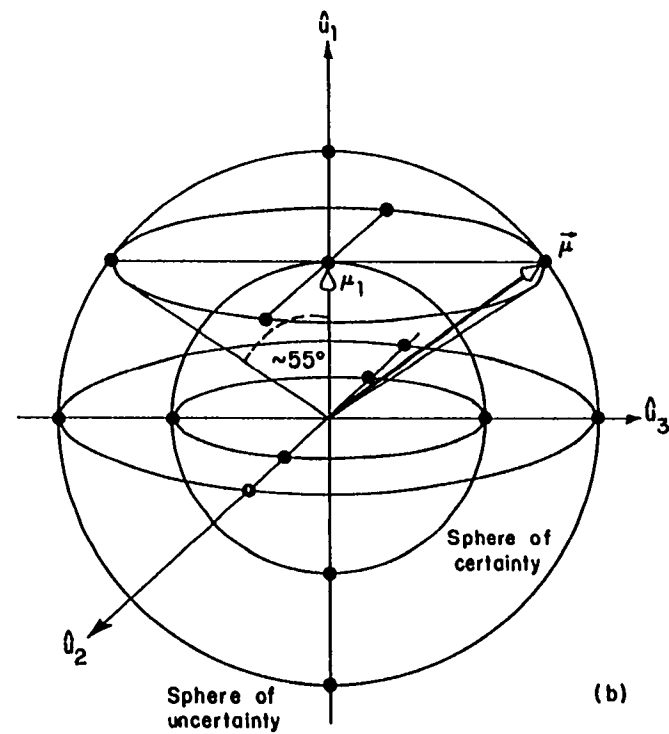
This describes the precession of the dipole moment about the field direction with the frequency of the precession given by  $\omega_0$ , the Larmor frequency (see Fig. 3a). The sign of  $\omega_0$  will determine the sense of the precession. When  $\gamma > 0$  and  $H_0 > 0$  (which is usually the case, convention dictates that  $H_0$  lie along the positive  $\hat{z}$  direction) then  $\omega_0 \hat{z}$ , the precession vector, will lie along the negative  $\hat{z}$  direction. The right hand rule may then be used to deduce the rotational sense of the precession. The transition from spin up (parallel to  $\vec{H}_0$ ) to spin down (antiparallel to  $\vec{H}_0$ ) may be accomplished by shining circularly polarized coherent light upon the sample (typically radio frequencies for nuclei and microwaves for electrons), which is embedded in the strong Zeeman field. Since we will be talking about a magnetic dipole transition the only component of the

Fig. 3a. (adapted from Macomber) This depicts the laboratory coordinate system, defined by the cartesian unit vectors,  $\hat{x}$ ,  $\hat{y}$ ,  $\hat{z}$ ; also the rotating coordinate system (the rotating frame) is represented by the unit vectors  $\hat{x}'$ ,  $\hat{y}'$ ,  $\hat{z}'$ . This coordinate system rotates about the  $\hat{z}=\hat{z}'$  axis with angular speed,  $\omega$ . The sense of the rotation is negative for positive spinning charges and positive for negative spinning charges. The vector whose tip is on the sphere could represent  $\vec{\mu}$ ,  $\langle\vec{\mu}\rangle$ , or  $\vec{M}$ .  $\phi = \eta - \omega_0 t$ , whose  $\eta$  is a phase determined by initial conditions. In the case of the FID experiment  $\theta = \gamma H_1 t$ ; for the case of the ASP experiment  $\sin \theta \sim H_1$  (see text for details). The vector  $\mu_1$  represents the direction of the "certain component" of angular momentum, see Fig. 3b and text

Fig. 3b. (adapted from Macomber) A spinning particle in a pure state subject to an applied Zeeman field has one component of angular momentum,  $\mu_1$ , along the "certain axis" (in equilibrium this is coincident with the Zeeman field direction). The other two components are uncertain and unobservable. When the particle is in the transitory superposition state the uncertain components become observable. The certain axis may be forced away from the Zeeman field direction during a magnetic resonance experiment, see text



(a)



(b)

field that need concern us is the magnetic component. We will call this component  $\vec{H}_1$ . In practice the light used is simply linearly polarized (which is the superposition of two opposed circularly polarized beams; we may ignore the beam that is polarized in the wrong direction, see Pake and Estle (159), Slichter (156), or Macomber (155)).

Initially our dipole will precess around the static field (provided that it hasn't somehow become lined up with the field) with the frequency of the precession being the same as the Larmor frequency. We will transform our coordinate system to a frame rotating in coincidence with the precessional axis of the dipole, where the cartesian axes will be  $\hat{x}'$ ,  $\hat{y}'$ , and  $\hat{z}'$  (henceforth, this will be called the 'rotating frame'). All motion ceases to the observer in this frame, with the dipole still aligned at the same angle with the  $\hat{z}' = \hat{z}$  axis common to both frames. We may generalize this transformation procedure and write (see Pake and Estle (159))

$$\frac{d'\mu}{dt} = -\gamma \vec{H}_e \times \vec{\mu},$$

$$\vec{H}_e = \vec{H} + \frac{\vec{\Omega}}{\gamma} = H_1 \hat{x}' + (H_0 + \frac{\omega}{\gamma}) \hat{z}', \quad (8)$$

$$\vec{\Omega} = \omega \hat{z},$$

where,  $\vec{H}_e$  is the effective field, and the assumptions of arbitrary frequency of rotation,  $\omega$ , and arbitrary Zeeman field strength have been taken; however, the field  $\vec{H}_1$  is assumed to rotate with the same frequency as the rotating frame. The prime on the derivative indicates that the operation

is carried out in the rotating frame (it will be the custom throughout to use primes when referring to the rotating frame). The motion described is that of a precession around the direction of  $\vec{H}_e$ , the speed of precession,  $\omega_e$ , then being proportional to the magnitude of the effective field:

$$\omega_e = \gamma(H_1 + (H_0 + \frac{\omega}{\gamma})^2)^{1/2} . \quad (9)$$

We may regain our original rotating frame by applying the resonance condition to Eq. 9. This implies that

$$\begin{aligned} \omega_0 &= -\gamma H_0 \\ \omega_e &= -\gamma H_1 \equiv \omega_1 \\ \frac{d'\vec{\mu}}{dt} &= -\gamma \vec{H}_1 \times \vec{\mu} . \end{aligned} \quad (10)$$

Once back in this resonantly rotating frame, we imagine that initially  $H_1 = 0$ . We then allow it to suddenly assume a fixed finite magnitude. This implies a precession of the dipole around the  $\hat{x}'$  direction. At any time,  $t$ , after the rotating field has been turned on the angle of inclination of the dipole with respect to the  $\hat{z}'$  direction is given by

$$\theta = |\omega_1|t = |\gamma H_1|t . \quad (11)$$

Suppose that we turn off the rotating field when  $\theta = \pi/2$ . We have pumped energy into the system—energy equal to  $|\vec{\mu}| |\vec{H}_0|$ . If we now step back into the laboratory frame we witness a dipole precessing at the Larmor frequency in the  $\hat{x}$ - $\hat{y}$  plane. As the dipole precesses we know that

it must radiate and lose its energy. This radiated energy forms the free induction decay (FID) signal that is detected in the lab. If the pulse is left on until  $\theta = \pi$ , the dipole will have been flipped antiparallel to the field; energy equal to one photon of Eq. 5a will have been absorbed.

In reality, this experiment is carried out on an ensemble of dipoles. The signal observed is coherent radiation, much like laser light only lower in frequency. A very short time after the  $90^\circ$  pulse the individual dipoles begin to lose phase coherency (this happens on a time scale characterized by the spin-spin relaxation time,  $T_2$ ). The free induction signal then decays in a time on the order of  $T_2$ . This often happens much faster than the dipoles can give up all of their magnetic energy to their surroundings (the time of this so called spin-lattice relaxation is on the order of  $T_1$ ).

This classical conceptual device, the rotating frame, comes very close to describing the FID experiment. There are some troubling aspects, however. If the spin ensemble is left in the Zeeman field for very long, all of the dipoles should become lined up with the field. In that case there will be no precession; what significance does a rotating frame then have? Furthermore, the FID experiment entails the absorption and emission of only half of a photon; how can this be? For a completely unambiguous description of the FID one must turn to quantum mechanics.



### C. The Quantum Mechanical Description of the FID Experiment

It has been established that spinning particles may exist in pure eigenstates of the energy in the beam experiments mentioned earlier. It is valuable to consider the entropy of such a configuration. Feynman (157) shows that the entropy of pure states is zero; this seems reasonable since the beam is a very ordered arrangement. This would imply that the temperature (considering just the spin energy) of the ensemble is undefined (see Kubo (165)); again, this seems reasonable since the individual spins are not interacting they can not communicate a sense of temperature amongst themselves. Therefore, in the case of an ensemble of interacting spins--definitely the situation for spins in condensed matter--the wavefunction of the individual spin is not a pure state. Indeed, one is therefore compelled to admit that the wave function is a superposition of the eigenstates of the energy. For the spin 1/2 case we may write

$$\psi(t) = Ae^{ia} e^{-i\alpha t} |\alpha\rangle + Be^{ib} e^{-i\beta t} |\beta\rangle, \quad (12a)$$

where we have made the following abbreviations:

$$H_0 |m\rangle = E_m |m\rangle, \quad (12b)$$

$$m \equiv E_m / \hbar,$$

$$|m\rangle \equiv |J, m\rangle,$$

and  $m$  stands for either  $\alpha$  or  $\beta$  ( $m = \frac{1}{2} \rightarrow |\alpha\rangle$ ,  $m = -\frac{1}{2} \rightarrow |\beta\rangle$ ). Note that  $A$ ,  $B$ ,  $a$ ,  $b$ ,  $\alpha$ , and  $\beta$  are all real numbers. This is, of course, the most

general solution to the time dependent Schrodinger equation, considering only the spin portion of the wavefunction. Normalization requires

$$A^2 + B^2 = 1 . \quad (13)$$

A convenient parameterization is

$$\begin{aligned} A &= \cos(\theta/2) \\ B &= \sin(\theta/2) . \end{aligned} \quad (14)$$

If we consider some observable property of the system, call the operator  $P$ , then we may in general calculate the time dependent expectation value of that property:

$$\langle P \rangle = A^2 P_{\alpha\alpha} + B^2 P_{\beta\beta} + 2AB P_{\alpha\beta} \operatorname{Re}[e^{i(b-a)} e^{-i(\beta-\alpha)t}] . \quad (15)$$

$$P_{mm'} \equiv \langle m | P | m' \rangle .$$

Notice that time dependence in Eq. 15 vanishes unless

$$[P, H] \neq 0 . \quad (16)$$

What sort of property,  $P$ , is there that will have a time dependent expectation value? It is obvious that if the energy is to be measured its expectation value will have no time dependence, the expectation value will be an average of the two eigenvalues of energy, weighted with  $A^2$ , and  $B^2$ . Does the system actually move back and forth from one eigenstate to the next? Yes. The interaction between spins in an ensemble is through the radiation field, i.e. the individual spins are constantly absorbing

and reemitting photons. This must be the case in order that the ensemble have a temperature. Any attempt at measuring the energy can be viewed then as one of the endless cycles in the absorption or emission process: the result of the measurement will yield the higher energy state in the case of emission and the lower energy state in the case of absorption. All of this then is just the equivalent of the Heisenberg uncertainty principle; the exact state of the system is unknowable because the act of measuring disturbs the system. Of course, we can say something about the probability of a particular outcome. In our case, as hinted at above, any particular measurement outcome has a probability determined by  $A^2$  or  $B^2$ . Shortly, it will be seen that for an ensemble of identical systems these values are intimately connected to the temperature. First, the question of what observable actually oscillates with time must be addressed. The answer to this question will also, eventually, provide insight into the process by which photons are absorbed and emitted by the systems of the ensemble.

The quantum mechanical equation of motion for the angular momentum is

$$\frac{d\vec{J}}{dt} = \frac{i}{\hbar} [H, \vec{J}]. \quad (17)$$

This equation is only symbolically true.  $\vec{J}$  has no time dependence (Schrodinger picture). It is written with the understanding that an expectation value must be taken of both sides and the time derivative then taken outside of the expectation value brackets (see Slichter (156)). Equation 17 along with the uncertainty relations for the components of the angular momentum,  $\vec{J}$ ;

$$\begin{aligned}
[J_x, J_y] &= i\hbar J_z, \\
[J_y, J_z] &= i\hbar J_x, \\
[J_z, J_x] &= i\hbar J_y,
\end{aligned} \tag{18}$$

yields:

$$\frac{d\vec{J}}{dt} = -\gamma\vec{H}_0 \times \vec{J}, \tag{19}$$

where we have specified  $H = H_0$ . If we then restore the meaning of the time derivative, and use the definition of  $\vec{\mu}$ , Eq. 2, we have

$$\frac{d\langle\vec{\mu}\rangle}{dt} = -\gamma\vec{H}_0 \times \langle\vec{\mu}\rangle, \tag{20}$$

which of course indicates precessional motion of  $\langle\vec{\mu}\rangle$  about the Zeeman field. It is important to realize that the time dependence of  $\langle\vec{\mu}\rangle$  derives from two facts: the uncertainty relation for angular momentum, Eq. 18, and the assumption of a superposition wavefunction for the spinning particle, Eq. 12. A geometrical interpretation of the uncertainty relation (Fig. 3b) is helpful. The spinning particle in a static magnetic field has a "certain axis" for the components of angular momentum; it is parallel to the Zeeman field. A measurement of the component of angular momentum along this axis yields one of two possible values for spin 1/2, always. The expectation value of this component is not time dependent. On the other hand, the expectation value of one of the other components, say the x component, yields:

$$\langle \mu_x \rangle = AB\gamma\hbar \operatorname{Re}(e^{i(b-a)} e^{-i(\beta-\alpha)t}), \quad (21)$$

for the dipole moment proportional to that component of angular momentum. The uncertainty principle demands that the angular momentum vector may never line up precisely with the Zeeman field. This necessarily implies that there will always be a transverse component to the angular momentum, and thus to the magnetic dipole. If the spin is in a pure state this transverse component is unobservable (imagine setting A or B to zero in Eq. 21). Only when the system is 'in transit' will one observe a transverse component. In the presence of other dipoles, this ubiquitous transverse component is the source of the radiation that simultaneously couples the dipoles to each other and thereby forces the individual wavefunction to be a time dependent superposition of eigenstates.

The classical situation, by way of contrast, is very different. The angular momentum vector is allowed to line up certainly in one direction; if one imagines the length of the angular momentum vector, in units of  $\hbar$ , approaching infinity the classical momentum is obtained. There will be no precession at equilibrium in this case.

With the quantum mechanical formulation, it is not difficult to extend the earlier classical treatment of the FID experiment, and put it on much firmer ground. It is assumed that the individual spin is in the superposition state given by Eq. 12; it should be understood that this is the result of the spin constantly interacting with its neighbors--absorbing and emitting photons through the coupling of their transverse magnetic dipole components (more will be said about this interaction, later). It

is also assumed that the entire spin ensemble is at equilibrium with the lattice; this will determine the values of A and B in Eq. 12. If we now transform to the rotating frame, as the  $90^\circ$  pulse is turned on, the Hamiltonian becomes

$$H' = -\vec{\mu} \cdot \vec{H}_1 = -\gamma \vec{H}_1 \cdot \vec{J}; \quad E'_m = \pm \frac{\gamma H_1}{2}. \quad (22)$$

We have transformed away the Zeeman Hamiltonian, such that we are now in the interaction representation (see Merzbacher (160)). The Zeeman Hamiltonian is a quantum mechanical generator of rotations about the  $\hat{z}$  axis, so the transformation to the rotating frame can be done rigorously (see Goldman (158)). Then in this representation the wavefunction becomes

$$\psi'(t) = A'e^{ia'}e^{-i\alpha't}|\alpha'\rangle + B'e^{ib'}e^{-i\beta't}|\beta'\rangle. \quad (23a)$$

We may set the phases, a and b such that

$$A'B' = A'^2 - B'^2, \quad (23b)$$

because at  $t=0$  the dipole is certainly along the  $\hat{z}$  axis, and the wave function can not change infinitely quickly. By analogy with Eq. 21, the expectation value of the  $\hat{z}'$  component of the magnetic dipole is given by:

$$\begin{aligned} \langle \mu_{z'} \rangle &= A'B'\gamma\hbar \text{Re}(e^{-i(\beta'-\alpha')t}) \\ &= A'B'\gamma\hbar \cos(\omega_1 t) \\ \beta' - \alpha' &= \gamma H_1 = -\omega_1. \end{aligned} \quad (24)$$

It is also known that  $\langle \mu_y \rangle = 0$  at  $t=0$ . Therefore, after a time,  $t$ , the angle between the expectation value of the magnetic dipole vector,  $\langle \vec{\mu} \rangle$ , and the  $\hat{z}$  axis will be given by Eq. 11. If the rf pulse is now turned off and we return to the lab frame, Fig. 3a describes the orientation of the expectation value of the magnetic dipole vector,  $\langle \vec{\mu} \rangle$ . Now, if the duration of the pulse is sufficient (or alternatively, if  $H_1$  is strong enough)  $\theta$  may be equal to  $90^\circ$ . In Macomber's terminology, the 'certain component of the angular momentum' has been rotated  $90^\circ$ , i.e.  $\hat{\mu}_1$  of Fig. 3b, originally aligned with  $\hat{z}'$  is made to rotate into coincidence with  $+\hat{y}'$ . Upon again returning to the lab frame, after the pulse is turned off, the expectation value of the x component of the magnetic dipole is given by Eq. 21, however the values of A and B are no longer the original ones determined by the equilibrium condition. Now they are equal. This may be seen by recalling that  $\langle \mu_z \rangle = 0$  after the  $90^\circ$  pulse; use of the same boundary condition that gave Eq. 23b shows directly that  $A = B$ . This, of course, implies that the magnetic dipole vector is precessing around the Zeeman field in the x-y plane. Once again, we have arrived at the FID configuration for the individual dipole. This time, however, the dipole direction (by this we mean certain component) started out along the z axis; the rotating frame was not contrived, but appeared naturally through the interaction representation.

There are still some troubling aspects to the present model. The actual FID experiment is carried out on a collection of dipoles, an ensemble of spin  $1/2$  systems. So far, we have only vaguely acknowledged this by noting it to be the reason that the wavefunction of the individual

system is a superposition of energy eigenfunctions (or equivalently eigenfunctions of the z-component of the angular momentum). The behavior of the ensemble of spin systems will be treated with some rigour in the next section.

#### D. The Interaction of the Spin System with its Surroundings: Density Matrix Formalism

Feynman motivates his lecture on the density matrix by noting that when we do basic quantum mechanics we divide the world into two parts: the system (in our case an individual spin 1/2 particle in a Zeeman field), and the rest of the universe (p. 39 of ref. 157). Then we consider only the wavefunctions of the system, paying no attention to the rest of the universe. This is, of course, not the proper way to set the problem up. One should always consider a wavefunction of the following form:

$$\psi = \sum_{ij} d_{ij} |m_i\rangle |\phi_j\rangle, \quad (25)$$

where  $|m_i\rangle$  is a basis function of the system and  $|\phi_j\rangle$  is a basis function describing those degrees of freedom of the universe that may interact with the system being studied. Then the matrix defining any general property of the system only is given by

$$\tilde{P} = \sum_{jkl} P_{jk} |m_j\rangle \langle \phi_l| \langle \phi_1| \langle m_k| \quad (26)$$

$$P_{jk} = \langle m_j | P | m_k \rangle.$$



We may consider the wavefunction of just the system again as

$$\psi = \sum_i C_i |m_i\rangle, \quad (27)$$

where the rest of the universe is taken into consideration by

$$C_i = \sum_j d_{ij} |\phi_j\rangle. \quad (28)$$

If we then define a matrix,  $\tilde{D}$ , by

$$D_{jk} = \sum_i d_{ji} d_{ki}^* \equiv \langle C_j | C_k \rangle^*. \quad (29)$$

The above expression incorporates an inner product over the wave functions that describe the environment of the system. We may easily calculate the expectation value of the property of the system,  $P$ , by

$$\langle P \rangle = \text{Tr}(\tilde{D}\tilde{P}) = \sum_{j=1} \left( \sum_k D_{jk} P_{kj} \right). \quad (30)$$

Now, the operator  $D$  implicitly includes the motions of the individual system's environment; this will encompass motions of all of the other spin systems. Therefore, the effects of an individual system's environment upon the expectation value of a property of the system only,  $P$ , are conveniently taken into account. This formalism is equivalent to assuming a superposition wavefunction, however it has the advantage of incorporating the ensemble statistics in a natural way and will give precise meaning to the coefficients of the superposition wavefunction. For our spin 1/2 system,

$$\tilde{D} = \begin{bmatrix} A^2 & ABe^{i(b-a)}e^{-i(\beta-\alpha)t} \\ ABe^{-i(b-a)}e^{i(\beta-\alpha)t} & B^2 \end{bmatrix} \quad (31)$$

This immediately implies

$$\begin{aligned} \langle \mu_x \rangle &= \frac{1}{2} \gamma \hbar (D_{\alpha\beta} + D_{\beta\alpha}) \\ \langle \mu_y \rangle &= \frac{1}{2i} \gamma \hbar (D_{\alpha\beta} - D_{\beta\alpha}) \\ \langle \mu_z \rangle &= \frac{1}{2} \gamma \hbar (D_{\alpha\alpha} - D_{\beta\beta}) . \end{aligned} \quad (32)$$

We have lumped all of the time dependence of the wavefunction with its coupling to its environment into the matrix  $\tilde{D}$ . The equation of motion is

$$i\hbar \frac{d\tilde{D}}{dt} = [H, \tilde{D}] . \quad (33)$$

If we consider an ensemble of systems, any macroscopic property of the ensemble will be an average of the expectation values of that property for each system. Considering  $N$  systems,

$$\langle \bar{P} \rangle = \frac{1}{N} \sum_{n=1}^N \langle P \rangle_n . \quad (34)$$

This motivates the definition of the density matrix,

$$\rho_{jk} \equiv \frac{1}{N} \sum_{n=1}^N D_{jk}^{(n)} , \quad (35)$$

such that,

$$\langle \bar{P} \rangle = \text{Tr}(\tilde{\rho}\tilde{P}) , \quad (36)$$

where the bar indicates an ensemble average. This demonstrates that the diagonal elements of  $\tilde{\rho}$  are the probabilities that the system will be found in a particular eigenstate. The basic postulate of statistical mechanics implies that

$$\rho_{jj}^e = e^{-E_j/kT} / Q, \quad (37)$$

where  $\rho_{jj}^e$  indicates the value at equilibrium,  $T$  is the temperature of the spin system and the lattice at equilibrium, and  $Q$  is the partition function, see Feynman (157). Now one may define a temperature for the spins,  $T_s$ , other than the temperature of the lattice. For spin 1/2,

$$\rho_{\beta\beta} / \rho_{\alpha\alpha} = e^{-(\beta-\alpha)\hbar/kT_s}. \quad (38)$$

This implies that the spin ensemble has reached some sort of equilibrium independent of the lattice. The nature of this equilibrium will become apparent shortly.

We may write an equation of motion for this density matrix,

$$\frac{d\rho_{ik}}{dt} = \frac{1}{i\hbar} [\tilde{H}, \tilde{\rho}]_{jk}, \quad (39)$$

where the Hamiltonian of Eq. 6 has been used. This equation, in principle, contains all information about the entire ensemble, and therefore will describe the macroscopic observables. Its utility derives mainly from its ability to deal with each system in an average fashion by ascribing a temperature to define its diagonal elements. By analogy with Eq. 31 it

may be seen that the off-diagonal elements of  $\tilde{\rho}$  may be time dependent. Equation 36 suggests that the time dependence of  $\tilde{\rho}$  would manifest itself as a time dependence in an observable of some sort. This must not be the case if the ensemble is in equilibrium. As will be seen, usually in the solid state, after an excitation, the off diagonal elements of  $\tilde{\rho}$  decay to zero very much more quickly than the diagonal elements approach their equilibrium values; this will come to mean that  $T_2$  is very much shorter than  $T_1$ . This relatively fast decay of the off-diagonal elements comes about because the spin-spin term  $H_{SS}$  of Eq. 6 is much stronger than the spin-lattice term  $H_{SL}$ . In this case then it is possible to define a spin temperature through Eq. 38, different from that of the lattice. This may make calculations of spin-lattice relaxation times fairly straightforward, see Slichter (156).

Before Eq. 39 is solved for the FID experiment, it is appropriate to finally define the macroscopic magnetization  $\vec{M}$ :

$$\vec{M} = N \langle \vec{\mu} \rangle . \quad (40)$$

This implies, through Eqs. 32, 34, 35, 36, and 37 that

$$\begin{aligned} M_x &= \frac{N\gamma\hbar}{2} (\rho_{\alpha\beta} + \rho_{\beta\alpha}) \\ M_y &= \frac{N\gamma\hbar}{2i} (\rho_{\alpha\beta} - \rho_{\beta\alpha}) \\ M_z &= \frac{1}{2} N\gamma\hbar (\rho_{\alpha\alpha} - \rho_{\beta\beta}) \\ M_o &\equiv \frac{1}{2} N\gamma\hbar (\rho_{\alpha\alpha}^e - \rho_{\beta\beta}^e) , \end{aligned} \quad (41)$$

where  $M_o$  is the equilibrium value of  $M_z$ .

Now, the FID experiment will be analyzed using the equation of motion for the density matrix, Eq. 39. For the pulse phase of the experiment it will be assumed that the pulse will take a time much less than either  $T_2$  or  $T_1$ . Then the relaxation terms may be neglected, for now. An easier problem will be solved first. Assume that  $H_1$  is zero. Then only the  $H_0$  term of the Hamiltonian remains. Equation 39 then reduces to

$$\begin{aligned}\frac{d\rho_{\alpha\alpha}}{dt} &= \frac{d\rho_{\beta\beta}}{dt} = 0 \\ \frac{d\rho_{\alpha\beta}}{dt} &= -i\omega_0 \rho_{\alpha\beta} \Rightarrow \rho_{\alpha\beta} = \rho_{\alpha\beta}^0 e^{-i\omega_0 t} \\ \frac{d\rho_{\beta\alpha}}{dt} &= i\omega_0 \rho_{\beta\alpha} \Rightarrow \rho_{\beta\alpha} = \rho_{\beta\alpha}^0 e^{-i\omega_0 t}.\end{aligned}\tag{42}$$

The expressions for the magnetization, Eq. 41 then imply

$$\begin{aligned}M_x &= N\gamma\hbar \text{Re}(\rho_{\alpha\beta}^0) \cos\omega_0 t \\ M_y &= N\gamma\hbar \text{Im}(\rho_{\beta\alpha}^0) \sin\omega_0 t.\end{aligned}\tag{43}$$

So, it has been established that the macroscopic magnetization precesses about the  $\hat{z}$  axis, provided that the off diagonal elements of the density matrix are not zero initially (which they must be if the ensemble is in equilibrium). We now investigate the means by which these off-diagonal elements are made to assume nonzero values.

If we apply this most recent result to the rotating frame with  $H_1$  suddenly turned on to some finite value, then the Zeeman Hamiltonian

disappears from the commutator of Eq. 39. Since we are still ignoring the relaxation terms, the equation of motion in the rotating frame reduces to

$$\begin{aligned}\frac{d\rho'_{\alpha\beta}}{dt} &= -i\omega_1 \rho'_{\alpha\beta} \Rightarrow \rho'_{\alpha\beta} = \rho_{\alpha\beta}^{o'} e^{-i\omega_1 t} \\ \frac{d\rho'_{\beta\alpha}}{dt} &= i\omega_1 \rho'_{\beta\alpha} \Rightarrow \rho'_{\beta\alpha} = \rho_{\beta\alpha}^{o'} e^{i\omega_1 t} \\ \frac{d\rho'_{\alpha\alpha}}{dt} &= \frac{d\rho'_{\beta\beta}}{dt} = 0.\end{aligned}\tag{44}$$

Be reminded: the primes indicate that the density matrix is to be calculated in the rotating frame (interaction representation). We will further assume that the magnetization was initially along the Zeeman field (i.e. the off-diagonal elements of the density matrix in the laboratory frame are zero) and that the diagonal elements are at their equilibrium values. The magnetization in the  $\hat{z}'$  direction is now given by

$$M'_z = \frac{N\gamma\hbar}{2} (\rho_{\beta\alpha}^{o'} e^{i\omega_1 t} + \rho_{\alpha\beta}^{o'} e^{-i\omega_1 t}) .\tag{45}$$

At time,  $t=0$ , we use as the boundary condition that  $M'_z = M_z \equiv M_o$ , which leads to

$$\rho_{\alpha\beta}^{o'} + \rho_{\beta\alpha}^{o'} = \rho_{\alpha\alpha}^e - \rho_{\beta\beta}^e .\tag{46}$$

Then for a pulse duration of time,  $t$ , the  $z'$  component of the magnetization in the rotating frame is

$$\begin{aligned}
M_z' &= \frac{1}{2} \gamma \hbar N (\rho_{\alpha\beta}' e^{-i\omega_1 t} + \rho_{\beta\alpha}' e^{i\omega_1 t}) \\
&= \gamma \hbar N \operatorname{Re}(\rho_{\alpha\beta}' e^{-i\omega_1 t}) \\
&= M_0 \cos \theta,
\end{aligned} \tag{47}$$

where  $\theta$  is given by Eq. 11. Now we have established that the macroscopic magnetization is rotated away from the Zeeman field direction by an arbitrary angle,  $\theta$ . This opens the way for an understanding of the macroscopic FID. First, a minor philosophical digression.

It is valuable to recognize that the phase coherent nature of the rf excitation is directly responsible for the profoundly collective nature of the rotation of the entire macroscopic magnetization into the transverse plane. It is this aspect of magnetic resonance that allows us to bring such a quantum mechanical phenomenon into the macroscopic world of the laboratory. Without the phase coherence of the rf excitation the precessing transverse magnetization of each spinning particle will not be in phase; the signal then observed would be more akin to luminescence. With coherent excitation, though, the response is coherent -- indeed, the brief response is much like that of a low frequency laser -- see Macomber (155). We return to the FID, which is already in progress.

After the pulse, it is convenient to consider the effects of the relaxation terms in the Hamiltonian,  $H_R$ . For the diagonal elements of the density matrix, the laboratory frame is the most convenient. In the case of the off diagonal elements, the rotating frame is the easiest. The

equations of motion in the laboratory and rotating frame for the diagonal and off-diagonal elements are, respectively,

$$\begin{aligned}\frac{d\rho_{mm}}{dt} &= \frac{1}{i\hbar} [H_{SL}, \rho]_{mm} \approx \frac{\rho_{mm}^e - \rho_{mm}}{T_1} \\ \frac{d'\rho_{jk}}{dt} &= \frac{1}{i\hbar} [H_{SS}, \rho']_{jk} \approx \frac{-\rho'_{jk}}{T_2}, \quad j \neq k,\end{aligned}\tag{48}$$

where the Bloch approximation for the effects of relaxation has been made. The effects of the relaxation interactions have been approximated by assuming that they lead to simple exponential solutions for the density matrix. This is very close to the mark in many situations, however it is not always valid. If we apply the definitions of the macroscopic magnetization and transform back into the lab frame for the transverse components, we have the Bloch equations for the longitudinal and transverse components of the magnetization, respectively,

$$\frac{dM_z}{dt} = \frac{M_0 - M_z}{T_1}\tag{49}$$

$$\frac{d\vec{M}_{x,y}}{dt} = -(\gamma \vec{H}_0 \times \vec{M})_{x,y} - M_{x,y}/T_2.$$

For our FID experiment, the Bloch equations then imply a simple exponential decay of the transverse components of the magnetization. There will be more said about the spin-spin relaxation process in section F.



### E. The FID and Adiabatic Slow Passage Experiments

The FID experiment is probably the easiest condensed matter magnetic resonance phenomenon to visualize; while, the adiabatic slow passage (ASP) is the most commonly used magnetic resonance technique. The FID experiment is both rapid and sudden; while, the ASP experiment is diametrically opposed to the FID. It is both adiabatic (the opposite of sudden) and slow (the opposite of rapid). These four terms characterize the speed with which manipulations of spin system ensembles are carried out. Pake and Estle (159) and Slichter (156) deal effectively with their definitions.

The adiabatic slow passage experiment proceeds as follows. The sample is placed in the Zeeman field for a time (several  $T_1$ 's) sufficient to allow the dipoles to line up with the field. A small rf excitation is applied to the sample and left on throughout the experiment. The Zeeman field is initially far from satisfying the resonance condition, Eq. 5b. The field is slowly and steadily changed (usually increased). In the rotating frame, as the resonance condition is approached (there is always a finite width to the resonance, for the same reason that the FID decays--to be discussed in the next section), the effective field begins to differ appreciably from the Zeeman field (see Eqs. 9, 10). It diminishes in magnitude and swings down toward the  $\hat{x}$ - $\hat{y}$  plane. However,  $H_1$  is so weak and the sweep so slow that spin-lattice relaxation sets in before the magnetization can follow  $H_e$  (see Pake and Estle (159) or Slichter (156) for details). The result is that the magnetization precesses around the Zeeman field with a transverse component proportional to  $H_1$  and the population of spins

in resonance at a particular field value provided that the resonance does not saturate, i.e.  $\frac{1}{T_1}$  must be large compared to  $H_1^2$ . In practice, one fixes the rf frequency and sweeps the field; in principle, one could just as easily hold the field constant and sweep the rf frequency. There are at least two ways to detect this slow passage signal. The first method involves actually detecting the signal due to the precessing magnetization (here one sees the stimulated emission of the spin ensemble). The second method involves monitoring the absorbed power (here one sees the stimulated absorption of the spin system). In any case, the signal detected may be written,

$$S(\omega) = cM_0 H_1 f(\omega - \omega_0) , \quad (50)$$

where C is a constant and the intensity of the signal has been written as a function of rf frequency. The distribution function,  $f(\omega - \omega_0)$  is symmetric with respect to  $\omega_0$  and is usually called the lineshape function.

These two very different types of experiment, FID and adiabatic slow passage, yield the same information about the system. The spin ensemble may be viewed as a collection of oscillators that absorb and emit photons. The transition may go either way just as easily for the individual spin; however, when the entire ensemble is considered the transition probabilities must be weighted with the appropriate diagonal element of the density matrix. These individual spins interact with the net result that they do not all emit or absorb at exactly the Larmor frequency; rather, there is some distribution function  $f(\omega - \omega_0)$  which describes the resonance of the ensemble, this of course describes the ASP lineshape as per Eq. 50. If

there has been a disturbance of the ensemble such that the diagonal elements of the density matrix are no longer at their equilibrium values, for instance a  $90^\circ$  pulse, emission will be the favored transition. All of the individual dipoles will not emit with the same frequency, in fact there will be a distribution of frequencies given by the same function  $f(\omega - \omega_0)$ . If we sum the contributions of the individual dipole emissions we find that the observed FID is simply the Fourier transform of the ASP shape function,

$$M_x(t) = M_0 D \operatorname{Re} \left[ \int_{-\infty}^{\infty} f(\omega - \omega_0) e^{i\omega t} d\omega \right], \quad (51)$$

where  $D$  is a constant. The decay in the transverse magnetization comes about because the differing frequencies in the sum eventually begin to interfere destructively. One should note that  $\frac{1}{T_2}$  is proportional to the width of  $f(\omega - \omega_0)$ , on the general grounds of Fourier theory.

#### F. Relaxation of the Magnetization: Beyond the Bloch Equations

The relaxation term of the Hamiltonian for the average spin takes the form,

$$H_R(t) = -\gamma \overline{\vec{H}(t) \cdot \vec{J}}, \quad (52)$$

where  $\vec{H}(t)$  is a randomly fluctuating field. This field could be due to anything, in general; in our case the field is probably the dipolar field of another spin. Some insight into the relaxation process that is brought

on by fluctuating dipolar fields may be obtained by investigating the Hamiltonian for the dipolar interaction between two spins separated by a distance,  $r$ . This Hamiltonian is

$$H_D = \frac{\gamma_1 \gamma_2 \hbar^2}{r^3} (A + B + C + D + E + F) (1 - 3\cos^2 \xi) \quad (53)$$

$$H_D \rightarrow \frac{\gamma_1 \gamma_2 \hbar^2}{r^3} (A + B) (1 - 3\cos^2 \xi)$$

where the  $C$ ,  $D$ ,  $E$ , and  $F$  terms are ignored; they lead to resonance at the harmonics of the Larmor frequency (these terms may become important when the dipolar interaction is the perturbation responsible for spin-lattice relaxation).  $\xi$  is the angle between the Zeeman field direction and the vector joining the two spins in space. Slichter (156) should be consulted for details. The remaining terms,  $A$ ,  $B$ , are given by

$$A = J_{1z} J_{2z} \quad (54)$$

$$B = -\frac{1}{4} (J_1^+ J_2^- + J_1^- J_2^+),$$

where  $J^+$  and  $J^-$  are respectively the raising and lowering operators for angular momentum (they are of course directly related to the transverse components of the angular momentum). Thus it can be seen that the  $A$  term represents the effects of the dipolar field in the  $\hat{z}$  direction of one spin upon the corresponding component of the other's dipole in that direction. The  $B$  term on the other hand involves the interaction of the transverse components of the dipolar field due to one dipole with the transverse components of the other's dipole. The  $B$  term then is responsible for mutual spin flips between neighboring dipoles.

The spin-spin relaxation in the FID experiment may be understood on the following grounds. The  $\tilde{B}$  term in the dipolar Hamiltonian is responsible for initiating mutual spin flips between neighboring spins; this communicates a sense of the spin temperature throughout the ensemble. Every such communication disrupts the phase of the off-diagonal elements of a  $\tilde{D}$  matrix, such that after a time of the order of  $T_2$  the sum over the ensemble of the  $\tilde{D}$  matrices, which is just the off diagonal elements of the density matrix, tends to zero. The  $\tilde{A}$  term adds to this dephasing by creating different effective Zeeman fields (due to the dipolar fields in the  $\hat{z}$  direction), and thus different effective Larmor frequencies at each spin site. Finally, the transverse components of the magnetization go as the off-diagonal elements of the density matrix and form the FID.

We will be analyzing signals in frequency (or equivalently field) space. Therefore, it is appropriate to consider the effects of the dipolar Hamiltonian on the line shape function,  $f(\omega - \omega_0)$ . Van Vleck has done this by the method of moments (see Slichter (156) or Abragam (163)). Considering the dipolar Hamiltonian, the second moment is

$$\overline{\Delta\omega^2} = M_2 = \frac{3}{5} \gamma^4 \hbar^2 J(J+1) \sum'_{j,k} \left( \frac{1}{r_{jk}^6} \right), \quad (55)$$

where the Hamiltonian of Eq. 53 has been used and its interaction between all pairs of the ensemble calculated. The prime in the sum indicates that it is to be carried out over all pairs. The angle  $\xi$  of Eq. 53 has been averaged over all possible values (this will be appropriate for the application of the formula in this work to amorphous materials). The

definition of the second moment of the lineshape function is

$$\overline{\Delta\omega^2} \equiv \int_{-\infty}^{\infty} f(\omega - \omega_0)(\omega - \omega_0)^2 d\omega \quad . \quad (56)$$

Note that the lineshape function  $f(\omega - \omega_0)$  is normalized to unity. Higher order moments may be calculated analogously. The values of these higher moments can also be calculated in terms of the dipolar interaction to yield results similar to Eq. 55. Abragam (163) or Slichter (156) should be consulted for details.

If the pulse of the FID experiment is left on longer than the time prescribed for a  $90^\circ$  pulse, Eq. 11, one may, as long as relaxation does not set in, swing the magnetization through  $180^\circ$  or any arbitrary angle. This implies that the populations given by the diagonal elements of the density matrix may be varied in a cyclical fashion. The first half of the cycle is stimulated absorption of magnetic energy; while, the second half is stimulated emission. So, in the case of a spin system being at some temperature higher than that of the lattice, irradiation with resonance frequency light may induce emission--if this irradiation comes from within the sample the emission may be called spin-lattice relaxation.

In cases where the members of the spin ensemble are in appreciable relative motion, the dipolar coupling provides significant thermalization to the lattice of the spin energy: the relative motion causes time dependent fields,  $\vec{H}(t)$ , to be felt at the spin sites. If enough of this motion has frequency components near the Larmor frequency, stimulated

emission results. There will also be a reciprocal force on the spins due to the field gradients experienced; hence, the emitted energy is transformed into thermal kinetic energy. In these cases, the mechanism of spin-spin temperature communication (mutual spin flips) is the same as the temperature communication to the lattice; with the result that  $T_2$  approaches  $T_1$  --this is called the fast motion or motional narrowing regime. This will not be our case. We will be concerned with the case of a very weak coupling of the spin ensemble to the lattice. Then, the spins will come to a common temperature after a disturbance a very long time before the ensemble's temperature becomes that of the lattice;  $T_2 \ll T_1$ . In this case the relaxation often comes about by the interaction of a few spins of the ensemble with some, so called, relaxation centers. The rest of the ensemble then adjusts its temperature via the mutual spin flips of the dipolar Hamiltonian. This process is called spin diffusion and takes place in times of the order of  $T_2$ ; more will be said about this in Chapter IV.

To understand spin-lattice relaxation is to understand the occurrence of magnetic fields which oscillate with approximately the Larmor frequency, where the source of these fields is within the sample. It is possible to solve Eq. 39 with the Hamiltonian of Eq. 52 in some cases. Slichter (156) or Abragam (163) are good sources of the details. First, one notes that if  $H_0$  is the only term in the Hamiltonian, then the diagonal elements of the density matrix are constant. When the relaxation Hamiltonian is turned on the populations begin to change toward their equilibrium values; therefore, in the spin 1/2 case

$$\frac{d\rho_{\alpha\alpha}}{dt} = \frac{-d\rho_{\beta\beta}}{dt} = -\frac{1}{T_1} (\rho_{\alpha\alpha} - \rho_{\alpha\alpha}^e) . \quad (57)$$

The solution of Eq. 39 then yields

$$\frac{1}{T_1} = \frac{2}{\hbar^2} [\sum_q K_{\beta\alpha}^q(\beta-\alpha)]; \quad \beta = \alpha \equiv |\omega_o| . \quad (58)$$

The  $K_{\beta\alpha}^q$  are summed over the spatial components of the fluctuating field that lead to relaxation. For  $T_1$  processes, this would only be the transverse components (again, only  $J_x$  and  $J_y$  couple the diagonal elements)<sup>1</sup>. Each term  $K_{\beta\alpha}^q$  can be written,

$$K_{\beta\alpha}^q(\omega_o) = \gamma^2 \hbar^2 |\langle \beta | J_q | \alpha \rangle|^2 k_q(\omega_o) . \quad (59)$$

The matrix element in the above is identical to that which would be employed had we used the Fermi golden rule to calculate the transition rate. The factor,  $k_q(\omega_o)$  is a spectral density function which is the Fourier transform of the time dependence of the randomly fluctuating field. In the case of a field that fluctuates "randomly" between  $\pm \hbar_q$ , with correlation time  $\tau_c$ , one has

$$k_q(\omega_o) = 2\hbar_q^2 \tau_c / (1 + \omega_o^2 \tau_c^2) . \quad (60)$$

---

<sup>1</sup>This is an oversimplification. One should consider  $q$  to be a generalized coordinate; for some cases  $H_q$  could represent the longitudinal component of a fluctuating field and  $J_q$  an operator involving transverse components (that couple up and down spin) of the spin system's angular momentum. The simple dipolar Hamiltonian including the nonsecular terms,  $C$  and  $D$ , of Eq. 53 is an example, see p. 289 of ref. 163. In this case fluctuations of the longitudinal field produce spin-lattice relaxation.



We say "randomly" because if the fluctuations were completely random the spectral density would be white, and there would be no finite  $\tau_c$  ( $\tau_c \rightarrow 0$ ). For the spin 1/2 ensemble, using Eqs. 58-60, we may express the spin-lattice relaxation rate as,

$$\frac{1}{T_1} = 2\gamma^2 \frac{h_o^2}{3} \frac{\tau_c}{1 + \omega_o^2 \tau_c^2} \quad , \quad (61)$$

where an isotropically fluctuating field ( $\pm h_o$  for each component) has been assumed (see Slichter (156)). There are other expressions for the spin-lattice relaxation rate. All of them, however, make use of the idea of a field whose components fluctuate with frequencies near the Larmor frequency. Thus, Eq. 61 contains the basic elements of spin lattice relaxation that will concern us.

The following chapter will deal with the experimental realization of magnetic resonance for the proton and electron, both spin 1/2 particles, in amorphous silicon hydrides, and some details of sample preparation.

### III. EXPERIMENTAL METHODS

#### A. Sample Preparation

##### 1. Sputtering parameters

The a-Si(H) samples for this study were deposited on Al foil substrates using the reactive sputtering technique. The sputtering system used was a modified Ion Equipment Corporation capacitively coupled model (see Appendix A, and ref. 35b for details).

Several sputtering parameters have great impact upon the resulting material qualities. Most importantly, variation of the hydrogen gas partial pressure during sputter deposition results in a variation of total H content in the deposited films. As mentioned in Chapter I, sputtering with high rf powers reduces the incidence of dihydride bond formation to virtually undetectable levels. The films dealt with in this study were all deposited from a high power rf plasma: the applied rf power density was approximately  $3.0 \text{ W/cm}^2$  in all cases. The resulting films had undetectable dihydride bond densities on the basis of ir measurements in which the  $840 \text{ cm}^{-1}$  and  $890 \text{ cm}^{-1}$  bond bending modes were monitored; see Jeffrey (35a, 35b). The primary object of this study was a series of six a-Si(H) samples with monohydride bonding and H concentrations ranging from ~4 at. % to ~17 at. %.

We will also be briefly concerned with several samples that have varying amounts of deuterium substituted for hydrogen. This was accomplished by mixing deuterium gas with hydrogen gas in the sputtering chamber. These samples, also, have been deposited from a high power rf

plasma, and monohydride bonding is presumed to be the predominant means of generic hydrogen incorporation.

Table 1 presents the sputtering parameters and some other details for all samples dealt with in this study.

## 2. Bulk sample preparation

The accumulation of hydrogen NMR signals of sufficient strength to allow meaningful analysis in an efficient manner requires that the sample quantity be very much larger than that normally prepared for other measurements. This necessitated development of a "bulk sample" collection technique.

To avoid uncontrolled self-bias effects on the target-to-substrate voltage it is necessary that the substrate be sufficiently grounded to the holder (see Appendix A). It was found that an effective means of accomplishing this was to bond Al foil to a pyrex plate (3M spray adhesive was used), allowing sufficient overlap of the Al foil unto the underside of the pyrex plate. In this way, an efficient path to ground is formed from the top of the substrate to the substrate holder by simply placing the substrate onto the holder. This scheme has enabled routine bulk sample deposition with approximately  $380 \text{ cm}^2$  of coverage, requiring plasma stability over many hours to produce films of about  $25 \text{ }\mu\text{m}$  thickness.

The Al foil with the deposited a-Si(H) film was then peeled from the pyrex plate. The resulting composite of Al foil, a-Si(H) film, and 3M adhesive was then placed in a dilute HCl acid etch. The 3M adhesive floats and was carefully skimmed from the surface of the acid etch bath.

Table 1. a-Si(H) sample sputtering parameters, sample masses, and hydrogen concentrations from NMR spin counts

Sample label	rf power density (W/cm <sup>3</sup> )	DC bias (kV)	Ar flow rate (cc/min)	Reactant gas (H <sub>2</sub> and/or D <sub>2</sub> ) flow rate (cc/min)	Sputtering chamber pressure (in Torr)	NMR sample mass (mg)	EPR sample mass (mg)	H concentration by NMR spin count (%)
C45	3.3	2.0	26	3.0 H <sub>2</sub>	28	317.5	15.8	4%
C52	3.1	1.9	27	5.5 H <sub>2</sub>	34	474.2	15.9	7%
C51	3.1	1.9	28	13.0 H <sub>2</sub>	33	500.6	19.5	11%
C70	2.9	1.9	30	24.0 H <sub>2</sub>	-- <sup>a</sup>	679.8	18.6	14%
C64	3.1	1.9	30	23.0 H <sub>2</sub>	30	819.0	16.5	15%
C53	3.1	1.9	27	36.0 H <sub>2</sub>	32	468.8	16.9	17%
C81	3.0	1.8	30	16.0 H <sub>2</sub>	-- <sup>a</sup>	287.8	10 <sup>c</sup>	5%
				11.4 D <sub>2</sub> <sup>b</sup>				
C83	3.1	1.9	30	10.0 H <sub>2</sub>	-- <sup>a</sup>	740.3	740.3	not meas.
				6.4 D <sub>2</sub> <sup>b</sup>				
C88	3.0	1.8	30	18.0 H <sub>2</sub>	-- <sup>a</sup>	652.9	13 <sup>c</sup>	7%
				10.0 D <sub>2</sub> <sup>b</sup>				
C89	3.1	1.9	30	None	-- <sup>a</sup>	None	28.4	not meas.

<sup>a</sup>The value of the chamber pressure was not available, presumably, it was approximately 30 m Torr.

<sup>b</sup>The deuterium flow rates were estimated from the leak valve setting.

<sup>c</sup>Estimates, was not weighed.

The Al was, of course, etched from the a-Si(H) film and dissolved into solution. The resulting flakes of a-Si(H) were then carefully filtered from the acid solution and rinsed several times in distilled water.

The samples were dried in an oven at approximately 100 C to drive off adsorbed water, and subsequently placed in cleaned 10 mm O.D. quartz NMR tubes. To improve the filling factor, the flakes of sample were broken down mechanically to approximately 100  $\mu$ m size. The tubes were then evacuated and allowed to degas for several minutes, filled with Ar at a pressure of approximately 0.5 atm, and finally sealed.

Samples produced with these sputtering parameters (except possibly those sputtered with the highest H flow rates) have been shown not to degrade quickly upon exposure to the atmosphere; nonetheless, atmospheric exposure was limited to approximately one day for each sample.

### 3. Documentation of contamination levels

Initially, the possibility of Al migration into the bulk of the sample was a concern. For this reason, and as a general precaution, Auger surface analyses and spark source mass spectroscopic analyses have been performed on several of the samples in the series. The Auger analysis indicated no observable Al contamination: less than 0.5% (the actual level is probably much lower than that). The results of the mass spectrometric analysis are given in Appendix B; the most significant bulk contaminant detected was Ar. Other major contaminants, C, N, and O are thought to be mostly surface dirt. Ar should have no effect on the material other than the creation of network strains due to the incorporation of Ar atoms at

interstitial sites in the a-Si network—it should be acknowledged that this could lead to an increase in the incidence of microvoid creation in the network.

## B. The Magnetic Resonance Probe

Before discussing the magnetic resonance spectrometer as a whole, it is appropriate to touch upon the rudiments of magnetic resonance signal detection (as opposed to noise reduction, signal amplification, etc). The heart of all magnetic resonance detectors is the probe.

### 1. The quality factor (Q) of the probe

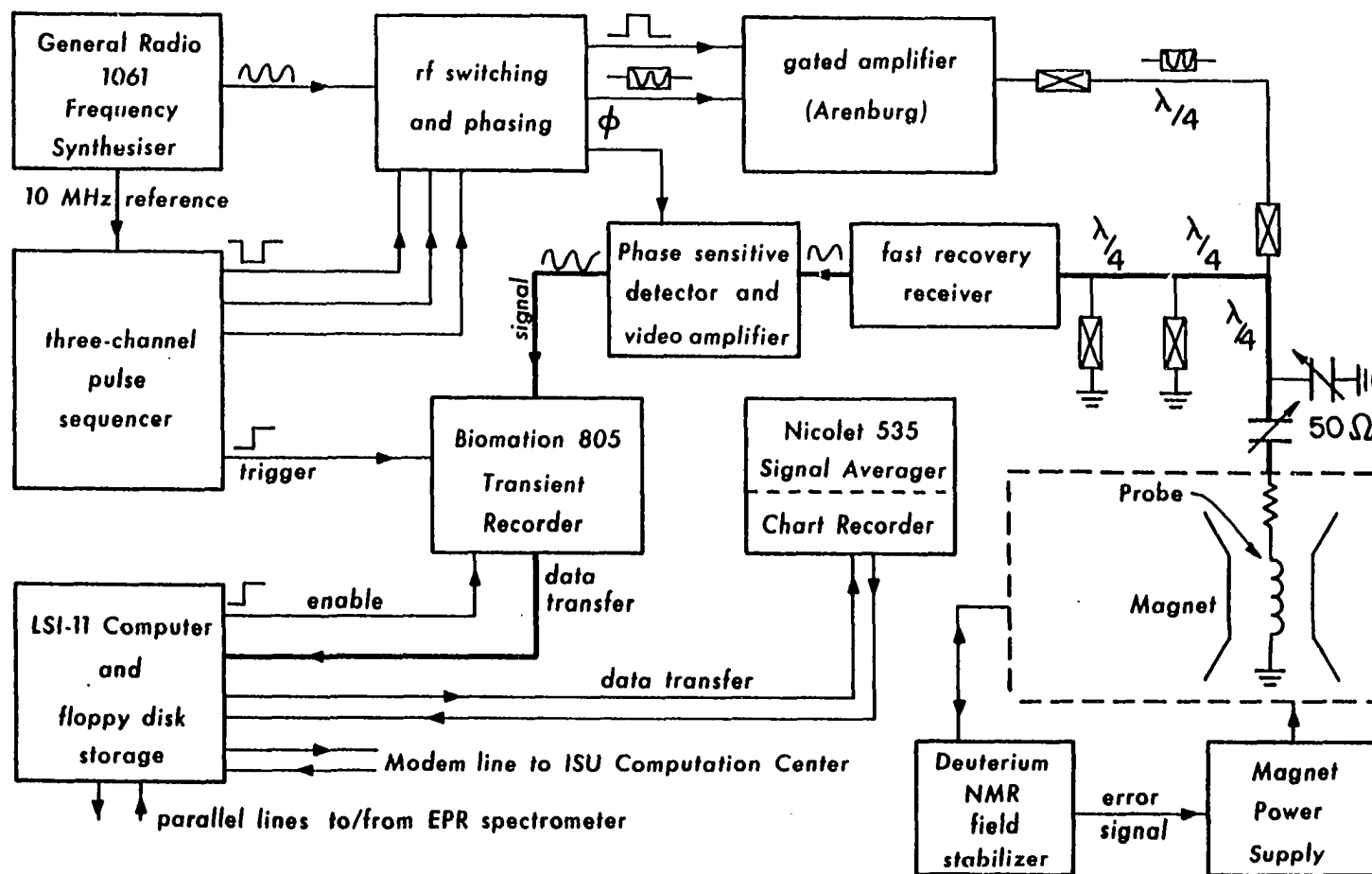
The quality factor may be defined as the ratio of stored energy to dissipated energy per cycle (166, 167). The stored energy is the electromagnetic field energy, and the dissipated energy may be due to resonant absorption or Ohmic resistance. It may be shown (166) that this definition of Q is equivalent to the ratio of the operating frequency of the probe to its bandwidth. So, high Q probes are relatively narrow banded and capable of storing more electromagnetic energy. As a result, high Q probes are more sensitive detectors of magnetic resonance; in fact, the observed signal intensity is proportional to the Q of the probe (166, 167).

### 2. The pulse NMR probe

The circuit for the type of probe used in this work appears in Fig. 4;  $Q \sim 40$  for the actual probes used. The inductor is a coil of 10–15 turns of 15 gauge copper wire. This coil is the transmitter of the oscillating magnetic field  $H_1$ . It is carefully wound to ensure optimized  $H_1$  field

Fig. 4. A block diagram of the pulse NMR spectrometer used for all NMR measurements is presented here  
The heavy line indicates the path of the NMR signal. See text for principles of operation.

# TORGESON/HORNUNG/ADDUCI PULSE NMR SPECTROMETER





homogeneity. The sample, of course, rests within the coil. The variable capacitors permit the probe to accommodate samples with a wide range of electrical and magnetic susceptibility and still tune. The probe is "tuned" when its impedance is a purely resistive 50 Ohms at the frequency of operation. This matches the characteristic impedance of the coaxial cable leading to the probe and therefore, maximizes the power coupled to the probe and the signal emanating from it.

Detection is accomplished via the same coil that is responsible for transmitting the excitation; the precessing nuclear dipoles create oscillating magnetic fields which induce oscillating voltages in the coil.

### 3. The EPR probe

The properties of electromagnetic waves at this frequency, several Gigahertz, require that a resonant cavity be the actual device that radiates to the sample (as opposed to the simple coil in the NMR case). The cavity used here was a Bruker ER 4102 ST,  $Q \sim 6000$ . The adjustable iris, visible only as a small aperture between the waveguide and cavity in Fig. 7, takes the place of the capacitors of the NMR probe. Changes in the effective iris diameter compensate for differing magnetic and electric susceptibilities, thereby allowing the cavity to be critically coupled to the waveguide (impedance matching). The reciprocal of the effective  $Q$  of the cavity plus sample is given by the sum of the reciprocal  $Q$ 's of each (166). During the course of the ASP experiment the sample will pass through resonance and the sample  $Q$  will decrease dramatically. This creates a change in the total  $Q$ ; the cavity plus sample will no longer be critically coupled and microwaves will be reflected towards the circulator

of Fig. 7. The detection of this reflected radiation will be discussed later.

Since  $Q$  is directly proportional to the stored field energy, the cavity  $Q$  may be increased appreciably by the insertion of material with relatively high dielectric into the cavity. This not only will effect the apparent signal magnitude, but will also shift the frequency at which the cavity tunes. This effect is a necessary consequence of the use of quartz dewars and dewar inserts to be discussed later.

### C. Pulse NMR Experimental Techniques

#### 1. The spectrometer

It is convenient to walk through the FID experiment—highlighting the physical processes that occur—to illustrate the principles of the spectrometer's operation.

The excitation of the spin system begins with the generation of a monochromatic continuous wave (cw) signal ( $\sim 35$  MHz in our case) at the frequency synthesizer (see Fig. 4). Pulses of rf waves are then created by the gating process in sequences which are setup in the hardwired pulse sequencer (or programmer (168)); phase information is simultaneously passed to the phase sensitive detector. Synchronous gating at the gated amplifier permits amplification of the pulse only. The diode boxes, placed at  $\lambda/4$  intervals between the gated amplifier and the probe, ensure that most of the high power rf pulse couples through the coaxial cable to the probe, while preventing the much weaker FID signal, to come, being shunted away from the receiver to the output of the gated amplifier (169, 170).

The probe (being previously tuned to the frequency of the rf,  $\nu_0$ ) is coupled to the coil at maximum efficiency. The current through the coil is forced to oscillate at the operating frequency,  $\nu_0$ , which, of course, sets up the resonant  $H_1$  field oscillating at the Larmor frequency of the sample nuclei within the coil (assuming that the resonant value of the field  $H_0$  has been selected).

The diode shorts between the probe and the receiver are designed to present a high impedance to the incoming pulse (169, 170); some rf power will pass through in spite of this precaution and the receiver will temporarily saturate. The receiver has been designed with three stages of "limited" amplification (170). This will limit the absorbed rf power, thereby limiting the dead time of the receiver.

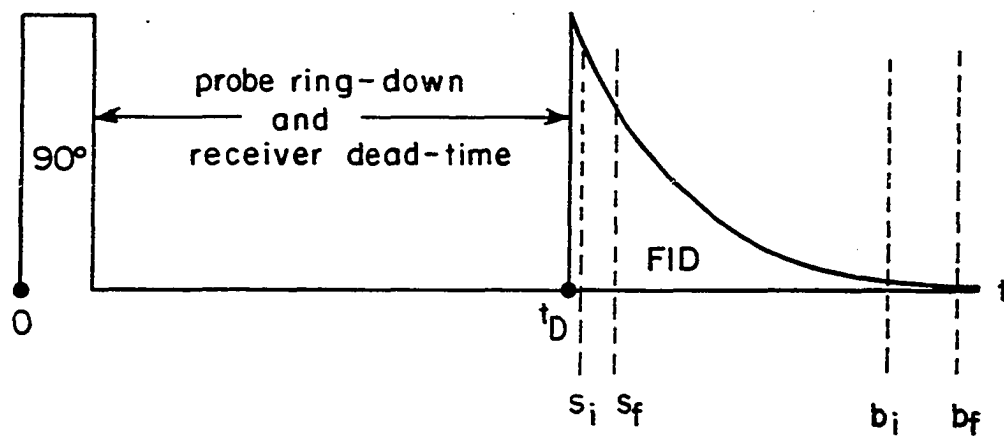
After the pulse has been absorbed by the probe, the latter will continue to oscillate at the resonance frequency (due to the stored field energy of a device with a nonzero  $Q$  as discussed in Section III.B.1). This "ringing" of the probe creates further saturation of the receiver and thus increases the dead time.

Of course, while all of this is happening the nuclear spins are precessing, and since the receiver will always be dead for at least a short time (see Fig. 5a) some of the FID will not be detected. There is, therefore, a compromise to be sought between the increased signal that obtains with large  $Q$ , and the decrease in receiver deadtime with small  $Q$ . For this work, the various probes used produced deadtimes requiring trigger delays of 8  $\mu$ s to 10  $\mu$ s (see Fig. 5a). These trigger delays are sufficiently fast relative to the measured spin-spin relaxation times that most of the information contained in the FID is captured.

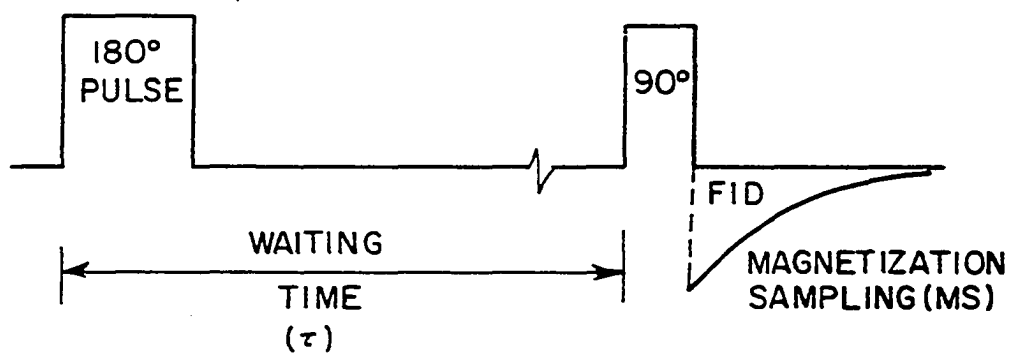
Fig. 5. Experimental details of the three basic NMR measurements discussed here are presented

- (a) This depicts the magnetization sampling (MS) experiment. After the receiver recovers, the Biomation transient recorder (see Fig. 4) captures the FID signal. The measurement window is specified by the initial,  $S_i$ , and final,  $S_f$ , signal channels; while the baseline window is specified by the initial,  $b_i$ , and final,  $b_f$ , baseline windows. See text
- (b) This is a schematic of the  $180^\circ$  pulse and magnetization sampling sequence,  $[180, T, MS]$ , that constitutes the inversion recovery  $T_1$  measurement technique. Note that  $\tau$  is much greater than either pulse width for our cases and that this diagram depicts a longitudinal magnetization which has not yet recovered even to zero
- (c) The FID pictured is being detected with the operating frequency,  $\nu_{op}$ , offset below the Larmor frequency,  $\nu_o$ , by an amount  $\nu_{os} = \nu_o - \nu_{op}$ . This transforms (via (FFT) into the lineshape on the right

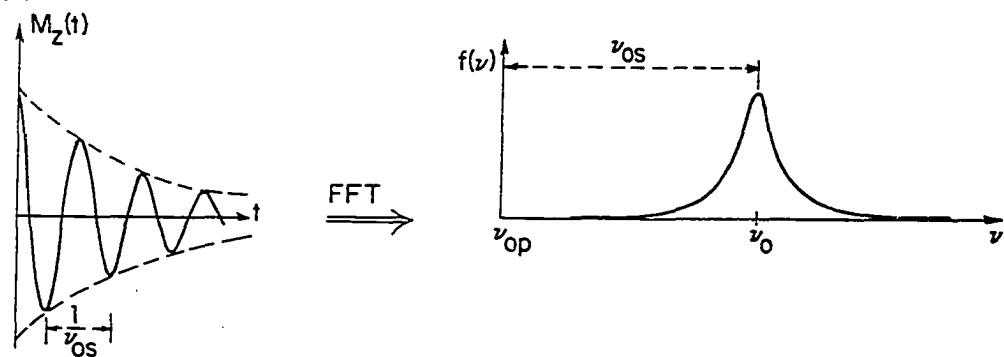
(a)



(b)



(c)



That portion of the FID that is picked up by the receiver is amplified and passed to the phase sensitive detector and video amplifier. This phase sensitive detection process narrows the bandwidth (centered around  $\nu_0$ ) considerably, providing a vast improvement in signal to noise. The cleaned-up FID signal is then captured by the Biomation transient recorder.

The transient recorder was usually operated at the fastest acquisition rate, .2  $\mu$ s/channel; there are a total of 2K (2048) channels of information where each channel stores the digitized value of the signal with 8-bit precision. This captured and digitized signal is then transferred to the LSI-11 minicomputer where several types of data manipulation are possible. The two most often used manipulations are features of distinct software packages that are rather affectionately dubbed Bionic and Alvin. These we will now discuss.

## 2. The FID as a magnetization sampler: Bionic

It is often necessary to know the value of the longitudinal magnetization,  $M_z$ , during the course of a magnetic resonance experiment. The accumulation of this information will be called magnetization sampling, and is the subject of this section.

Bionic (171) is a collection of assembler (DEC Macro-11 language) and Fortran routines that provide for transfer of data between the Biomation transient recorder and the Nicolet signal averager, disk storage of data, and a small amount of number crunching. In particular, Bionic calculates a number which is proportional to  $M_z$ . The calculation is done in accordance with the following formula:

$$MS \equiv \sum_{n=s_i}^{s_f} B_n - \left( \sum_{n=b_i}^{b_f} B_n \right) \frac{|s_f - s_i|}{|b_f - b_i|} \quad (62)$$

The subscripted B's stand for values that have been collected from the Biomation transient recorder; Fig. 5a should be consulted for the definitions of the remaining symbols. MS stands for the measured or sampled magnetization. Equation 62 then represents a sampling of several points at the beginning of a FID (it is convenient to call this the measurement window). The effects of any arbitrary DC offset in the recorded signal are taken into account by also sampling the "baseline" of the signal (call this the baseline window), normalizing, and subtracting from the measurement window. Of course, the baseline must be sampled well after the free induction signal has decayed. A measurement window of 32 points and a baseline window of 512 points were typically used. The number that is calculated from Eq. 62 is then passed to one of the channels in the Nicolet signal averager.

Magnetization sampling was used for the following two types of experiment.

a. NMR spin counting For the proper interpretation of proton NMR data in  $\alpha$ -Si(H), it becomes necessary to have a fairly good estimate of the amount of hydrogen in each sample. To this end, protons were counted by performing several room temperature magnetization sampling experiments with the spin system in equilibrium with the lattice. Equation 41 clearly shows that the number of spins is proportional to the equilibrium magnetization. Therefore, Bionic furnishes a value proportional to the number of

spins in the sample via Eq. 62. This procedure is automatically repeated a minimum of 20 times, with the values obtained placed in consecutive channels of the Nicolet.

An average of the several values placed into the Nicolet is easily calculated. The same procedure is repeated with a standard sample of water whose mass is well known. A comparison of the two numbers obtained for the a-Si(H) sample and the water standard will then directly provide the total number of protons in the sample.

It is important to note that the  $T_2^*$  (see III.C.5.b) of the water standard is much longer than that of the a-Si(H) samples. A proportionately larger sampling time (in the transient recorder) is used for the water standard runs; this ensures that the value calculated from Eq. 62 estimates the magnetization just after the deadtime, equivalently for both cases. However, the magnetization for water will not decay as quickly as that for a-Si(H) during the deadtime; this leads to a slight error in the spin count which is easily corrected; this correction will be briefly dealt with in Chapter IV. By comparing spin counts made with several different water standards, the total error in the measurement is estimated to be 20%.

b. Spin-lattice relaxation time,  $T_1$ , measurements using the inversion

recovery technique      The inversion recovery measurement is made by inverting the magnetization and sampling it at some time,  $\tau$ , after the 180° inversion pulse, during its recovery to equilibrium with the lattice. See Fig. 5b. The sampling must be done after the spin system has



established a temperature, i.e.  $\tau \gg T_2$ . It will be helpful to abbreviate the magnetization sampling step as MS. The sequence of events may be briefly capsulized as:  $[180^\circ, \tau, \text{MS}]$ . The sequence  $[180^\circ, \tau, \text{MS}]$  is repeated with the values of  $\tau$  incremented automatically by the auto increment module of the pulse sequencer (172). The repetition rate of the sequence  $[180^\circ, \tau, \text{MS}]$  is governed by the main clock time of the sequencer and must be slow enough to ensure that the magnetization totally recovers to the equilibrium value between  $[180^\circ, \tau, \text{MS}]$  sequences. A main clock time of at least seven times  $T_1$  was used in all cases here unless noted otherwise. The inversion recovery sequence places the initial condition  $M_z(0) = -M_0$  upon the longitudinal Bloch equation, Eq. 49. The solution is,

$$M_z = M_0 (1 - 2e^{-\tau/T_1}) \quad (63)$$

Unless noted otherwise all  $T_1$  values quoted in Chapter IV are arrived at by fitting data collected by the  $[180^\circ, \tau, \text{MS}]$  technique to Eq. 63. It should be recognized that Eq. 63 may not always be appropriate; the Bloch equation may not be valid, or the possibly inhomogeneous nature of the material may lead to pockets of magnetization that are at different temperatures following the  $180^\circ$  excitation.

### 3. The FID as a source of lineshape information: Alvin

The spectrometer operates in essentially the same manner as in the magnetization sampling experiments with one important difference: The spectrometer is initially set up to produce an on-resonance FID, pictured in Fig. 5a. Then the frequency generated by the synthesizer is shifted

away from exact resonance a slight amount (usually 100 kHz). The signal seen will be the off-resonance FID, or interferogram, of Fig. 5c.

It may at first seem surprising that one sees a FID at all since the initial cw rf is 100 kHz away from resonance; this is actually several times the linewidth of the observed a-Si(H) resonance in frequency space. The spin system is able to absorb energy because it is irradiated with a pulse. The frequency spectrum of cw radiation is of course proportional to the Dirac delta function; it is easily demonstrated by Fourier theory (167) that the spectrum of a pulse depends upon the pulse duration. In general for a variety of pulse shapes the approximate relation

$$\frac{1}{\Delta t} \approx \Delta \nu \quad (64)$$

holds, where  $\Delta t$  is the pulse length and  $\Delta \nu$  is the width of the frequency spectrum in a full-width-at-half-maximum sense (FWHM). The longest 90° pulses for this work were  $\sim 2.5 \mu\text{s}$  (this was set on resonance, we will see that it will not actually be a 90° pulse off-resonance). Using Eq. 64, we find that the frequency spectrum of the worst case 90° pulse is 400 kHz wide. This provides plenty of overlap with the Larmor frequency and explains why the spin system absorbs energy even with an "off-resonance" excitation.

One further point must be made about this excitation. An appeal to Eq. 8 clearly shows that the magnetization will not precess around the  $\hat{x}$  direction when the resonance condition, Eq. 5b, is not precisely met. Therefore, the precession around  $\vec{H}_e$  given by Eq. 8 will not put the

magnetization in the  $\hat{x}$ - $\hat{y}$  plane. In our case the  $H_1$  field is at least 23 Gauss; an offset of 100 kHz implies that the magnetization is only a little more than  $45^\circ$  away from the z-axis after the "90° pulse." This is of no real consequence because the magnetization is tipped away from the z-axis in any event; the initial magnitude of the transverse component (the only component detected by the coil) is simply not as large as it might be. So, the FID will proceed as usual with smaller initial magnitude.

The phase information passed to the phase sensitive detector by the frequency synthesizer is, however, a monochromatic frequency signal. The detector is therefore "out of step" with the Larmor precession frequency and the interferogram of Fig. 5c results.

Alvin (173) is a rather extensive program that has several features of interest to us. Those are the ability to transfer the interferograms captured by the Biomation to computer memory where they are averaged in a buffer (the signal to noise ratio goes as  $\sqrt{N}$  where  $N$  is the number of passes, (167)), perform fast Fourier transforms (FFT) on the interferograms, and communicate data to the ISU computation center for more sophisticated analysis (such as least squares fitting of lineshapes).

The proton NMR lineshapes presented in this study are FFT's of signal-averaged interferograms. The least squares fitting was done with a program (174) based upon the standard routines available at the ISU computation center.

#### 4. Temperature variation, control, and measurement

NMR measurements (primarily  $T_1$ ) were made over a wide range of temperatures. This required five different sample heating or cooling

schemes. These will be briefly outlined below, by temperature range.

a. 4.2 K A probe with a large enough diameter coil was employed to accommodate a standard Pope He finger dewar. The sample was then maintained at liquid He temperature by immersion into the bath.

b. 10-130 K (excluding temperatures near 77 K) A standard Varian quartz dewar insert tube was placed inside the coil of the same type of probe as in a. An evacuated brass transfer dewar connected the dewar insert with an He storage dewar. An Ohmic heating element submerged in the storage dewar provided an over pressure of cold He gas by simple boiling. The pressure gradient forced cold He gas to flow through the dewar insert past the enclosed sample. Stable temperatures as low as 10 K were attained in this fashion without benefit of any of the standard control feedback loops; the only control used was the voltage applied to the dewar heating element.

Temperatures were measured with an in-house fabricated Au-Fe (0.03) vs. Cu thermocouple in the range 10-50 K, and with a in-house fabricated Cu vs. Constantan thermocouple for the range 50-130 K. In both cases, the thermocouple was placed approximately 1.0 cm "downstream" of the sample in the He gas flow.

c. 77 K Here the arrangement was completely analogous to that in a., except that a liquid N finger dewar was used instead.

d. 130-300 K For this range it was possible to use a probe with a smaller diameter coil. The coil diameter is just large enough to accommodate the 10 mm O.D. NMR tube; the cooling fluid (cold N<sub>2</sub> gas) is forced to circulate through a brass vacuum jacketed chamber which contains

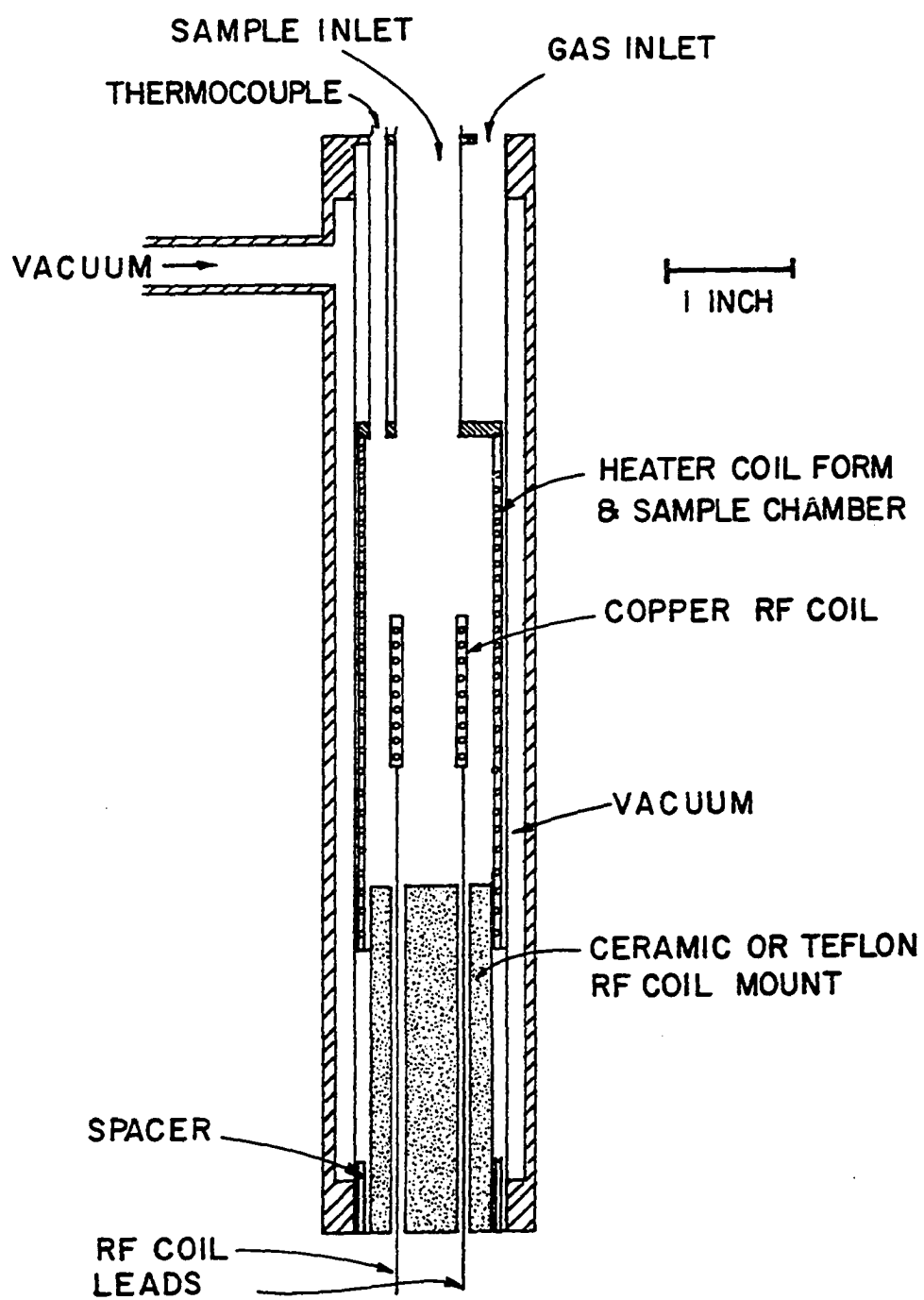
the coil with sample and a noninductively wound heating element, see Fig. 6.

The cold  $N_2$  gas flow was obtained by boiling the liquid in a storage dewar. Connection to the probe was facilitated by insulated surgical tubing. The measurement thermocouple provided a feedback voltage which was compared to a preset voltage. The difference in voltages was used as an error signal to drive the probe heater. This closed feedback loop provided excellent thermal stability over very long times. Commercial (Omega) and in-house fabricated Cu vs. Constantan thermocouples were used for temperature measurement.

e. 300-620 K Dry  $N_2$  gas from the building lines was forced into the probe of d. The noninductively wound heater element served to heat the gas. The feedback loop of d. was also employed for stability.

f. Thermocouple calibration For all thermocouple schemes the standard reference bath was water and ice. The indicated measurement temperatures were calibrated by immersing a measurement thermocouple in one of three baths: liquid He, liquid  $N_2$ , or water and ice, depending upon the operative range of the thermocouple. The measured temperature was always within a few degrees of the actual sample temperature. Nonetheless, calibration of the actual sample temperature was done by fixing a second thermocouple directly to a dummy sample tube and recording both the measurement thermocouple and sample thermocouple readings for several temperature points for each thermocouple arrangement. (Noise considerations make it impossible to directly measure the sample temperature during an NMR experiment.) Calibration graphs were then constructed and used for

Fig. 6. This NMR probe allows measurements to be obtained at temperatures from  $\sim 110$  K to  $\sim 650$  K (or higher if a ceramic coil mount is used). Since the cooling fluid does not have to be inside the coil with this arrangement, the coil may be narrower and  $H_1$ , consequently, more homogeneous



each of the above temperature ranges (except 300-620 K where the error is not large).

The temperature error after calibration is less than 1.0 K for all ranges (except 300-620 K: the error does not exceed a few K).

### 5. Sources of error: Field inhomogeneities, instabilities, and sensitivity

There are a number of less than ideal characteristics of this spectrometer (as with all measurement tools) which must be discussed to successfully interpret many of the experimental results.

#### a. Inhomogeneity of the rf field, $H_1$      The probe coils produce $H_1$

fields whose intensities vary in space, somewhat. This defect can be quantified by the following experimental technique. The magnetization is sampled with two separate sequences of pulses:  $[180, \tau_1, MS_1]$  and  $[180, \tau_2, MS_2]$  where  $\tau_1 \ll T_1$  but  $\tau_1 > T_2$  and  $\tau_2 > 5 T_1$ . When  $T_2 \ll T_1$  (definitely our case) and the  $H_1$  field is homogeneous  $MS_1 = -MS_2$ . Therefore a measure of the inhomogeneity would be

$$\frac{MS_2 - MS_1}{MS_2} \equiv \frac{M_o - MS_1}{M_o} \quad (65)$$

For the wide coil probes (those that must accommodate a dewar inside of the coil) this value was at most 10%. For the narrow coil, Fig. 6, Eq. 65 yields .8%. These measurements were made with a standard sample ( $LaH_{2.99}$ ) that had a spatial extent as least as large as the largest a-Si(H) sample measured. This type of error sometimes becomes important when considering the possible nonexponentiality of magnetization recovery in a  $T_1$  determination.



b. Inhomogeneity and instability of the Zeeman field      The magnet used for this work has appreciable inhomogeneity; this must be quantified to treat correctly the narrower features of lineshapes in our samples. Before any type of lineshape measurements were undertaken, the probe was moved around in the magnet gap and the length of the FID was monitored. (This was actually done with a slightly off-resonance Hahn spin-echo sequence (156), to increase visual sensitivity to the field homogeneity changes.) When the FID length had reached a maximum, the probe was fixed in this most homogeneous location. (Zeeman field inhomogeneities cause dephasing of the transverse magnetization, just as the "A" term of Eq. 53; the apparent  $T_2$  in the presence of  $H_1$  field inhomogeneities is called  $T_2^*$ .)

The spatial inhomogeneity and the temporal instability of the Zeeman field have been estimated for this magnet and field stabilizer arrangement. This was done by accumulating an interferogram for several water samples of greater spatial extent than any of the a-Si(H) samples studied. The signal averaging went on for several hours in each case. This was repeated several times. The Fourier transformed interferograms had a FWHM linewidth of .66 kHz (or .16 Gauss) on average. Since the actual linewidth of water is very small, this width represents the combination of spatial and temporal fluctuations of the Zeeman field over the sample; most of the fluctuation is simply field inhomogeneity.

c. Spectrometer stability      Most of the NMR measurements made on these samples, because of long  $T_1$ 's and the small number of resonant spins being detected, were carried out over many hours. The stability of the entire system then becomes important when trying to estimate errors in

measurement. One way of measuring the stability is to perform an equilibrium magnetization sampling experiment repeatedly and store the results in consecutive channels of the Nicolet signal averager; the fluctuations of the values stored in the Nicolet will then be a fair representation of the system instability. This was done over a period of many hours. The short term instability was approximately .8% and the long term was approximately 1.1%.

d. Spectrometer sensitivity      The minimum number of spins that can be detected by the spectrometer is the definition of its sensitivity. The major limiting factor to the sensitivity is noise. Two significant improvements that limit the amount of noise received were: the installation of an Elgar model 2.4-.001 R line isolation transformer between the instrument rack which contains the receiver and the 120 V AC power line, and installation of a low-pass two-way filter between the Biomation and the AC power line. The former effectively isolated the receiver from every other source of noise on the line while the primary function of the latter was to isolate the Biomation from the noise generated by the LSI-11 minicomputer (which was considerable).

After this was done the minimum number of proton spins that could be detected without signal averaging was  $\sim 1.0 \times 10^{20}$ ; with signal averaging this becomes  $(1.0 \times 10^{20})/256 = 4.0 \times 10^{17}$  (this is in the limit of infinite averaging).

## D. Continuous Wave EPR Experimental Methods

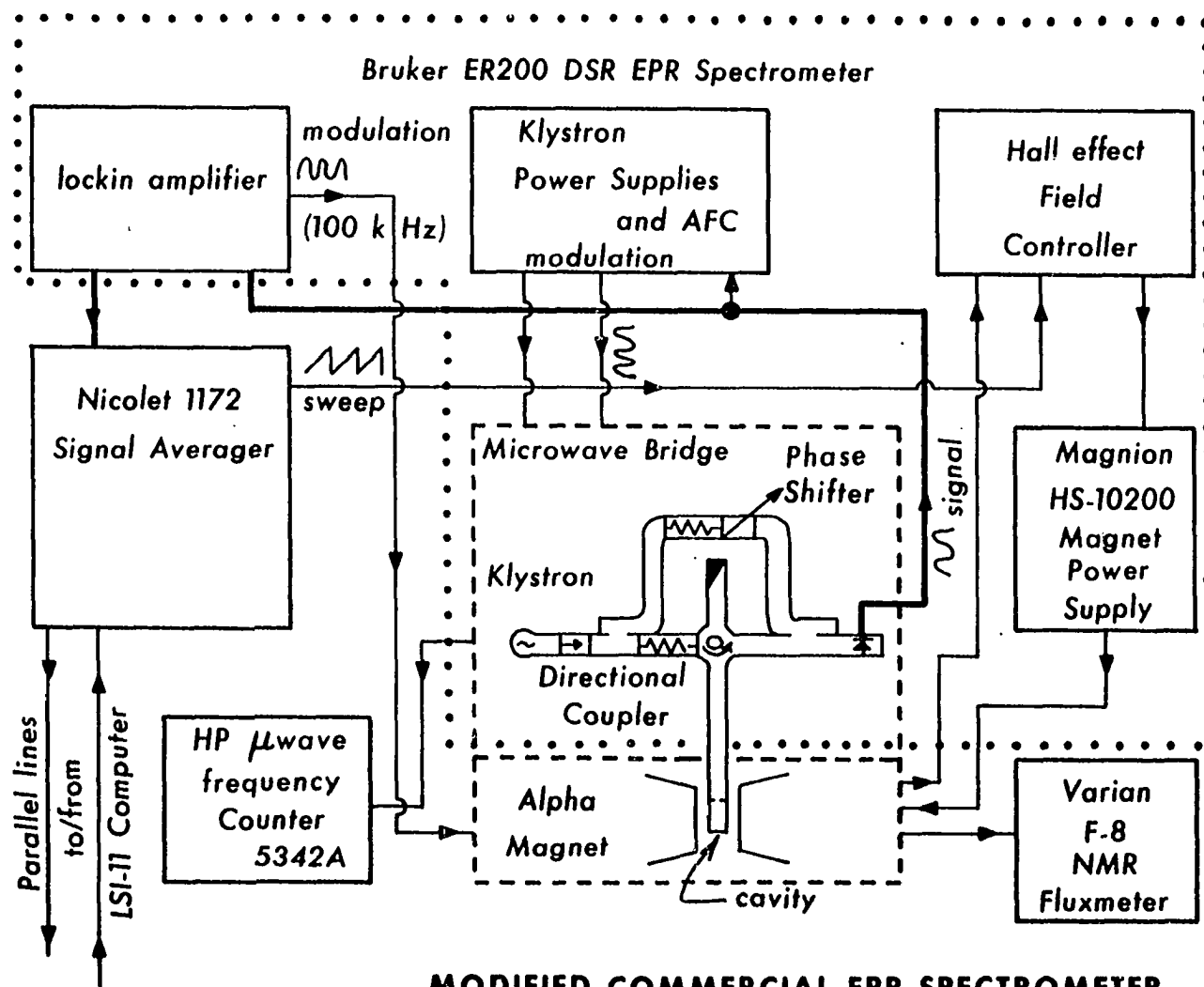
### 1. The ASP experiment

Once again it will be convenient to describe the spectrometer's operation by walking through a basic experiment; for the case of the EPR spectrometer, this is the ASP experiment. It will be helpful to refer to Fig. 7.

The cavity, with the sample in place, is critically coupled to the microwave energy travelling through the waveguides from the Klystron. This is accomplished by varying the iris opening until the reflected microwave power is minimized (the impedances of the waveguide and cavity are then matched). The reflected power is sensed by the detector diode which responds to microwave radiation. This diode operates most efficiently, in terms of detecting changes in reflected power, when it is constantly absorbing some microwave energy—thereby producing a DC current. This bias current comes about as the result of absorbing microwave radiation from the standing waves which are the superposition of travelling waves from the reference arm and those reflected from the cavity (the circulator prevents energy directly from the Klystron coupling to the diode).

Now the Zeeman field is allowed to approach resonance from very far away. As the tail of the resonance is approached the sample begins to absorb microwave energy (provided it isn't already saturated). This is manifested as a change in the sample  $Q$  and therefore the total  $Q$  (see III.B.3).

Fig. 7. Here is a block diagram of the EPR spectrometer used for this work. The commercial system has been slightly modified to facilitate wide field scans. Note that the EPR signal path is represented by a heavy line. See text for brief principles of operation



When the total (sample plus cavity)  $Q$  changes the impedance mismatch between waveguide and cavity is altered producing an increase in reflected microwave power (there is also a change in the resonant frequency of the cavity; however, the AFC circuit, Fig. 7, which operates using the lockin principle, discussed below, compensates for this frequency variation). The reflected power increases the intensity of the standing wave at the diode and thus the current through the diode.

This change in current is the electronic representation of the EPR resonance. Unfortunately, in most cases, because of noise from the Klystron and other sources this change in current would go unrecognized. Lockin detection must be used.

Imagine that the Zeeman field is set somewhere on the resonance. If the field is modulated a small amount around that position the current at the detector will be modulated proportional to the slope of the resonance absorption lineshape at that point. This modulated current from the diode is then fed into the lockin detector along with the original oscillator signal that produced the Zeeman field oscillation (with the proper phase). The lockin detector, p. 452 ref. 166, uses the original modulation signal to switch a DC amplifier whose input is the raw signal between positive and negative gain. The output then resembles a signal which has been "selectively" rectified. This rectified signal is then filtered to attain a pure DC level which is proportional to both the modulation amplitude and slope of the lineshape. Therefore, the lockin detector detects only those signals with frequencies in a narrow band around the frequency of the modulation signal and with the same phase. This, of course, greatly

increases the signal-to-noise ratio of the detection process.

So as the Zeeman field is slowly swept from one side of the resonance to the other the field is being rapidly modulated. Since the modulated diode current is proportional to the slope of the lineshape at any point the detected lockin signal must retain this same proportionality, and the signal from the lockin as a function of the slowly varied Zeeman field will then be proportional to the derivative of the actual absorption lineshape (provided that the modulation amplitude is at most  $\sim 10\%$  of the width of any "feature" of the lineshape).

The Zeeman field sweep originates with a voltage ramp function ( $-5$  V to  $+5$  V) from the Nicolet signal averager (a modification undertaken to facilitate very wide field sweeps). This is fed to the Hall effect field controller where it is amplified and offset depending upon the settings of the field width and center point controls on the front panel. This amplified and offset ramp is fed to the magnet power supply which then provides a ramp for the field strength. The actual values of the field are monitored by the Hall effect probe. The voltage values from the Hall probe are compared to those stored on a memory chip in the field effect control unit, and the differences are used to generate an error voltage which is then applied to the magnet power supply to correct the Zeeman field magnitude.

To complete the circle, the Nicolet receives analog DC signals from the lockin detector which are a function of the applied Zeeman field. At the beginning of the Nicolet ramp function the lockin output is sampled and put through an analog to digital converter (precision is 12 bits).

This digital value is stored in the first channel. After a time determined by the Nicolet clock settings, the voltage is ramped up to the next value; the Zeeman field is correspondingly increased and a new analog DC signal is received from the lockin, digitized, and stored in the second channel. The process continues until 1024 channels are stored. Finally, the resulting signals, stored in the Nicolet, form the derivative of the line-shape as a function of channel number (Zeeman field strength). The field may be swept repeatedly and these signals averaged channel by channel (the same signal to noise improvement as with the "Alvin" averaging process obtains).

These averaged signals may then be transferred to the LSI-11 computer of the NMR spectrometer where they are then stored on floppy disk for later manipulation. For the present study the digitally stored spectra were in a form that allowed convenient subtraction of background and least squares baseline adjustment. These manipulations were carried out using the FA1 program (175). Background subtraction was accomplished by acquiring the many times averaged spectrum of the cavity, without sample, under conditions identical to those used for the actual sample spectrum. The background spectrum was then subtracted channel by channel from the sample spectrum after normalizing for any differences in effective gain. Occasionally, the background signal would be linear or parabolic to good approximation with no features. In these cases it was more expedient to use the least squares baseline adjustment feature of the FA1 program to correct the recorded sample spectrum for spurious baseline drifts. Briefly, this is done by fitting regions of the spectrum that are far



from the actual sample signal to a polynomial (degree of 2 at most) and subtracting the resulting fit. This results in a very clean correction; no additional noise is added to the result as may be the case with the simple background subtraction method.

## 2. EPR spin counting

In the course of providing a characterization of these a-Si(H) samples, it became necessary to have a reasonable estimate for the concentration of paramagnetic (or unpaired) electronic spins. This is, in principle, easy to do.

It is obvious that the number of spins in a particular sample is directly proportional to the area beneath the absorption lineshape for that sample. The most accurate method of determining the proportionality constant is to compare the integrated absorption of the sample to the integrated absorption of some known amount of standard. The relative gains of the spectra,  $g$  values, spin, modulation amplitude, operating power etc. must also be taken into account in this comparison. This has been done in accordance with Eq. 14, D-33 of ref. 166.

There is one more subtle condition of the spectrometer's operation that must be taken into account when comparing the spectra of standard and sample to determine the absolute number of spins. That is the so called filling factor. Since the  $H_1$  field is provided by the standing waves in the cavity, there will be a spatial dependence to  $H_1$ . The absorption of microwave energy at a particular spatial region of the sample depends on the value of  $H_1$  at that region. This effect may be corrected for by

ensuring that the sample and standard fill the same region of space. We have accomplished this by carefully mixing known amounts of DPPH with KCl and weighing a volume of the mixture that closely approximates the volumes of the samples studied. This mixture of KCl and DPPH has a known number of spins and then serves as a reliable spin count standard. The KCl and DPPH standard was also calibrated against another DPPH standard and a  $\text{CuSO}_4$  standard.

The estimated error in the EPR spin counts due to uncertainty in the number of spins in the standard and variations in the filling factor is ~50%.

In practice we have counted spins not by comparing the integrated absorption lineshapes, but by comparing the product of the peak-to-peak (pp) derivative signal intensities and square of the pp linewidths. This method is rigorously correct when the lineshapes are identical. However, variations in lineshape may force our simple method of spin counting into appreciable error (~350% when one lineshape is Lorentzian and the other Gaussian see p. 551 ref. 166).

### 3. EPR spin-lattice relaxation time estimations

Poole (166) thoroughly discusses the procedures for determining the electron  $T_1$  from cw ASP experiments; his treatise should be consulted for details. We only briefly outline the method.

The electronic spin system will only absorb a finite amount of energy, unless the energy may be diverted from the spin system quickly enough (through spin-lattice relaxation processes). When relaxation is

fast enough all of the microwave energy incident upon the sample is absorbed; when in this regime the EPR signal is proportional to the square root of the incident microwave power due to the "linear response" of the detector diode (p. 433, ref. 166). If  $T_1$  is not short enough the microwave power incident on the sample will not all be absorbed. In this "saturation" regime, the signal intensity does not increase as fast as the square root of the power and begins to decrease at sufficiently high powers. There is also an associated "saturation broadening" of the resonance line.

We have monitored these details of EPR signals as a function of applied microwave power and from this estimated  $T_1$  in some cases. In the Bruker ER 220 D SR used for this work the power meter is "calibrated" from information stored in a memory chip. To check on the accuracy of this calibration, we monitored the EPR signal intensity for solid DPPH and found that the intensity did follow the power level raised to some fractional power (exponent). This fractional index was measured to be within 3% of  $1/2$ , until the sample began to saturate at approximately 100 mW of incident microwave power. The absolute magnitude of the indicated power is not easily calibrated; the manufacturer suggests that the absolute error in the power reading is no more than 10%. At any rate, the magnitude of  $H_1$  at the sample, which is proportional to the square root of the power, is the relevant quantity. This proportionality constant was determined by performing a saturation study on DPPH (whose  $T_1$  is known), see p. 711 of Poole (166).

#### 4. Temperature variation and control

EPR lineshape measurements were made over a limited temperature range. Two schemes were employed for the two temperature ranges covered.

a. 77 K A standard Bruker liquid N<sub>2</sub> quartz finger dewar was employed for this temperature. The "finger" portion of the dewar protrudes into the cavity, greatly increasing Q ( $\sim 29\%$ ) and shifting the resonant frequency (down  $\sim 5\%$ ). The change in Q becomes important if intensity measurements are to be made.

Operation of the spectrometer at high power was impossible in this configuration. The boiling liquid N in the finger dewar was, of course, within the cavity; the bubbling caused violent changes in the cavity Q which the AFC circuit could not track and compensate for at incident microwave powers above  $\sim 200$   $\mu$ W. A carborundum boiling chip placed in the bottom of the finger dewar away from the sample did allow operation at slightly higher powers. Further improvements were made by adjusting the AFC circuit. However, operation above  $\sim 10$  mW was still not possible.

b. 120 K to 300 K Temperature variation in this region was accomplished in a fashion completely analogous with that used for the NMR experiments of similar temperature range except that the actual hardware used was the commercial Bruker B-VT-1000 temperature control system. None of the problems of high power operation associated with the liquid N finger dewar arrangement were present in this regime. The dewar insert used with the B-VT-1000 unit created approximately the same Q increase and frequency shift as the finger dewar. Temperature accuracy was  $\pm 1$  K.

### 5. Sources of error: Microwave frequency instability, errors in Zeeman field strength and field inhomogeneity

The Hewlett-Packard model 5243A microwave frequency counter has an absolute error of  $\sim 1$  ppm (including possible aging of the internal crystal time base). The observed frequency stability of the klystron was only  $\sim 50$  ppm when operating with the liquid N finger dewar (because of the bubbling problems mentioned above) and  $\sim 5$  ppm under normal conditions. Therefore, the maximum frequency measurement error was 50 ppm operating at 77 K and 6 ppm operating under normal conditions.

The indicated values of the Zeeman field were calibrated in two ways. The value of the Zeeman field at center sweep is given on the front panel of the Hall effect field control unit. However, due to errors in transducer placement and internal offsets the readout is in error. This center field error was discovered and corrected by running a standard sample of DPPH ( $g = 2.0036 \pm .0003$ ) several times. The center field readout is approximately  $340 \pm 150$  ppm larger than the field measured using DPPH. The indicated values of the Zeeman field sweep width were calibrated with the NMR fluxmeter shown in Fig. 7. Expressed as a fraction of the indicated sweep width the error is  $\sim 2\%$ . Therefore, for a sweep width of 100 G around  $g = 2$  the total error in measured Zeeman field at any point would be approximately 240 ppm (this assumes that the error due to the center field readout has been corrected). When  $g \sim 2$  then the accuracy of  $g$  is approximately  $\pm .0005$ ; it should be realized that most of this error is due to uncertainty in the Zeeman field.

For very low (a few hundred Gauss) Zeeman fields, the error can be quite large. For instance, when the field control unit indicates 0 G the actual field (by measurement with a Rawson rotating wire loop gaussmeter) is  $\sim 100$  G. Slightly above 100 G, the field value measured with the Rawson gaussmeter is the indicated field within the relatively high experimental error of the Rawson,  $\sim 2\%$ .

A crude estimate of the Zeeman field inhomogeneity was obtained by moving the probe of the NMR gaussmeter around the magnet gap. The probe was moved over rather large regions (several cm) while the values of the field were noted. This large region inhomogeneity was then extrapolated down to regions of the order of a sample volume. The result is roughly .08 G inhomogeneity over a typical sample volume.

Since the number of spins is proportional to the square of the derivative linewidth, the sensitivity of the spectrometer is line width dependent. For a linewidth of 5 G operating at 1% of full levelled power (1.96 mW) the sensitivity for  $s = 1/2$ ,  $g \approx 2$  spins is approximately  $2.6 \times 10^{14}$  spins (provided there is no saturation). With signal averaging, but otherwise the same operating conditions, the minimum number of detectable spins is  $2.6 \times 10^{14} / 2^{12} = 6.3 \times 10^{10}$  in the limit of infinite averaging.

The next chapter will deal with the experimental NMR and EPR results on reactively sputtered amorphous silicon hydrogen alloys. Chapters I-III will be applied in discussion of these results.

#### IV. RESULTS AND DISCUSSION

The results to be presented in this chapter represent the first (to this author's knowledge) study of its type on reactively sputtered a-Si(H) alloys: extensive NMR measurements have been made and correlated with EPR measurements on a series of a-Si(H) samples in which the H concentration has been systematically varied. Because it is the first such study, the philosophy embraced has favored a mind's eye "big picture," sometimes at the expense of refinement in measurement detail. In other words, the course plotted has served to map out that terrain which is accessible by conventional magnetic resonance techniques in the study of amorphous silicon-hydrogen alloys; which is not to say that no conclusions will be reached, rather that these conclusions, while extremely plausible, must be viewed as preliminary and subject to later refinement (or perhaps revision in some cases).

##### A. NMR Results

###### 1. FFT absorption lineshapes

We begin with results of an NMR lineshape study. As previously mentioned, the lineshapes to be presented were arrived at by fast Fourier transforming (FFT) the time domain free induction decay (FID) signal. The lineshape function,  $f(\omega - \omega_0)$ , as discussed in Chapter II, is an even but otherwise arbitrary distribution function. Fortunately, the lineshapes actually observed are usually well approximated by either Gaussian or Lorentzian shapes and sometimes shapes that are "between" Gaussian and

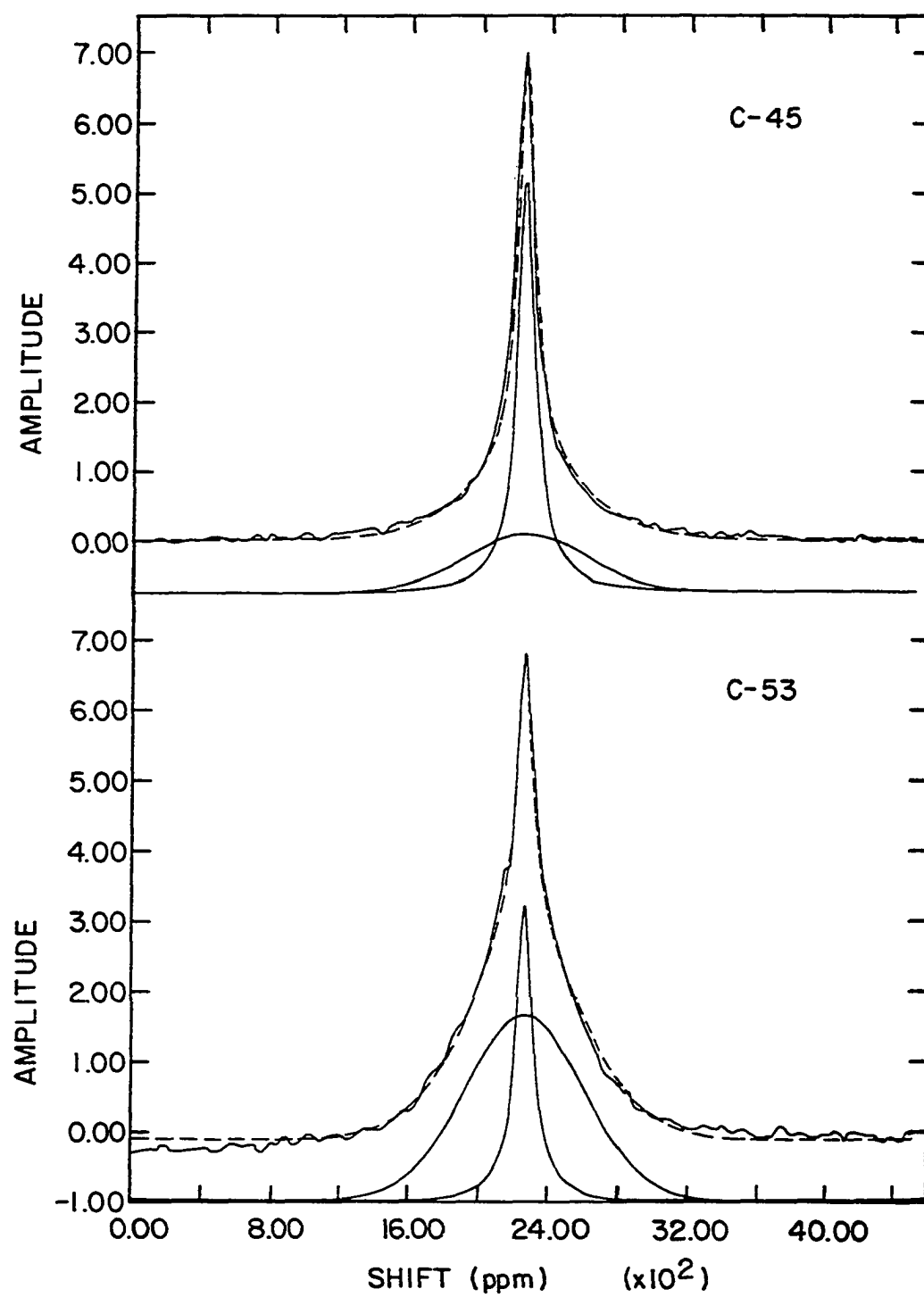
Lorentzian (163); this seems to be particularly true when the absorption line is homogeneously broadened (this means that all spins giving rise to the line experience the same spin temperature--they are communicating efficiently). The most obvious characteristic of the FFT spectra for this study is that the shape is not simply a Gaussian or Lorentzian. Figure 8 demonstrates that for both the lowest (4%) and highest (17%) H concentrations the lineshape may be resolved into the superposition of a broad Gaussian and a narrow Lorentzian lineshape function. This seems to be a universal feature of proton NMR spectra in this material, see Reimer (78). In fact, this wide Gaussian--narrow Lorentzian superposition consistently fits the data for the entire H concentration series.

One must be concerned about the physical interpretation of this two component decomposition of the lineshapes: Do the individual components actually correspond to separate proton environments or is the lineshape as a whole actually homogeneous with the details of the shape being a function of H concentration? Before we answer this, consider the possible causes of absorption lineshape broadening in our case.

There are three processes that could be the source of the linewidth in this material: inhomogeneous chemical shift broadening (this would usually be quite small compared to our observed linewidths--however, the amorphous nature of the material requires that we not dismiss it a priori as a possibility here), heterospin electron-proton dipolar interactions (heterospin silicon-hydrogen dipolar interactions will be negligible due to the scant abundance, 4.7%, of  $^{29}\text{Si}$  and its small magnetogyric ratio), and homonuclear proton dipolar broadening (definitely the most likely).



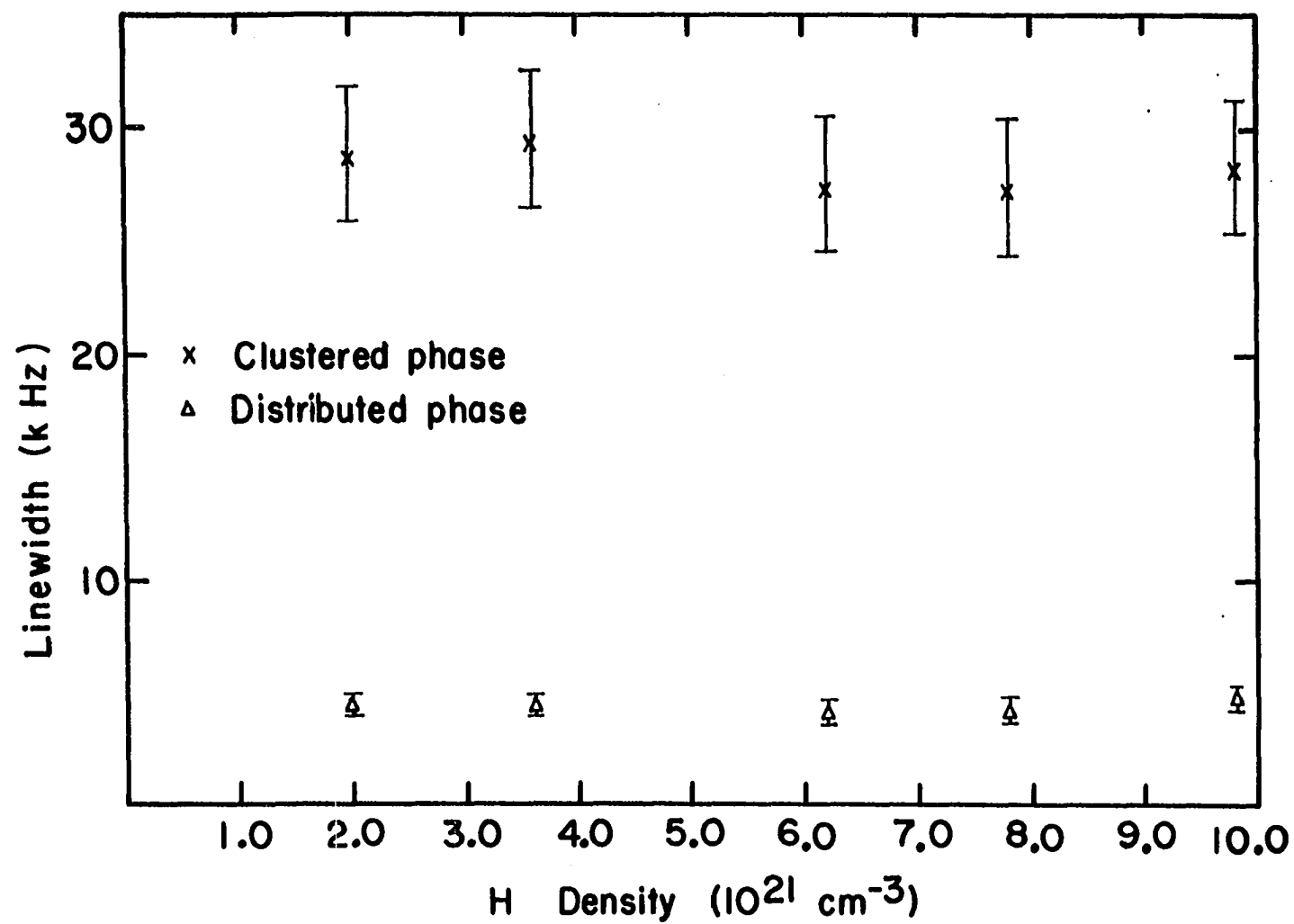
Fig. 8. The lowest H concentration ( $\sim 4\%$ ), upper spectrum, and the highest H concentration ( $\sim 17\%$ ), lower spectrum a-Si(H) samples show remarkably different proton NMR FFT absorption lineshapes (solid line). Both are decomposed into the superposition (dashed line) of narrow Lorentzian and wide Gaussian lineshape functions (lower solid lines)



The work of Reimer (68) established early that the width of the line shapes in GD material is almost totally due to the homonuclear dipolar interactions (this was done by applying the FFT after an 8-pulse homonuclear decoupling cycle). The later work of Carlos and Taylor (69) along with more due to Reimer (78) has established conclusively by solid echo and hole burning experiments that the two components are distinct: the total spectra are inhomogeneous sums of the individual dipolar broadened components. It should be understood what this really means: the mutual spin flip mechanism of the  $B$  term in Eq. 53 has been found to be much more efficient for the broad component of the spectra (compared to the narrow). Therefore, the Gaussian spins communicate more closely among themselves, compared to the communication among the Lorentzian spins and the communication between the Gaussian spins and the Lorentzian spins; this is enough to qualify for the inhomogeneous categorization. These experiments were done on GD material; the lineshapes and widths of the two components in this study are identical with the GD results, therefore it seems very unlikely that the results would have been any different for the case of RS material.

a. A tale of three phases Interestingly, as we see in Fig. 9, the linewidths of the two components remain convincingly constant through the whole of the H concentration series. The relative intensities of the two components, however, do change dramatically with the H concentration, as exemplified by the two extremes in Fig. 8. This phenomenon of constant linewidths as a function of total H concentration (the reason for use of the qualifier "total" will soon be apparent) is surprising. A brief study

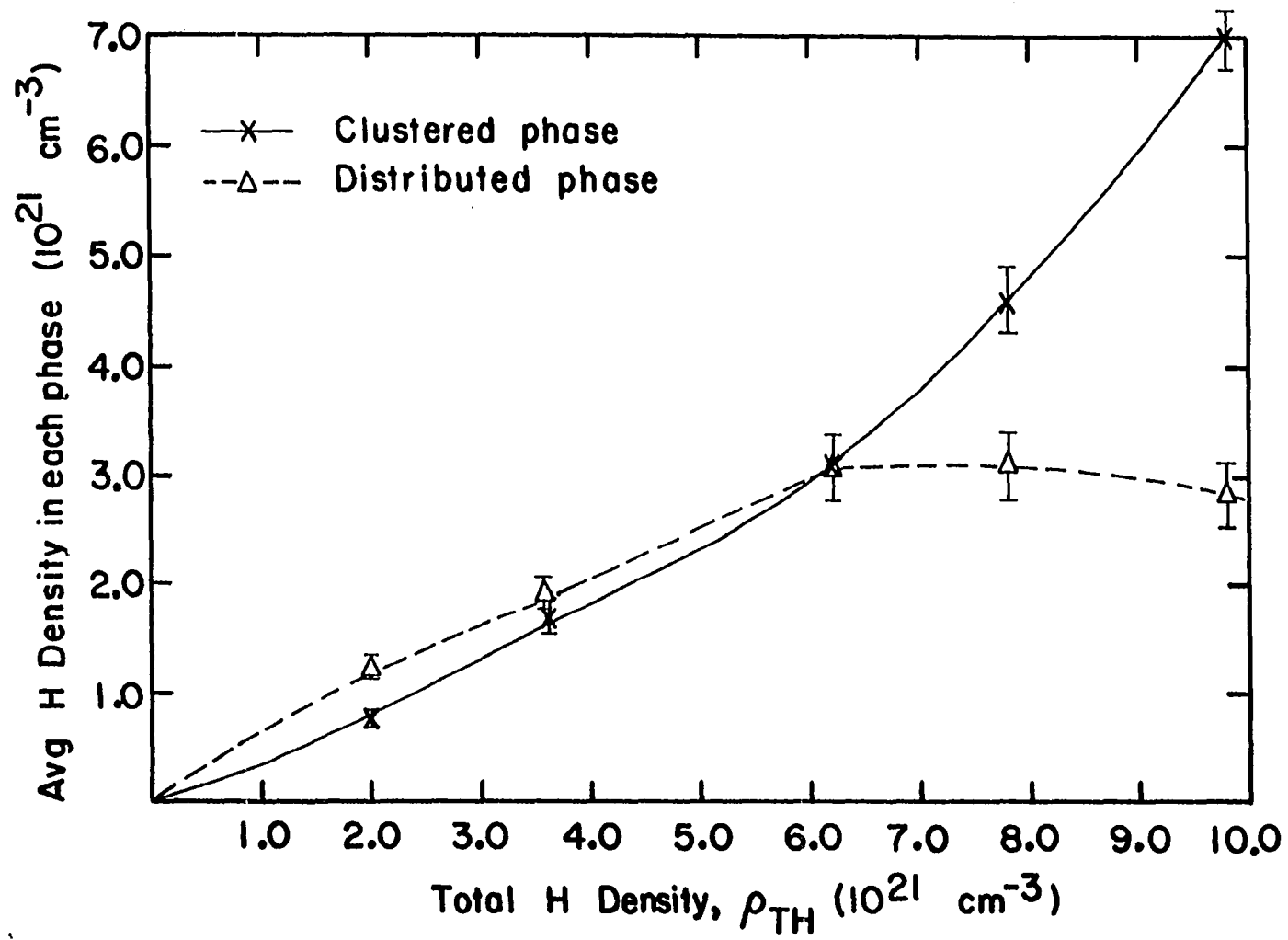
Fig. 9. The FWHM linewidths of the Gaussian component ( $\sigma$ ) and the Lorentzian component ( $\Delta$ ) are plotted as a function of total H concentration. The designations "clustered" and "distributed" anticipate arguments to come in the text



of the van Vleck equation for the second moment, Eq. 55, will reveal that as H nuclei are brought closer together the linewidth of the spectrum (as measured by the second moment) should increase. We observe that addition of H does not increase the linewidth. An obvious resolution of this apparent paradox would be to postulate that as the total concentration of H increases, the H nuclei do not become more crowded together; the local density of H remains constant with an increase in total H concentration. Put another way, the film growth mechanism must favor an a-Si(H) network in which the film is deposited in distinct phases, such that the local density of H assumes particular values. This is a radically new result and will no doubt have great impact upon the way in which the film growth process is understood. These ideas will now be placed upon a firmer foundation; this will be accomplished by developing the means of calculating the average local density of the protons that give rise to a particular absorption line component.

The area beneath each component lineshape will be proportional to the number of spins associated with that component. It has just been established (Fig. 8) that the relative intensities of each component of the FFT lineshape vary with the total H concentration. Figure 10 summarizes the trend of this variation, thereby depicting the percentage of spins associated with either the "Gaussian phase" or "Lorentzian phase" of the material as a function of total H concentration. From this, it is seen that the number of spins in each phase initially grows at approximately the same rate. After a total H concentration of ~11% is reached, the rate of growth of the Gaussian phase appears to increase at the

Fig. 10. The average H density (number of protons divided by total sample volume) from each component (Gaussian, "x," or Lorentzian, "Δ") plotted as a function of total H content (expressed as number of H atoms divided by total sample volume),  $\rho_{TH}$





expense of a corresponding leveling off or decrease in the growth of the Lorentzian phase. What sorts of structural configurations are represented by these two components of the lineshape?

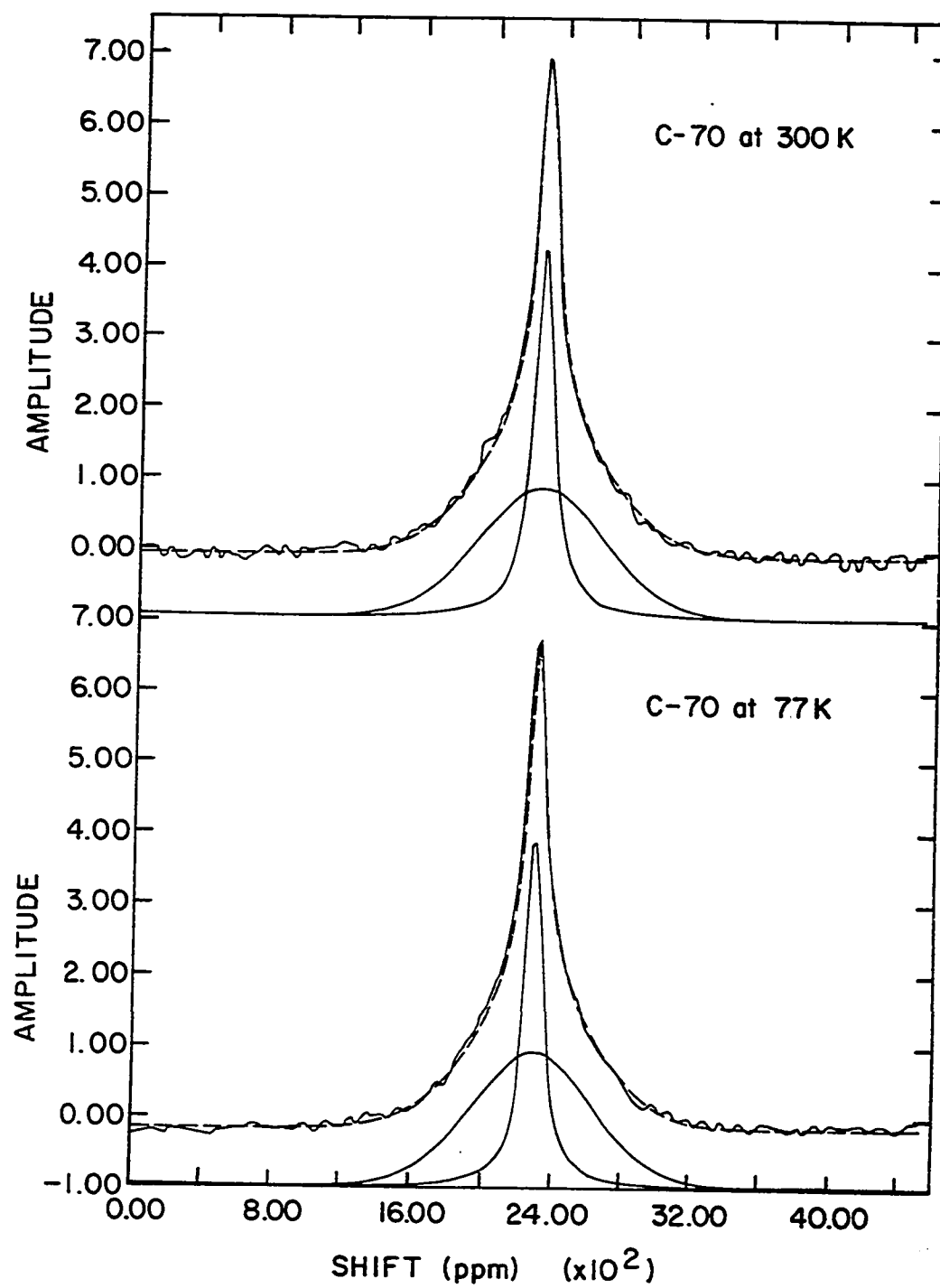
In the crystalline solid state in the absence of motion or exchange the observed lineshapes are often Gaussian or nearly so. The presence of a Lorentzian component in a magnetic resonance lineshape usually suggests one of two possibilities: motional or exchange narrowing of the resonance lineshape (156,159,163). Exchange narrowing comes about when the wavefunctions of the spinning particles overlap sufficiently so that the mutual fields of the dipolar interaction (Eq. 53) are averaged away; while, for the case of motional narrowing the averaging away of the dipolar interaction comes about as a result of actual motion of the spins. It should be emphasized here that Eq. 55 is valid only in the so called rigid lattice regime where neither motion nor exchange are appreciable; the second moment expression may lose its validity because the calculation assumes the dipolar interaction to be static and to originate from point dipoles. Furthermore, the second moment of a Lorentzian lineshape is undefined (the integral in Eq. 56 diverges). Exchange narrowing is common in electronic spin ensembles; it is virtually unheard of in a nuclear ensemble. We then eliminate exchange narrowing as the cause of the Lorentzian lineshape. (One should, however, make a mental note that the system at hand is indeed rather strange--prudence dictates that exchange narrowing not be "completely eliminated.") Motional narrowing is very common in NMR; it must be taken seriously as a possible cause of the Lorentzian lineshape.

It is usually possible to decrease the rate of motion of a spin ensemble, and thusly the line narrowing, by decreasing the temperature. If the spins' motion is slowed enough, the rigid lattice regime is attained and the line will broaden dramatically. Figure 11 compares the spectra of the 14% H sample taken at room temperature and liquid N<sub>2</sub> temperature. No broadening with reduced temperature is observed. For most systems with moving nuclear spins, 77 K would be cold enough to freeze out the motion; one could probably safely conclude on this basis alone that motional narrowing is not present. To strengthen the argument, measurements were made at liquid He temperatures; again, no discernable broadening of the narrow line was observed. All of this leads to the conclusion that motional narrowing may be eliminated as the source of the Lorentzian component.

Another, traditionally less common, situation in which a Lorentzian lineshape may be observed is the case of a "dilute" ensemble of spins with random interparticle spacings. Abragam (163) calculates the line-width in a full-width-at-half-maximum (FWHM) sense in two somewhat complementary ways.

He initially considers the case of spins placed randomly upon a periodic lattice. The average local density of spins may then be represented by a fractional occupancy of the available lattice sites. By making use of relationships between the second and fourth moments for a lineshape function that has been truncated far in the wings and the van Vleck formulas for these moments, Abragam obtained this relationship between the FWHM and the local average density of spins:

Fig. 11. The proton NMR FFT absorption spectra are compared for the 14% H  $\alpha$ -Si(H) sample at room temperature (upper traces) and liquid N<sub>2</sub> temperature (lower traces). In each case the spectra are decomposed in the same fashion as in Fig. 8. It is apparent that no broadening of the narrow Lorentzian component occurs on lowering the temperature from room to liquid N<sub>2</sub>. Measurements were carried all the way to liquid He temperature with no broadening of the Lorentzian



$$\Delta\omega_{\frac{1}{2}}(\text{rad/s}) = 10.84 \gamma^2 \hbar \rho_L (\text{cgs units})^{\frac{1}{2}} \quad (66)$$

where  $\Delta\omega_{\frac{1}{2}}$  is the FWHM of the lineshape in radians/sec and  $\rho_L$  is the local average density of spins in  $\text{cm}^{-3}$  (Abragam's arguments for this case are scattered about over pp. 126, 107, and 112 of ref. 163). This formula applies to any situation in which the ratio of the square root of the fourth moment of the line shape to the second moment is very much larger than one; of the two normally adopted lineshape functions, Lorentzian and Gaussian, only the Lorentzian satisfies this criterion. The Lorentzian shape has much of its intensity far in the wings of the distribution; these wings correspond to absorption by spins that are very close together. It is then physically reasonable to impose a cutoff in the distribution corresponding to some sensible notion of the closest possible approach of two spins.

Abragam (p. 126) outlines another method of relating the width of the lineshape to the local density of spins in a random spatial distribution. In this second so called statistical approach to the problem only the A term of the dipolar Hamiltonian, Eq. 53, is used in the calculation: this is justified somewhat cryptically by a presumed great dilution of the spin system. This approach yields directly the conclusion that the lineshape is exactly Lorentzian and the relation

$$\Delta\omega_{\frac{1}{2}}(\text{rad/s}) = 7.60 \gamma^2 \hbar \rho_L (\text{cgs units}) \quad (67)$$

---

<sup>1</sup>This is not precisely Abragam's result. Upon making the same approximations and following his method, the present author finds this equation where the numerical prefactor differs slightly and insignificantly from the result quoted by Abragam.

between the linewidth and the average local density of the spins. Notice that the prefactor in Eq. 67 is smaller than that of Eq. 66; this is probably due to dropping the  $B$  term of the dipolar Hamiltonian in the derivation of Eq. 67.

Both of these approaches require the assumption that the spin system is dilute: for the second case no numerical criterion is given, however, in the first case the derivation rests upon the assumption that the occupied site fraction,  $f$ , is less than one percent. We will find upon application of either one of Eqs. 66 or 67 that this is not quite satisfied for our case. However, as noted earlier, the first treatment assumed a random dilute occupation of a lattice, and the calculation proceeded within that framework. We are dealing with an amorphous material: here the quantitative disorder of the network allows much more variation in the interspin spacing than in the crystalline lattice occupation scheme. In effect then, we may view the "lattice" simply as a calculational construct and allow the lattice parameter to become small (there will be some limit to how small the lattice parameter is allowed to become). In this case, of course, the number of possible occupation sites becomes large and we find that  $f$  will decrease for a given spatial density of spins. It is concluded that the effects of quantitative network disorder allow us to apply Eq. 66 to our case.

It should be noted that more recent work (176), involving more detailed calculations, has shown that a lineshape very similar to a Lorentzian with slightly more intensity in the wings obtains for systems of dilute randomly distributed spins (the crystalline lattice occupation

scheme is used here also--and again the present author makes the case that we may allow the lattice parameter to become effectively small, making the result phenomenologically valid for our case).

Finally, for the purpose of calculating the local density of the Lorentzian phase, a compromise between Eqs. 66 and 67 has been made by simply averaging the prefactors:

$$\Delta\omega_{\frac{1}{2}}(\text{rad/S}) = 9.22 \gamma^2 \rho_L (\text{cgs units}). \quad (68)$$

We have so far not dealt with the structural configuration of the protons that contribute to the Gaussian component of the line. If we imagine allowing a collection of randomly distributed spins to become spatially closer together to form some sort of cluster, we expect that the lineshape due to absorption by such spins will no longer be Lorentzian but will become more closely Gaussian: this will happen because a greater number of the spins will now be strongly interacting, taking intensity away from the center of the line and forcing it towards the wings, thereby broadening the "shoulders" of the distribution which results in an approximate Gaussian shape.

We now turn to the relatively easy task of calculating the local density of protons that contribute to the Gaussian component of the absorption line. Appealing to the van Vleck formula for the second moment, Eq. 55, we may easily evaluate it by making the following approximation. We consider that the distance to the  $n^{\text{th}}$  nearest neighbor,  $R_n$ , may be approximated on the average by

$$\frac{4}{3} \pi R_n^3 \rho_G = n + 1 , \quad (69)$$

where  $\rho_G$  is the local density of protons. Then Eq. 55 becomes

$$M_2 = \frac{4}{5} \gamma^4 \hbar^2 \pi^2 \rho_G^2 \sum_n \frac{1}{(n+1)^2} . \quad (69)$$

We may then use the relation between the second moment and the FWHM line-width for a Gaussian:

$$2.35[M_2]^{1/2} = \Delta\omega_{1/2} , \quad (70)$$

Finally obtaining

$$\Delta\omega_{1/2} (\text{rad/s}) = 5.30 \gamma^2 \hbar \rho_G (\text{cgs units}) , \quad (71)$$

which relates the FWHM of the lineshape to the local density for a cluster. One may question the averaging arguments leading to Eq. 71. To verify that they are not unreasonable one may follow Abragam and calculate the second moment for a fully occupied simple cubic lattice of protons with lattice parameter  $d$ :

$$M_2 = 5.1 \gamma^4 \hbar^2 I(I+1)/d^6 \Rightarrow \Delta\omega_{1/2} = 4.60 \gamma^2 \hbar \rho_G \quad (72)$$

where the obvious identification  $\rho_G^2 = d^{-6}$  has been made. The author believes that the larger prefactor in Eq. 71, compared to that of Eq. 72, is consistent with a cluster in which some disorder is allowed. This is so because in the amorphous cluster configuration one expects that occasionally two protons would be allowed to come closer together than



the average thereby making a contribution further in the wings of the distribution (which would of course increase  $M_2$ ). One should also note that this may change the lineshape which would then modify Eq. 70; however, the difference between Eqs. 71 and 72 is insignificant. We are free to choose Eq. 72 for our case.

Before we apply the local density formulas, Eqs. 68 and 71, two inadequacies in the raw data must be addressed.

We will, first, concern ourselves with the "real" value of the FWHM linewidth of the two phases. For either lineshape, we take an average of the computer optimized linewidths, which appear in Fig. 9, over all of the samples. This is 4.40 kHz and 28.2 kHz for the Lorentzian and Gaussian components, respectively. Now, we recall the spatial and temporal inhomogeneity of the magnet discussed in section III.C.5.b; this was  $\sim 6.66$  kHz. We may approximately correct the above linewidths by simply subtracting the inhomogeneity from each: Yielding 3.74 kHz and 27.54 kHz for the Lorentzian and Gaussian FWHM linewidths, respectively.

We may now calculate the local proton densities for each phase. We find  $\rho_L = 3.39 \times 10^{21} \text{ cm}^{-3}$  (average proton spacing,  $a_L$ , is  $6.66 \text{ \AA}$ ) and  $\rho_G = 4.34 \times 10^{22} \text{ cm}^{-3}$  ( $a_G = 2.85 \text{ \AA}$ ) for the Lorentzian and Gaussian local densities, respectively. One additional source of error must be dealt with before volume occupancies for each phase are calculated.

In section III.C.1 the necessary trigger delays due to the dead time of the NMR receiver were discussed. These trigger delays cause some of the information in the FID (and therefore the FFT) to be lost. There are principally two errors involved: an error in the overall proton spin

density due to directly comparing the magnetization sampling of water to that of our samples, and an error in the relative proportion of Gaussian and Lorentzian components, because the FID for the Gaussian decays faster than the FID for the more narrow Lorentzian. The corrections were very simple and will be only briefly discussed.

For the corrections in the percentage of each component in the line-shape, one may extrapolate the magnetization back to the zero of time from the first instant after the trigger delay, using the computer optimized linewidths to determine the individual time constants; this will yield the correct equilibrium magnetization for each component and therefore one easily corrects the ratio of each component for a given spectrum.

Next, armed with the corrected percentages of each component one may extrapolate back to zero time from the median of the magnetization sampling window (see section III.C.2) to calculate the proper equilibrium magnetization for a given sample; this same extrapolation is then made for the water standard, and the corrected ratio of the equilibrium magnetizations will yield a more accurate estimate of the number of spins in a given sample.

These corrections have been applied to the raw data—results appear in Table 2.

Also appearing in Table 2 is the fractional (percentage) volume of each sample occupied by each phase of the material (Lorentzian or Gaussian). These are calculated by applying Eqs. 68 and 71, the total H concentration for each sample, and assuming the same mass density for each sample (95% of crystalline silicon density was used:  $2.214 \text{ g/cm}^3$ ).

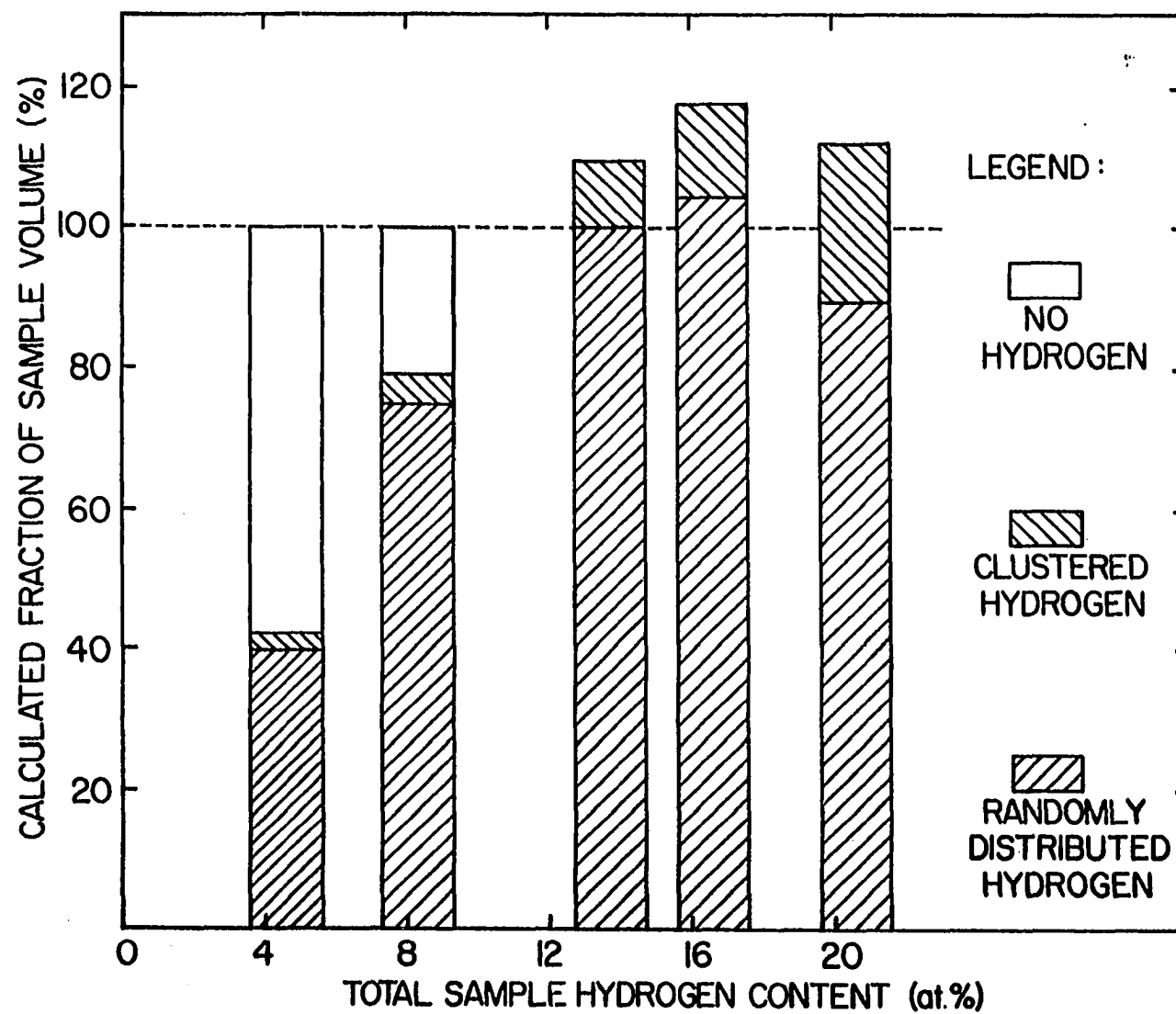
Table 2. Corrections to spin counts and lineshape analysis due to the receiver deadtime

Sample label	Lorentzian fraction (%)		Gaussian fraction (%)		Total $^1\text{H}$ spin density ( $\text{cm}^{-3}$ )		Corrected Total H concentration (at. %)	Corrected Lorentzian volume fraction (%)	Corrected Gaussian volume fraction (%)
	raw	corrected	raw	corrected	raw	corrected			
C45	61.6		38.4		$2.76 \times 10^{20}$		4.6	39.7	2.17
	58.8		41.2		$3.28 \times 10^{20}$				
C52	61.7		38.3		$7.76 \times 10^{20}$		8.3	75.0	4.07
	59.0		41.0		$9.23 \times 10^{20}$				
C51	47.9		52.1		$1.38 \times 10^{21}$		13.7	100	9.51
	45.1		54.9		$1.70 \times 10^{21}$				
C70	40.1		59.9		$2.31 \times 10^{21}$		16.7	104	13.6
	37.4		62.6		$2.90 \times 10^{21}$				
C53	26.8		73.2		$2.01 \times 10^{21}$		20.8	89.4	21.4
	24.6		75.4		$2.61 \times 10^{21}$				

Figure 12 graphically summarizes the volume occupancy of both the Lorentzian and Gaussian phases of the material as a function of total H concentration (actually the data has been graphed with the corrected values of the total H concentrations in accordance with Table 2). It can be seen that for the 4% and 7% H samples there are indeed regions of the sample in which there is no H. Then at approximately 12% H the entire volume of the sample is evidently hydrogenated with one of the two phases; from that point to higher total H concentrations the volume of sample occupied by the Gaussian phase begins to increase at the expense of the Lorentzian phase occupancy. We see from Fig. 12 that we overestimate the total volume of the sample for those of relatively high total H content; the maximum in this overestimation occurs with the maximum of Lorentzian phase occupancy—most probably indicating that the prefactor in Eq. 68 is too small. Actually, in view of the many approximations made, it is very impressive indeed that the total volume is overestimated by less than 20%.

The assumption that the mass density is 95% that of pure crystalline Si for each sample needs some justification. If the mass density of the a-Si(H) samples increases with decreasing total H concentration, it is possible that the validity of our conclusion that three phases exist in the material may be called into question. Mass density measurements have been made for RS a-Ge(H) by the Harvard group (11) as a function of total H incorporation. They find that the density changes only slightly, and the trend is density increasing with decreasing H concentration. For the above three-phase conclusion to be invalidated, the mass density must be increased by more than a factor of two from 12% to 4% H concentration;

Fig. 12. The sample volume occupancies for each of the "three phases of a-Si(H)": The randomly distributed H phase, a-Si:H; the H cluster phase, HC; and the pure a-Si phase, no H. These volume occupancies appear as a function of total H content (as at. %); the total H content of each sample has been corrected for the "receiver dead-time" error (see text)



this would place the mass density at approximately twice the crystalline value for the low H concentration samples. Impossible. Nonetheless, mass density measurements were made on all of the samples in the series (which effectively destroyed them for the purposes of making other measurements of any integrity); unfortunately, the measurements were very inconclusive due to extremely poor reproducibility of results.

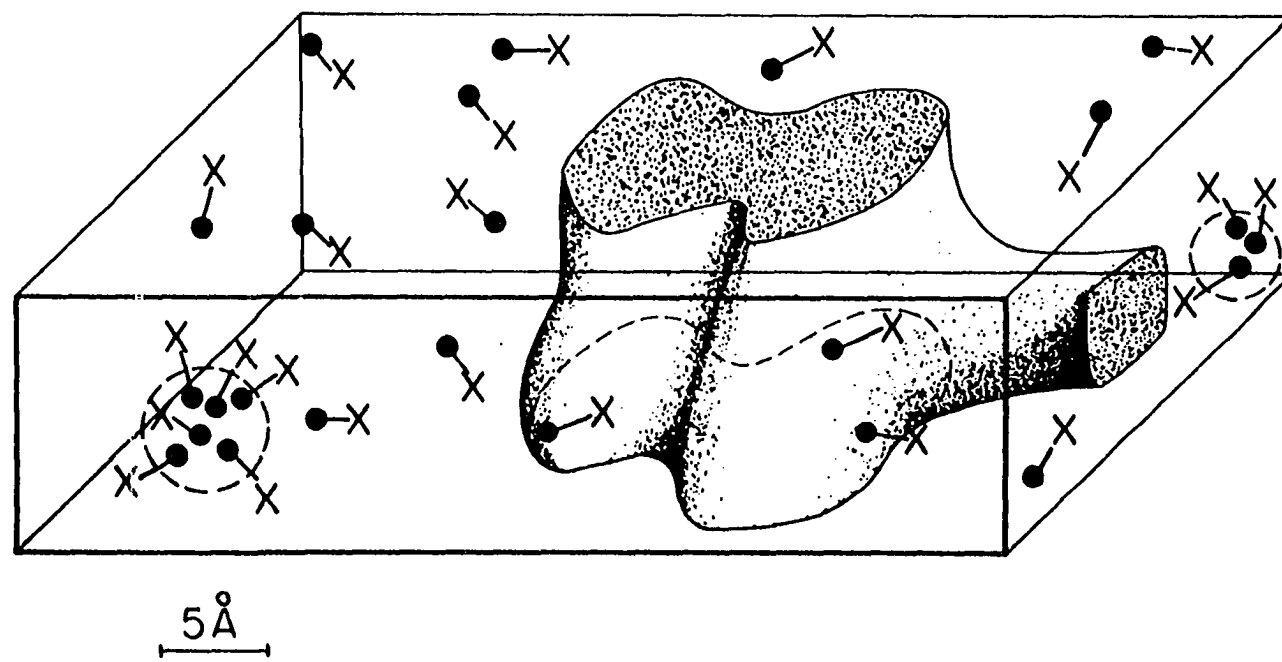
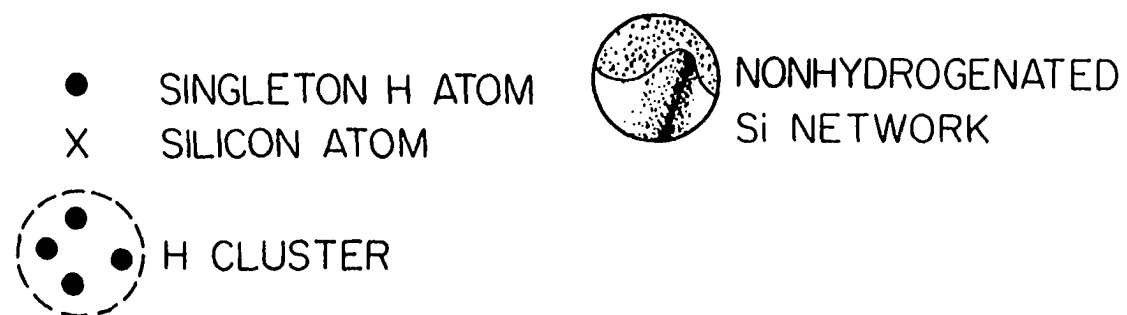
Thus we find evidence for two and three fold intermediate range disorder (or inhomogeneity) in the low and high total H concentration samples, respectively: the high concentration ( $> \sim 12\%$  H) samples appear to be composed of a phase of a-Si(H) in which the H atoms are more or less uniformly yet randomly distributed on the amorphous network occasionally decorated with relatively compact clusters of H (probably lining the surfaces of some microvoid structure, the size of which is still unknown). As the total H concentration is reduced we find this two phase structure is interrupted by yet a third phase which incorporates no H at all. A schematic of this model appears in Fig. 13. Hereafter we shall find it convenient to refer to the densely clustered H giving rise to the Gaussian component simply as HC (hydrogen clusters) and to the phase of the material in which the H are randomly distributed throughout the a-Si network (which is manifested in the Lorentzian NMR line) as a-Si:H. The latter designation for that phase of the material in which the H is randomly distributed, a-Si:H, recognizes that this phase is probably a distinct random alloy whereas the HC "phase" is just a defect in that alloy network.

b. The two component NMR line and the interpretation of ir data

As briefly discussed in the introduction, the interpretation of some of the

Fig. 13. A schematic of the "three phases" of a-Si(H). The average local densities of H in the HC, a-Si:H, and a-Si "phases" are, respectively,  $4.34 \times 10^{22} \text{ }^1\text{H/cm}^3$  (average separation = 2.85 Å),  $3.39 \times 10^{21} \text{ }^1\text{H/cm}^3$  (average separation = 6.66 Å), and  $0 \text{ }^1\text{H/cm}^3$ . The actual sizes of the spatial regions filled by each phase are unknown

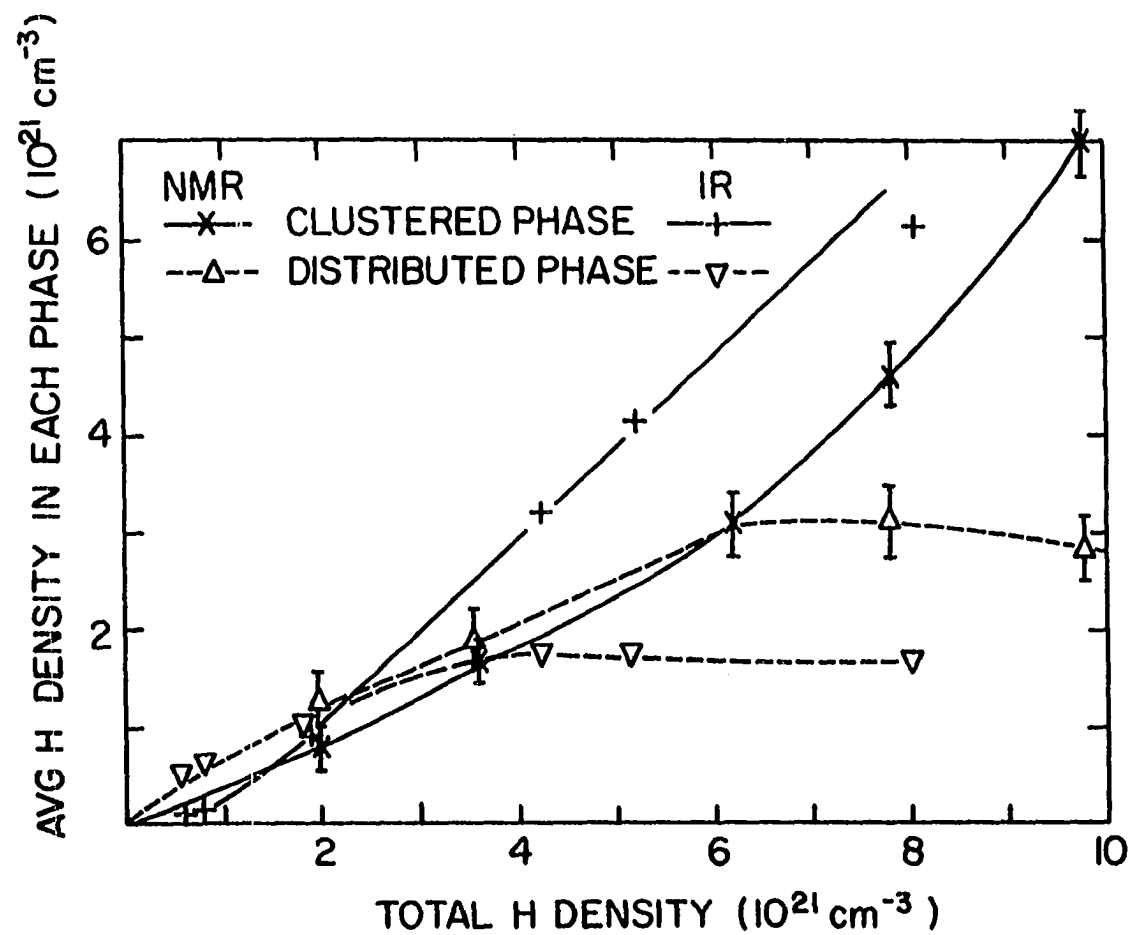




ir absorption lines is still the subject of controversy. In particular, Paul of the Harvard group has been fairly vocal (109) in his objection to the conventional assignment of the  $2100\text{ cm}^{-1}$  ir absorption line exclusively to the stretching mode of multihydride bonded H (109). He argued that there were other equally plausible explanations, two of which involved closely spaced H atoms bonded to different Si atoms. This combination, it was said, would give the required  $2100\text{ cm}^{-1}$  stretch mode without the wagging ( $640\text{ cm}^{-1}$ ) and bending ( $840\text{--}890\text{ cm}^{-1}$ ) modes of the multihydride bonds; this was needed to explain some data in which the  $2100\text{ cm}^{-1}$  peak exists without the corresponding wagging and bending peaks. Shanks et al. (79) have correlated the NMR data of Fig. 10 with the integrated ir absorption for the anomalous  $2100\text{ cm}^{-1}$  peak and the  $2000\text{ cm}^{-1}$  peak (which is generally accepted as arising from absorption in the stretch mode of an isolated Si-H bond) as a function of total H concentration; this appears in Fig. 14. A very plausible correlation is established between the NMR HC phase concentration and the  $2100\text{ cm}^{-1}$  ir peak integrated intensity on one hand, and the NMR a-Si:H phase concentration with the  $2000\text{ cm}^{-1}$  ir peak integrated intensity on the other hand. Furthermore, an older study by Connel and Pawlik of the Harvard group (11) presents the analogous ir data for the a-Ge(H) case as a function of RS H pressure (which scales with total incorporated H concentration). The resemblance of the data to Fig. 10 of this work is very striking.

Thus, the NMR lineshape data has contributed to the resolution of a long standing debate in the interpretation of ir absorption data on a-Si(H).

Fig. 14. This is essentially Fig. 10 of the present work augmented by infrared absorption (ir) work of Shanks et al. (79). The "+" and "v" represent normalized integrated intensities of the  $2100\text{ cm}^{-1}$  and  $2000\text{ cm}^{-1}$  ir peaks, respectively. The curves are aids to the eye. This and other discussion (see text) resolves a long standing dispute in the interpretation of ir data in a-Si(H). Taken from Shanks et al. (79)



## 2. Proton NMR spin-lattice relaxation times

The last section has demonstrated that the details of the spin-spin interactions between protons in a-Si(H) may be an aid to understanding the material's structure. This section will demonstrate that even more of the structural mysteries of this material may be unraveled by study of the spin-lattice interaction.

a. General trends To begin,  $T_1$  was measured at room temperature as a function of total H concentration for the series of samples; these data are presented in Fig. 15. Notice that the maximum occurs at the same H concentration at which we had previously found the nonhydrogenated regions to be disappearing (recall Fig. 12). This rather interesting behavior led to an investigation of the spin-lattice relaxation as a function of temperature for each of the samples in the H concentration series.

The temperature dependence of  $T_1$  often yields clues to the origin of the relaxation mechanism; we will find this to be the case here. Figure 16 capsulizes the temperature and total H concentration dependence of  $T_1$ . It will be noticed that as H concentration passes from low to high the temperature dependence of the relaxation time changes drastically. Furthermore, the average level of  $T_1$  passes through a maximum at about 11% H: this is not surprising in view of Fig. 15.

b. A confused relaxation Before we proceed with the analysis of this temperature dependence, we must somewhat qualify what is meant by  $T_1$ . If the Bloch equations (Eq. 49) hold and the pulse sequence discussed in Chapter III is used then the magnetization will follow Eq. 63 as previously discussed. However, the relaxation may proceed via some mechanism that

Fig. 15. Room temperature spin-lattice relaxation time ( $T_1$ ) is plotted as a function of the average H concentration in a-Si(H). See text for significance of  $T_1$  maximum

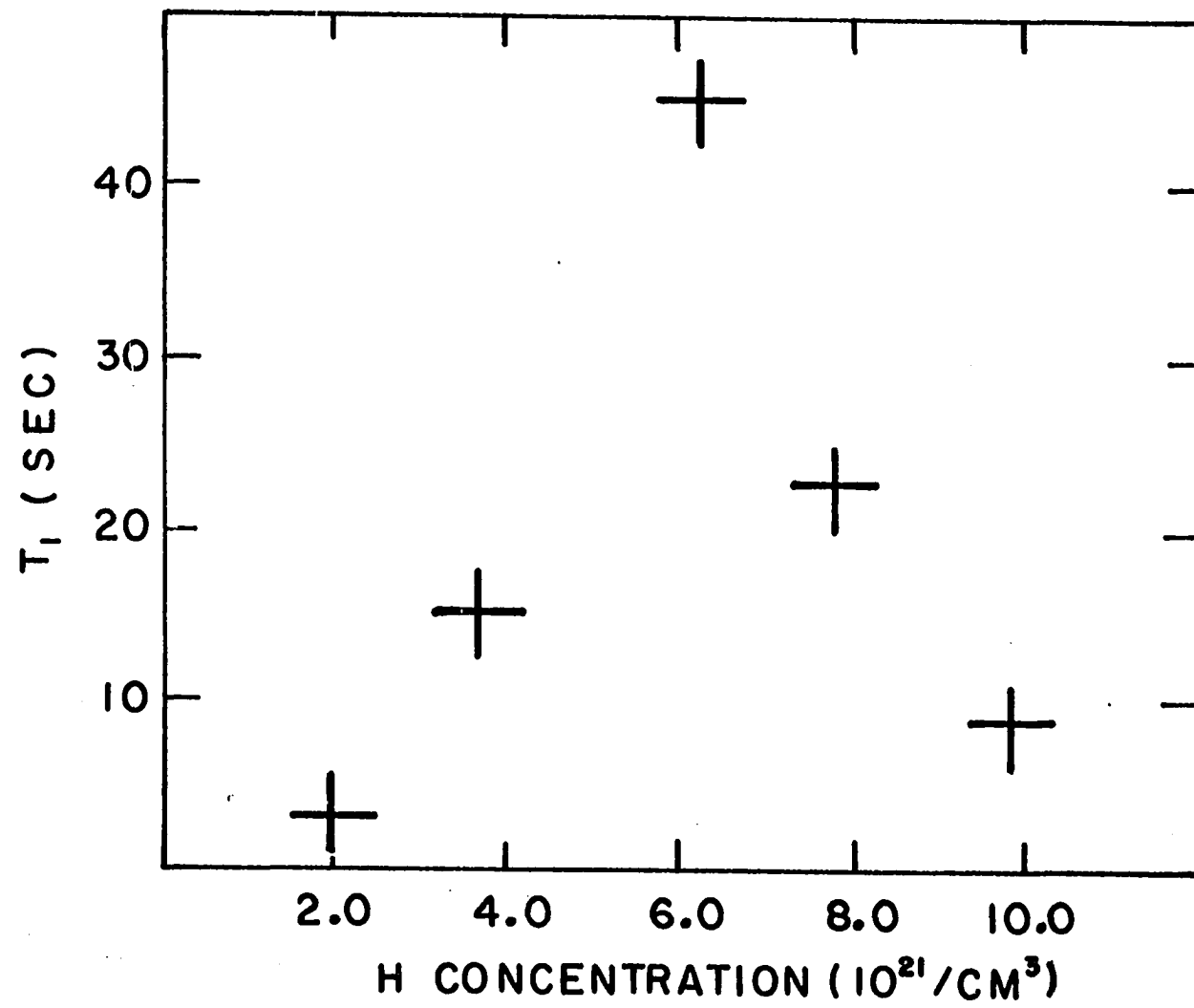
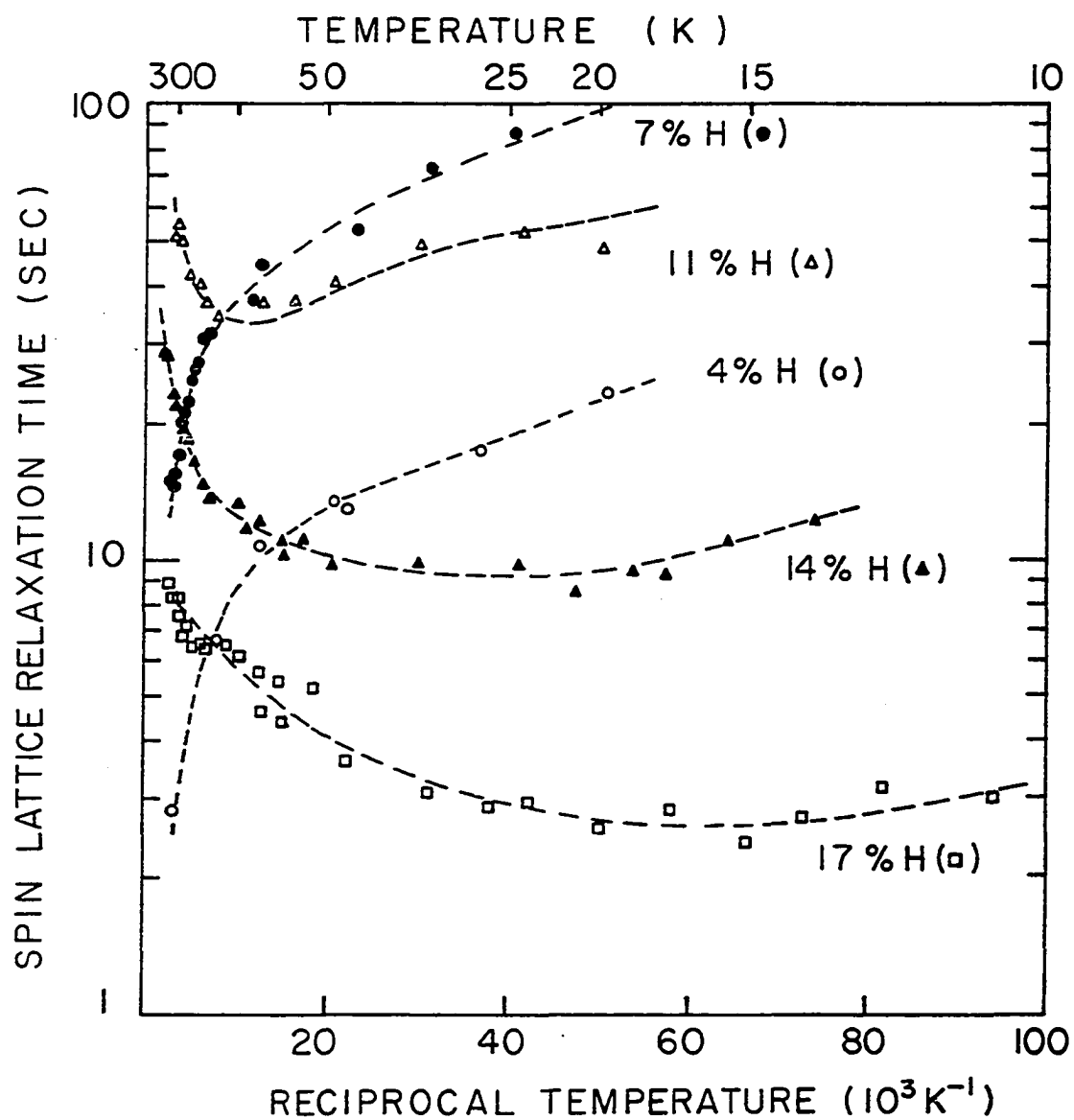


Fig. 16. A compilation of the temperature and total H concentration dependence of the spin-lattice relaxation time,  $T_1$ , is presented. The broken lines are visual aids, not fits; they also point towards the measured  $T_1$  values at 4 K (these will appear in later figures). Notice the dramatic change in temperature dependence between 7 and 11% H concentration





does not obey the Bloch equations or the inhomogeneity of the sample may lead to some sort of a distribution of  $T_1$ 's. The latter seems more likely for our case: it is well known that spin-lattice relaxation in insulators and semi-conductors usually proceeds through the process of spin diffusion; this is not a physical motion of the spinning particle, rather it is a long sequence of mutual spin flips. This is the means by which the spin system attains its temperature through the  $\beta$  interaction of the dipolar Hamiltonian Eq. 53, (as briefly discussed in Chapter II). Blumberg (177) has shown that in many such cases a small portion of the early recovery does not obey the Bloch equation.

Bloembergen (178) was the first to discuss the phenomenon of spin diffusion. He calculated the probability rate of nearest neighbors experiencing a mutual spin flip

$$W \approx \frac{1}{50T_2} \quad (73)$$

where  $T_2$  is the spin-spin relaxation time of the spins involved in the diffusion (this number is very approximate--Movaghar and Schweitzer (115) carry out the calculation for the disordered lattice). One may then define the spin diffusion coefficient

$$D = Wa^2 \quad (74)$$

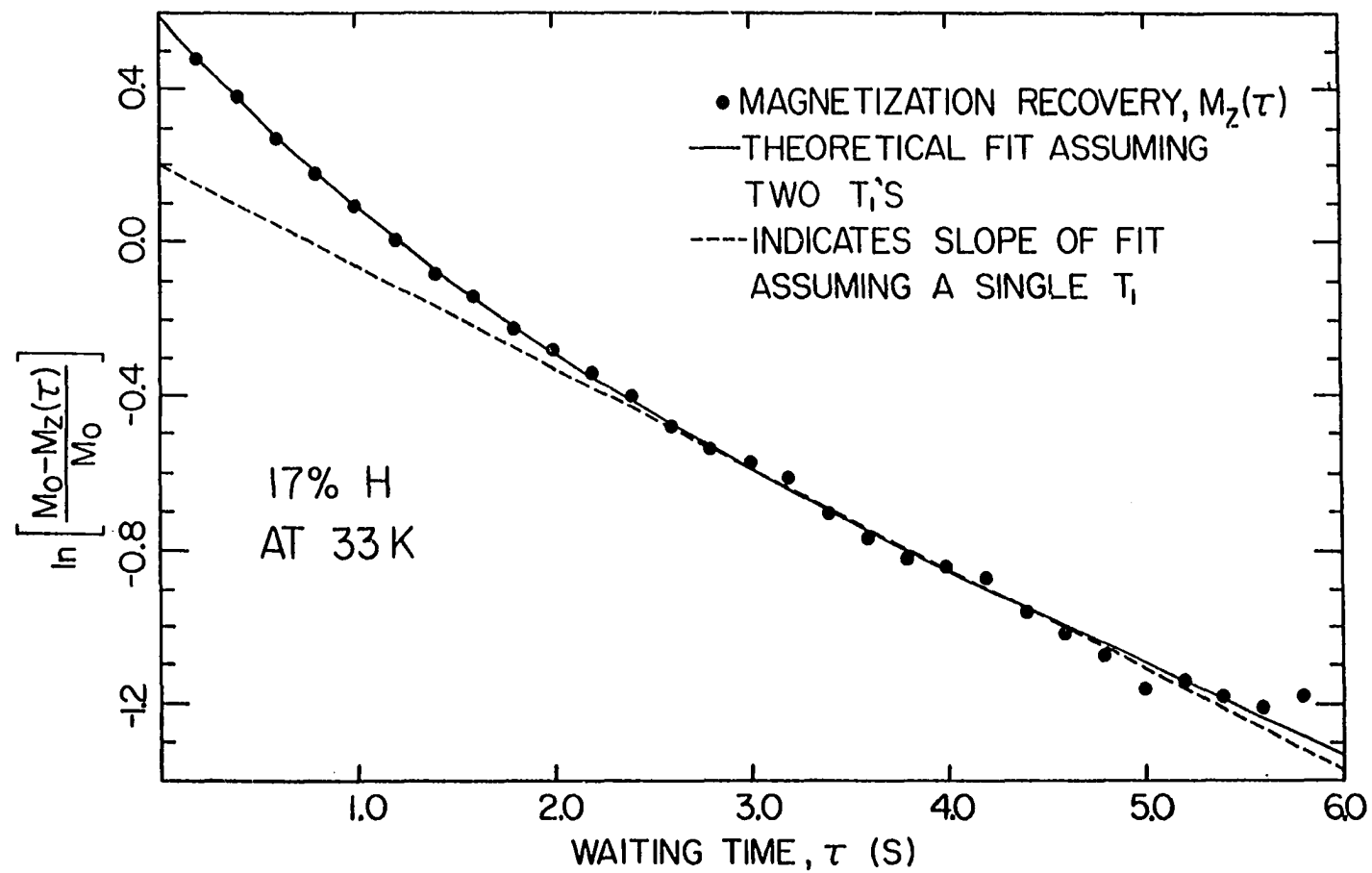
where  $a$  is the interspin spacing. Thus it is seen that all of the information necessary for calculating the diffusion coefficient is contained in the lineshape. Throughout the calculations, to follow, the diffusion coefficient employed is that for the a-Si:H phase of the material, i.e.

the information from the Lorentzian component of the lineshape is used. This is done because in every case the a-Si:H phase of the material covers by far the greatest volume; furthermore, diffusion through this phase will be slower--this should be the rate determining step, and thus determine  $T_1$  unless the clusters have their own relaxation "sinks" (definitely a possibility). When Eq. 74 is applied for this case, assuming  $a = 6.66 \text{ \AA}$  (the average separation of protons in the Lorentzian phase), one obtains  $D = 1.04 \times 10^{-12} \text{ cm}^2/\text{s}$ .

The ultimate "sinks" for this diffusing spin energy are called relaxation centers. These centers, as the above implies, are rare compared to the resonant spin species. For the case of amorphous materials, it is not difficult to imagine that there could exist inhomogeneity in both the spatial distribution and strength of these relaxation centers; therefore, at any particular time after an excitation not all of the spins will experience the same spin temperature--those interacting with more or stronger centers will assume the temperature of the center(s) more quickly. Thus, the so called nonexponential magnetization recovery of Fig. 17 will not be too surprising (notice that this nonexponential recovery is an effect probably beyond that predicted by Blumberg (177), mentioned earlier).

This nonexponential recovery, observed in the highest H concentration sample at 33 K, exemplifies the type of recovery observed throughout the series; although, this particular example is amongst the most striking. The recovery has been fit (using FITMAN (179) with an equation of the form

Fig. 17. A reduced natural log plot of the magnetization recovery following a  $180^\circ$  inversion pulse (Section III.C.2.b), as a function of the waiting time,  $\tau$ . The solid line is a computer fit assuming the magnetization follows Eq. 75: This yields  $T_{1a} = 0.98$  S,  $T_{1b} = 4.46$  S, and  $R = M_{0a}/M_0 = 43.7\%$ . If a single exponential recovery is fit, Eq. 63,  $T_1 = 3.33$  S. See Appendix C for a complete study using the dual exponential approach



$$M_z(\tau) = M_{oa}(1-2e^{-\tau/T_{1a}}) + M_{ob}(1-2e^{-\tau/T_{1b}}) \quad (75)$$

where  $1/T_{1a}$  and  $1/T_{1b}$  are the relaxation rates for the magnetizations  $M_{oa}$  and  $M_{ob}$ , respectively; this assumes only two distinct spin reservoirs with their own connections to the lattice.

The apparent existence of only two spin-lattice relaxation times had lead to the hope that these times were in some way correlated with the two hydrogenated phases of the material (a-Si:H or HC a-Si(H)). A complete data analysis has been carried out on each of the spin-lattice relaxation measurements that were made (with the exception of some measurements in the 7% H sample made at high temperature) on the basis of Eq. 75. This appears in Appendix C; there will be found  $T_{1a}$ ,  $T_{1b}$ , and  $R = M_{oa}/M_o$  (which gives an indication of what fraction of the total number of spins has the faster relaxation mechanism, by convention  $1/T_{1a} > 1/T_{1b}$ ) plotted as a function of temperature for all of the samples, except the 4% H sample (the poor signal-to-noise of the measurements rendered those fits practically meaningless). Unfortunately, no correlation between  $R$  and the relative amount of a-Si:H or HC spins is in evidence.

In principle, one anticipates more than two distinct rates of spin-lattice relaxation: a distribution of relaxation rates to coincide with the supposed distributions in relaxation center strength and local concentration is to be expected. However, in practice, one would probably not be able to distinguish two relaxation rates from a distribution of rates unless exceptional signal-to-noise was attained. There are several possible trends in the two reservoir analysis; however, the very tentative nature of the trends relegates discussions to Appendix C.

Therefore, in arriving at the data plotted in Fig. 16 a uniform spin temperature has been assumed, i.e. Eq. 63 has been used--see Chapter III. In fact, all of the discussion to come of the spin-lattice relaxation data will only deal with the spin-lattice relaxation time in the sense of a least squares fit to the recovery data using Eq. 63. Therefore, we will be dealing with an average, in some sense, of the actually more complicated distribution of spin-lattice relaxation times. It should be noted here that none of the other workers in the field has reported any sort of nonexponential magnetization recovery (69,73,78,83); it is possible that they have simply not searched carefully enough, or it could be that the very nature of the relaxation centers in their material (mostly GD) lends itself to an homogeneity in the observed relaxation rate.

c. The case of the hopping electrons      Having made the above qualifications to what is meant by  $T_1$  in our case, we are in a position to discuss the mechanism(s) of spin-lattice relaxation in a-Si(H). We begin with the low H concentration samples. These two samples (4% H and 7% H) show an almost Arrhenius temperature behavior, i.e., the relaxation rate appears to be proportional to the Boltzmann factor  $e^{-E/kT}$ , where E is some activation energy, particularly for the high temperature regions of the plot. In fact, it is possible to fit the data quite well by assuming that the relaxation rate is the sum of two Arrhenius processes with different activation energies; the slope of the plot, Fig. 16, gives the value of the activation energy. The data in both sets are fit quite well assuming activation energies of .05 eV and .003 eV. It is, however, necessary to assume another rate which changes slowly with temperature in order to fit the liquid He point for either sample.

Jellison and Bishop (180) have observed such apparently thermally activated relaxation behavior in some of their work on chalcogenide glasses. They applied the relaxation by spin diffusion expression due to de Gennes (de Gennes' paper is in French, however, Rorschach (181) gives an authoritative discussion of the more general result with references to de Gennes' original work) with the pseudo-potential radius replaced by the spatial extent of the electronic wavefunction. This was done because those authors believed that the Fermi contact interaction between a localized paramagnetic electron and the resonant nuclei is the operative mechanism of the relaxation center; the original work by de Gennes assumed that the dipolar interaction between a paramagnetic center and surrounding resonant nuclei provided the energy flow to the center (see Bloembergen (178) and Blumberg (177)), so that the effective range of the dipolar interaction, the pseudo-potential radius (distance at which the rate of spin diffusion just equals the rate of direct relaxation to the center) is replaced by the spatial extent of the electronic wavefunction. The expression for the overall relaxation rate then becomes

$$\frac{1}{T_1} = 4\pi n_s D r_o \quad (76)$$

where  $r_o$  is the spatial extent of the paramagnetic electron's wavefunction, and  $D$  is the spin diffusion constant. The density of relaxation centers,  $n_s$ , is thought to be thermally activated: this can be understood in terms of a thermally activated bond breaking process (these could be the "negative U" centers discussed in section I.E).



The low H concentration spin-lattice relaxation data from the present study may be fit very well with expressions of the above form. However, there exists a model with fewer parameters and a substantial connection to a large body of previous work on a-Si(H):

As is well known, and as we will see upon discussion of the EPR results, the addition of H reduces the "total" concentration of dangling bonds that give rise to the  $g = 2.0055$  EPR signal. We say "total" because the three-phase conclusions from the previous section would indicate that large volumes of the two low H concentration samples are pure a-Si containing no H. Perhaps the most preeminent feature of pure a-Si is the hopping conductivity which follows the famous Mott law (148). This conductivity has been repeatedly correlated with the  $g = 2.0055$  EPR signal (53,58,155,93,96). In fact, Gourdon et al. (182) in a very recent work, have completed extensive measurements of the spin-lattice relaxation time of the dangling bond EPR resonance in evaporated a-Si. They find that above the phonon bottleneck temperature the electronic relaxation time follows

$$\frac{1}{T_{1e}} = \lambda T + v_{oe} \exp \left[ - \left( \frac{T_o}{T} \right)^{\frac{1}{2}} \right] , \quad (77)$$

where  $\lambda$  depends upon the concentration of electrons and arises from exchange effects,  $v_{oe}$  is the prefactor of that contribution to the relaxation that comes from the hopping motion of the electrons and should not exceed the maximum phonon frequency of the material (see P. Nagels in ref. 149),  $T_o$  is the Mott law temperature constant given by

$$T_o = \frac{(2.1)^4}{r_o^3 N(E_F)k} , \quad (78)$$

where  $r_o$  is the spatial extent of a hopping electron's wavefunction, and  $N(E_F)$  is the density of states at the Fermi level.

It will be the contention, in the following, that the proton relaxation in the low H concentration samples occurs via the hopping electrons whose spin-lattice relaxation obeys Eq. 77. Because the electrons are in motion, yet localized in terms of the spatial extent of their wavefunctions, the theory of nuclear spin relaxation via spin diffusion to strong relaxation centers of Movaghar and Schweitzer (115) is most likely to be the appropriate theory of relaxation; furthermore, these authors develop the theory specifically for amorphous materials. Their final expression for the relaxation rate in this regime is

$$\begin{aligned} \frac{1}{T_1} &= \frac{2\pi^{3/2}}{3} n_s C^{1/2} (e\sigma)^{1/2} = 1.46 \times 10^{-34} (T_2)^{1/2} \rho_L n_s \left[ \frac{t_c}{1 + \nu_o^2 t_c^2} \right]^{1/2} \\ &= K n_s \left[ \frac{t_c}{1 + \nu_o^2 t_c^2} \right]^{1/2} , \end{aligned} \quad (79)$$

where  $C$  is the strength of the interacting paramagnetic center (178),  $n_s$  is the average concentration of centers,  $\rho_L$  is the local concentration of protons,  $T_2$  is the spin-spin relaxation time (for both the local proton concentrations and the  $T_2$  value those of the Lorentzian phase are used, as discussed earlier),  $\nu_o$  is the Larmor frequency in Hz (as opposed to rad/sec, see Eq. 5b), and  $e\sigma$  is proportional to  $W$  of the Bloembergen

theory above, but takes into consideration that the network is disordered;  $1/e$  is a factor between 0 and 1 that correctly counts the percolation paths of the magnetic energy through the disordered lattice ( $e = 9.9$  has been assumed, following Movaghar and Schweitzer (115)). A brief study of Eq. 79 will reveal that the relaxation rate may be viewed as proportional to the geometric mean of the direct rate of relaxation of the spin energy to the center,  $Cn_s^2$ , and the rate of spin diffusion through the disordered network.

The strength of the interaction,  $C$ , is given by

$$C = C_0 \frac{t_c}{1 + \nu_0^2 t_c^2} = \frac{3}{20\pi} \gamma_N^2 \gamma_e^2 \hbar^2 \frac{t_c}{1 + \nu_0^2 t_c^2} \quad (80)$$

where  $t_c$  represents a correlation time for the time dependent fluctuations of the dipolar interaction of the paramagnetic center with the surrounding resonant nuclei. Equation 80 is a spectral density function which arises from the nonsecular terms of the dipolar Hamiltonian, Eq. 53. This particular spectral density function arises from the  $C$  and  $D$  terms of the dipolar Hamiltonian for unlike spins. These terms involve the product of the  $z$ -component of the electron's spin with  $I_+$  and  $I_-$  of the resonant nuclear spin; therefore, the fluctuations in the longitudinal component of the paramagnetic center's field are responsible for the relaxation. The other terms of the dipolar Hamiltonian may be ignored because they either pertain to spin-spin relaxation effects or require a mutual spin flip between an electron and proton (without a phonon assist this would be non-energy conserving) which is highly improbable. See pg. 295 of Abragam (163) for details.

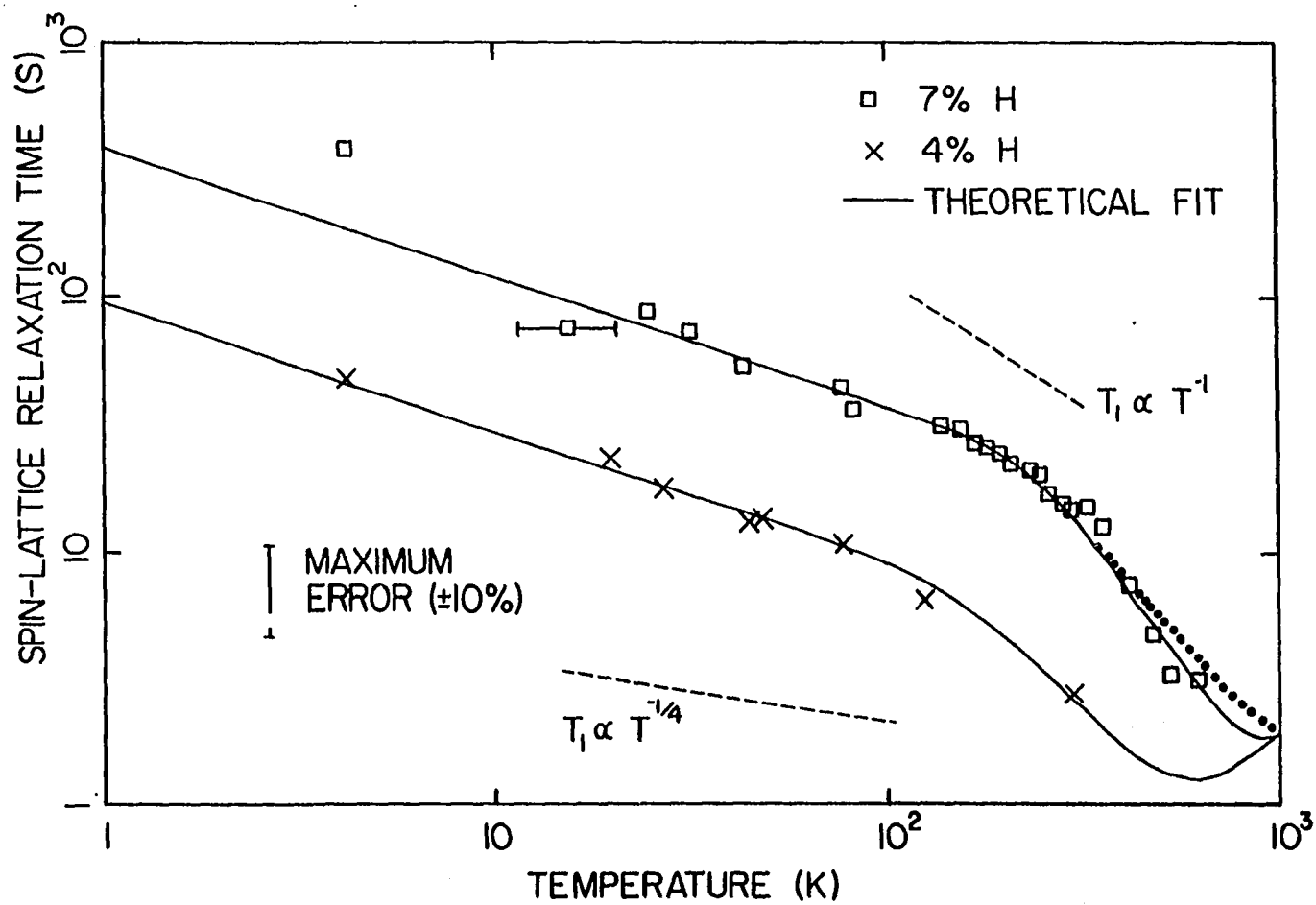
Figure 18 presents the low H concentration  $T_1$  data replotted on log-log scale together with analytic fits using Eqs. 77, 79, and 80. The fits are well within experimental error, with the exception of the 4 K point for the 7% H sample (this could be due to diffusion barrier effects discussed by Rorschach (181) that would be expected to come into play as the hopping electron motion is frozen out, or the phonon bottle neck in the electronic relaxation, discussed by Gourdon (182), could account for it); and the results for the parameters are very consistent with other measurements.

For the 4% H sample  $n_s = 1.46 \times 10^{18} \text{ cm}^{-3}$ ,  $\lambda = 3.11 \times 10^3 \text{ s}^{-1} \text{ K}^{-1}$ ,  $\nu_{oe} = 1.0 \times 10^{13} \text{ Hz}$ , and  $T_o = 1.5 \times 10^7 \text{ K}$ .

The best fit for the 7% H sample yields  $n_s = 1.01 \times 10^{18} \text{ cm}^{-3}$ ,  $\lambda = 4.0 \times 10^2 \text{ s}^{-1} \text{ K}^{-1}$ ,  $\nu_{oe} = 3.0 \times 10^{14} \text{ Hz}$ , and  $T_o = 6.0 \times 10^7 \text{ K}$ . The dotted line of Fig. 18 represents the fit with  $\nu_{oe}$  constrained to the more reasonable value of  $1.3 \times 10^{13} \text{ Hz}$ , and yields  $T_o = 3.2 \times 10^7 \text{ K}$ ; the other parameters were not allowed to vary.

Gourdon et al. (182) obtain  $T_o$  values of  $3.0 \times 10^7$  and  $5.4 \times 10^7 \text{ K}$  from their EPR relaxation measurements. They compare this to the transport measurements by Paul and Mitra (183) on sputtered a-Si (no H) and to that of Lewis (184) on evaporated a-Si (again, no H) where  $T_o = (3.5-8.8) \times 10^7 \text{ K}$  and  $(1.8-2.4) \times 10^8 \text{ K}$ , respectively; the  $T_o$  values tend to increase with increasing annealing temperature in either case. In Lewis's transport measurements (10) on a-Ge(H) values of  $T_o = (1.8-2.6) \times 10^8 \text{ K}$  are obtained, Hasegawa and Yazaki (185) obtain  $T_o = 1.8 \times 10^8 \text{ K}$  from transport measurements on sputtered a-Si, and Knotek (186) obtains  $T_o = 1.8 \times 10^8 \text{ K}$  (he notes this to be an increase of more than a factor of 100 over his own

Fig. 18. The low H concentration  $T_1$  data replotted in log-log form are presented with theoretical fits utilizing the theory of M&S with the field modulation for proton relaxation due to electronic exchange relaxation and hopping electron motion. The dotted line is a fit with constraint of the hopping prefactor. The dashed lines represent the expected temperature dependence for proton relaxation due to fluctuating electronic fields arising from the low temperature electronic exchange relaxation in the rapid diffusion (upper dashed) and diffusion limited (lower dashed) regimes of the theory of Rorschach (181). See text for discussion



previously reported data) from transport measurements on evaporated a-Si. Clearly, the present results from the fit to the proton NMR  $T_1$  data fall within the scatter of the above values.

One further point should be made about our  $T_0$  values. Using Eq. 78, the average of the  $T_0$  values obtained from the fits, and assuming the value of  $10 \text{ \AA}$  for the spatial extent of the wavefunction,  $r_0$ , one arrives at  $N(E_F) \sim 6 \times 10^{18} \text{ eV}^{-1} \text{ cm}^{-3}$ . This value is in very good agreement with the values of the density of states in the gap quoted in the introduction.

The value of  $\lambda$  from Eq. 77 obtained from the EPR data of Gourdon et al. (182) is  $\sim 1 \times 10^4 \text{ s}^{-1} \text{ K}^{-1}$  for the sample with the lowest concentration of dangling bonds ( $6 \times 10^{19} \text{ cm}^{-3}$ ); this value decreases with decreasing dangling bond concentration and would, therefore, approach even closer to the values we obtain from the fits (the average of the dangling bond concentration for the 4 and 7% H samples is  $\sim 1 \times 10^{19} \text{ cm}^{-3}$ , see Fig. 23).

It will be noticed that the values of the relaxation center concentration,  $n_s$ , for these two samples are very close--closer than the dangling bond concentrations of Fig. 23 would suggest. These concentrations are not very independently sensitive to the fit: the values of  $n_s$  and  $\lambda$  are very strongly correlated in the fitting process--an underestimation of  $n_s$  is easily compensated by an overestimation of  $\lambda$ , and other adjustments. The theory predicts a minimum in  $T_1$ , at high temperature. The value of  $T_1$  at this minimum would accurately yield  $n_s$ ; unfortunately, at the necessary temperatures implied by the other parameters one would expect considerable annealing and H motion, introducing other relaxation mechanisms and complicating the situation perhaps beyond resolution.

Regardless of the above shortcomings in accuracy of the  $n_s$  determinations, it seems clear that some form of center clustering is needed to explain the discrepancy between the EPR dangling bond concentration and the deduced values of  $n_s$ : on the basis of this discrepancy one expects the cluster density to be at least 10 centers per cluster. This would be consistent with our earlier conclusions with regard to regions or clusters of the third phase, pure a-Si, of the low H concentration samples.

It will be recalled (see introduction) that annealing reduces the dangling bond concentration of a-Si(H). If the hopping electrons associated with this dangling bond signal are responsible for the relaxation in the low H concentration samples, one expects that annealing would reduce the concentration of centers and therefore reduce the relaxation rate (increase  $T_1$ ). The 7% H sample has been annealed in the course of performing  $T_1$  measurements; after an anneal at 565 K the room temperature spin-lattice relaxation time,  $T_1$  (RT), was 31.2 s; after an anneal at 620 K,  $T_1$  (RT) = 60.7 s. Comparing this to the unannealed  $T_1$  value of 15 s, lends support to the supposition that the dangling bond electrons are the source of the relaxation.

It should be noted that the elaboration of the de Gennes theory due to Rorschach (181) will not account for the low temperature behavior of the  $T_1$  data with the correlation time given by Eq. 77. Both the fast diffusion regime (upper dashed line, Fig. 18) and the diffusion limited regime (lower dashed line) are at odds with the data. Whereas, the M&S theory seems to fit that regime very well.

d. Some protons even hop      Now we deal with the temperature dependence of  $T_1$  for the high H concentration samples. Perhaps the most



important trend in the data, evident in Fig. 16, is the decrease of the minimum with increasing H concentration: whatever the mechanism, the relaxation interaction must grow stronger with increased H concentration. This, of course, is directly in opposition to the trend apparent in the low H data. Therefore, one would not expect the relaxation mechanism for the high H concentration samples to involve the dangling bond electrons, since the concentration of these is still decreasing with increasing H content.

Carlos and Taylor (69) were the first to propose a model to explain the behavior of a-Si(H) samples that yield a minimum in the temperature dependence of the spin-lattice relaxation time. Their model consisted of relaxation centers augmented by spin diffusion. The center was postulated to be a proton that hopped back and forth very rapidly between two nearly isoenergetic configurations (called disorder modes). This hopping motion would give rise to a time-dependent modulation of the dipolar field felt by neighboring protons, producing a direct relaxation rate given by Eq. 61, with the relaxation of the remaining protons proceeding via spin diffusion.

Movaghar and Schweitzer (114, 115) quickly pointed out that the concentration of such hopping protons required to explain the depth of the minimum would have to be very large (at least 10%) and therefore directly observable in the NMR spectrum. These centers would be extremely quickly relaxing; nothing like this has been observed.

Conradi and Norberg (116) then asserted that if relatively small concentrations of molecular H ( $H_2$ ) were presumed trapped in the network of the material the relaxation data could be explained. The fluctuations of

the dipolar field produced by the ortho state (nuclear spin = 1) of the  $H_2$  molecule would provide the perturbation to induce the relaxation of neighboring spins, and, once again, spin diffusion would provide the relaxation of the other protons.

We propose that the model of C&T can indeed account for the temperature dependence of  $T_1$  in these high H concentration samples. Resurrecting the C&T model involves an important modification: the source of the failure of the original model is the relatively small fluctuating field provided by a hopping proton. If the hopping motion of the proton were augmented by the concomitant fluctuation of an electronic dipolar field, then the strength of the fluctuating field would be enhanced by a factor of  $\sim 700$ . Thus, we propose that the centers responsible for the relaxation are the "three center bonds" discussed in the introduction. The model may be understood in the following fashion.

In the amorphous network, it is probable that occasionally, especially as the H concentration is increased, a Si-H bond will be in close proximity to a dangling Si bond. This configuration may be viewed as a three center bond. The H atom would be in a lower energy state closer to one or the other Si atoms; there would arise a considerable probability of phonon assisted hopping or tunneling motion between the two quasi-equilibrium positions. This motion of the proton would cause violent fluctuations in the dipolar field emanating from either of the two Si electrons involved in the bond: the dipolar field would oscillate because the spatial position of the source changes, as first one then the other Si electron is bonded to the H atom; further, this two center bond breaking would be expected to provide immediate longitudinal relaxation for the unpaired electronic spin.

For most of the neighboring protons the fluctuations due to the longitudinal relaxation will be the most important.

We again apply the theory of Movaghar and Schweitzer (115). (Note that we are just on the edge of the strong center regime, Eq. 79. The diffusion limited results of Rorschach (181) may be more appropriate; in any case, the results are expected to be qualitatively similar.) However, the shallow nature of the minimum will require some effort to understand. This will be dealt with in two very different ways.

Initially, in an effort to incorporate the nonexponential recoveries into the model, it was supposed that at any particular temperature there would be a distribution of correlation times,  $t_c$ , for the fluctuations of the relaxation center fields (and therefore a distribution of direct relaxation times via Eq. 61). This distribution in correlation time was believed to correspond to the rather sensible notion that at some of these sites the proton may "find it easier" to make the jump than at other sites: one would expect to encounter a distribution of energy barriers for the jump on the basis of the disorder, and thus a distribution of correlation times.

With this view the average value of  $T_1$  (recall that we are dealing with an average in "some sense") should obey an expression of the form

$$\left\langle \frac{1}{T_1} \right\rangle = \int_{E_m}^{E_M} P(E)R(E)dE \quad , \quad (81a)$$

where  $R(E)$  is the relaxation rate of protons associated with a center of barrier energy,  $E$ , given, through Eqs. 79 and 80, by

$$R(E) = K n_s \left[ \frac{t_c}{1 + v_o^2 t_c^2} \right]^{1/2} \quad (81b)$$

The hopping rate will be given by

$$\frac{1}{t_c} = v_{oH} e^{-E/kT}, \quad (82)$$

and the probability distribution for energy barrier heights will be the simplest possible:

$$P(E) = \frac{1}{E_M - E_m}, \quad E_m < E < E_M \quad (83)$$

$P(E) = 0$  otherwise, where  $E_M$  and  $E_m$  are, respectively, the maximum and minimum of the energy barrier distribution. We finally have a very difficult integral to do. In fact, it turns out to be a sum of the elliptic integrals of the first and second kind. This would create ponderous, but not insurmountable programming difficulties in the fitting routine used (179). The essential physics can be obtained by going back to our definition of the average in Eq. 81, claiming that just as reasonable an average may be obtained by defining it in the rms sense (recall that we are concerned with relaxation times that are "average in some sense"):

$$\left\langle \frac{1}{T_1} \right\rangle = \left[ \int_{E_m}^{E_M} P(E) R^2(E) \right]^{1/2} \quad (84)$$

The integral is trivial and we have

$$\langle \frac{1}{T_1} \rangle = K n_s \left\{ \frac{kT}{(E_M - E_m) v_{OH}} \left[ \arctan \left( \frac{v_o}{v_{OH}} e^{E_M/kT} \right) - \arctan \left( \frac{v_o}{v_{OH}} e^{E_m/kT} \right) \right] \right\}^{1/2} \quad (85)$$

Now, this expression is very similar to that originally used by C&T, and even more similar (not surprisingly) to the expression derived by M&S in their treatment of the C&T disorder mode model; since we have invoked electronic field fluctuations as the source of the relaxation, the valid objections of M&S to the model of C&T do not apply. However, application of Eq. 85 in the fitting routine simply will not fit the data, see Fig. 19. A little reflection reveals the physical reason: clearly, with any kind of averaging process the slope of the flanks of the minimum will be determined by the maximum and minimum of the barrier energy for the high and low temperature sides of the  $T_1$  minimum, respectively. This minimum is so broad that any attempt to match the slopes on both sides of the minimum will yield such disparate barrier energies that the double  $T_1$  minimum structure corresponding to the two extremes in activation energy will develop.

Another approach must be taken. If the proton motion is indeed phonon assisted, there should be a distribution in correlation times for any given center, reflecting the density of states of phonons. Thus, any center would see many correlation times; the value of a particular correlation frequency would depend upon the energy of the most recently scattered phonon. We are then permitted to define an average correlation frequency by

$$\langle \frac{1}{t_c} \rangle = \int_{E_m}^{E_M} P(E) \frac{1}{t_c(E)} dE = \frac{v_{OH} kT}{(E_M - E_m)} (e^{-E_m/kT} - e^{-E_M/kT}) \quad (86)$$

where once again the simplest distribution of "effective" jump energies has been assumed ("effective" because the effects of the scattered phonon have been taken into account).

Repeating, for convenience, Eq. 79,  $T_1$  is then given by

$$\frac{1}{T_1} = K n_s \left[ \frac{\langle t_c \rangle}{1 + v_o^2 \langle t_c \rangle^2} \right]^{1/2}, \quad (87)$$

with  $\langle t_c \rangle$  given by Eq. 86. A computer optimized fit of the 17% H data appears in Fig. 19. The data are fit very well with this scheme. In fact, all of the high H concentration relaxation data may be understood in terms of this model, see Fig. 20. The results of these fits appear in Table 3.

As mentioned in the introduction, C&T have completed very conclusive experimental work in which they observed drastic increases in the proton  $T_1$  as a result of holding the samples at liquid He temperature for months. This is consistent with the expected conversion of  $H_2$  from ortho (spin = 1) to para (spin = 0, and therefore not effective as a relaxation center) at low temperatures. C&T's work was done exclusively on GD material; it is seen by the very poor results of attempting to fit the present data with the C&N model that significant amounts of  $H_2$  do not exist in Ames Lab rf sputtered a-Si(H). It is possible to understand why GD material would have significantly more  $H_2$  than RS a-Si(H).

Fig. 19. The 17% H  $T_1$  data are replotted with an expanded vertical scale. Also shown are theoretical fits using Eq. 85 (short-long dashes); the theory of C&N (dashes) - here the most extreme, and very unphysical, values of the C&N parameters were used to generate this best possible fit; and finally the theory which culminates in Eqs. 86 and 87 (solid), utilizing the approach of M&S with an average correlation frequency associated with fluctuating electronic fields, originating in the phonon assisted hopping of protons (see text for details)

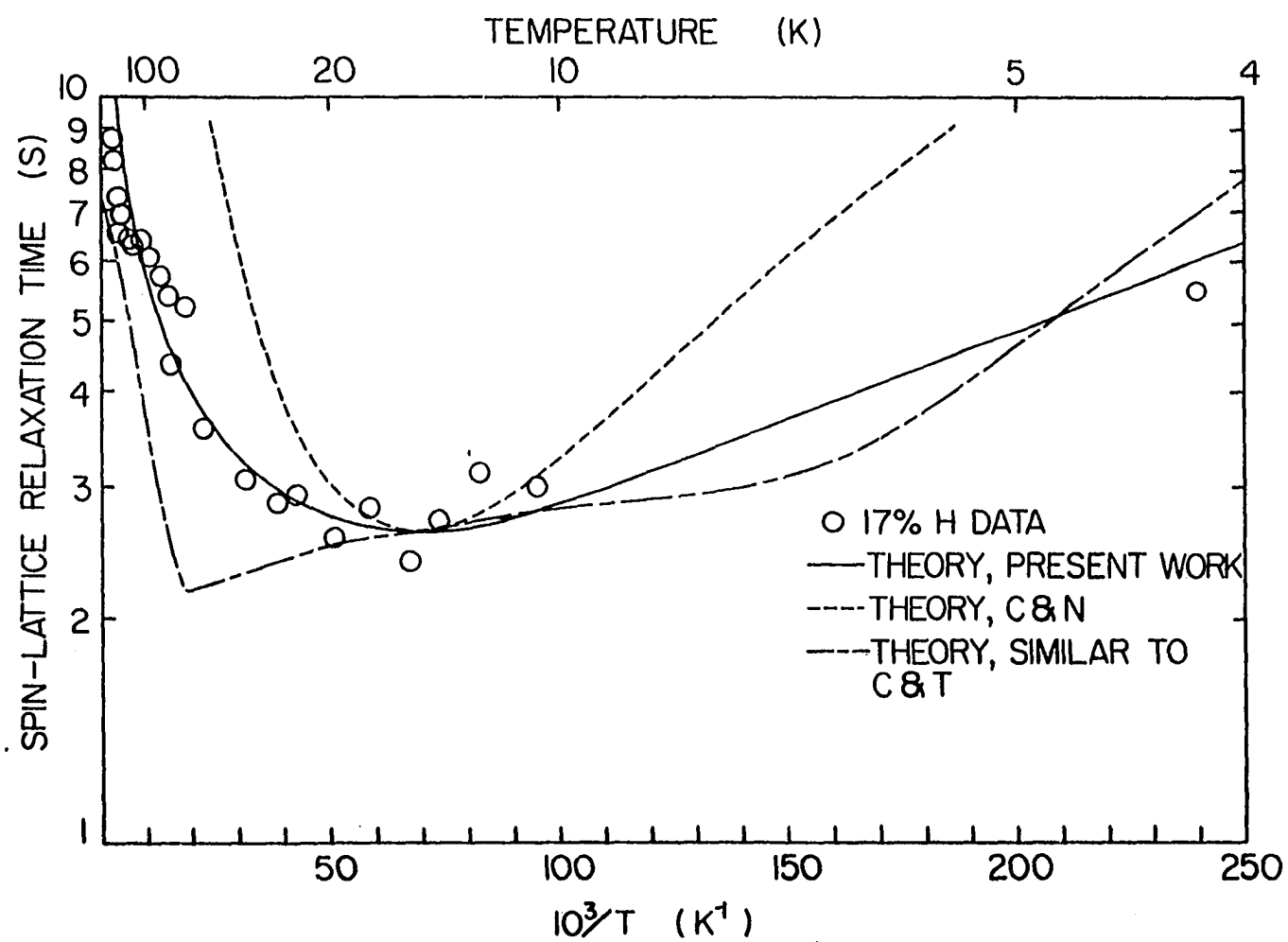




Fig. 20. The high H concentration data are fit very well by assuming that  $T_1$  is given by Eqs. 86 and 87. The optimized fit parameters appear in Table 3

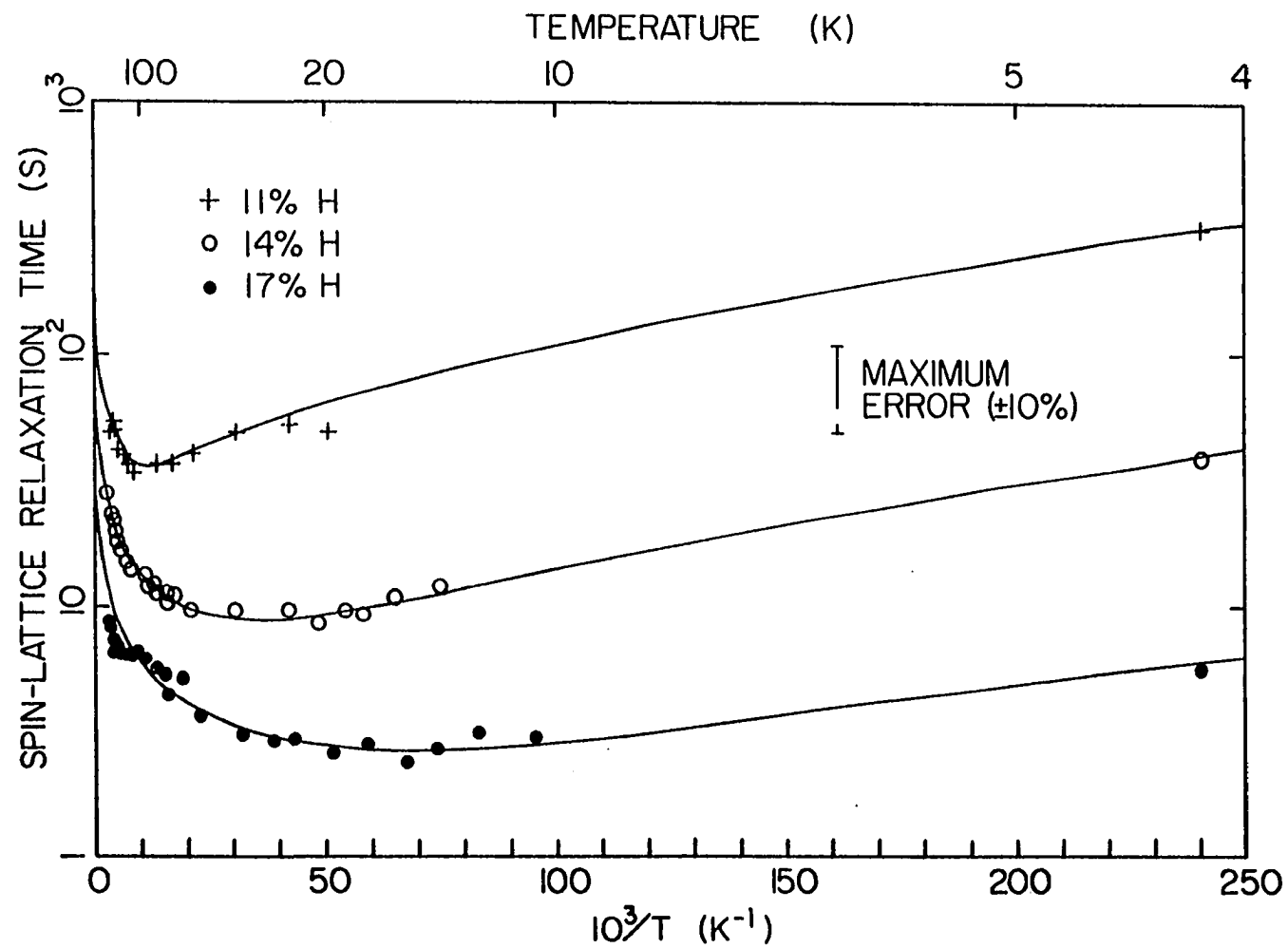


Table 3. Results of computer optimized fitting of  $T_1$  vs. temperature data in high H concentration regime

H content (%)	Concentration of centers, $n_s$ (cm <sup>-3</sup> )	Hopping frequency prefactor, $\nu_{oH}$ (Hz)	"Effective" barrier energy minimum, $E_m$ (eV)	"Effective" barrier energy maximum, $E_M$ (eV)
11	$5.0 \times 10^{16}$	$3.6 \times 10^9$	$7.0 \times 10^{-4}$	0.70
15	$2.1 \times 10^{17}$	$8.98 \times 10^9$	$7.8 \times 10^{-4}$	0.45
17	$7.0 \times 10^{17}$	$1.85 \times 10^{10}$	$5.5 \times 10^{-4}$	0.44

The GD material used by C&T was deposited on a heated substrate ( $\sim 300$  C). The RS  $\alpha$ -Si(H) produced at the Ames Lab was not deposited on a heated substrate; the necessary dihydride bond-breaking energy was supplied only to the film growth surface from the effective high temperature of the high power rf plasma. It is conceivable that the heat supplied continually to the entire film in the GD case increases the mobility of weakly or unbound H atoms for such an extended time that the probability of two H atoms coming close enough to form a molecular bond increases significantly compared to the RS case.

Furthermore, the  $T_1$  values at the proton  $T_1$  minimum observed by C&T are usually quite small (0.3 S), whereas the values we observe range from a factor of  $\sim 10$  to  $\sim 100$  larger. The point is that there could exist centers in the GD films of the sort propounded here, but the stronger relaxation effects of the  $H_2$  present in the GD films would overshadow the effects of the former.

To summarize this section on NMR spin-lattice relaxation, data and discussions have been presented which strongly suggest the existence of two distinct types of relaxation centers: proton relaxation occurs through the fluctuating longitudinal dipolar field of electrons; the fluctuations are created by the hopping motion of the electron itself or by the hopping motion of a proton in a "three center bond" in the low H and high H concentration regimes, respectively.

## B. EPR Results

### 1. Narrow scan EPR results

The signals appearing in Fig. 21 will be familiar to anyone who has worked in the a-Si(H) field; they are the dangling bond signals whose correlation with the hopping motion of electrons, particularly in the low H concentration regime, has been discussed in the introduction and in this chapter. Here the signals are displayed for the samples in the full H concentration series. It should be noted that the line shape progresses from nearly Lorentzian to nearly Gaussian with increasing H concentration. Even though the sources of the linewidth are manifold and not always clearly elucidated, most workers agree that a considerable amount of exchange narrowing of the line occurs at high dangling bond concentrations (recall that exchange produces a Lorentzian lineshape). This supports our earlier conclusion that the low H concentration samples contain considerable clusters of pure a-Si, where the concentration of dangling bonds will bring nearest neighbors within the  $10^{\circ}$  Å extent of the electronic wavefunction (necessary for exchange to take place).

Evidence of structure in the high field peak of the derivative spectrum for the 17% H sample may be discerned in Fig. 21. By operating at higher microwave powers the dangling bond signal begins to critically saturate, and a very narrow resonance is discovered superposed upon the dangling bond signal; see Fig. 22. The approximate g value and width of this line indicate that it is probably due to the Si-E' center, see Holzenkampfer et al. (187): the E' center is a "dangling"  $sp^3$  orbital on a Si atom whose other  $sp^3$  orbitals are tied-up with bonds to oxygen.

Fig. 21. The well-known "dangling bond" EPR signals are presented as a function of total H concentration for the samples of the series. The dotted lines on the downfield derivative peak for the first 3 spectra are Lorentzian lineshape function points; this will guide the eye in following the trend of the lineshape from nearly Lorentzian to nearly Gaussian with increasing H concentration

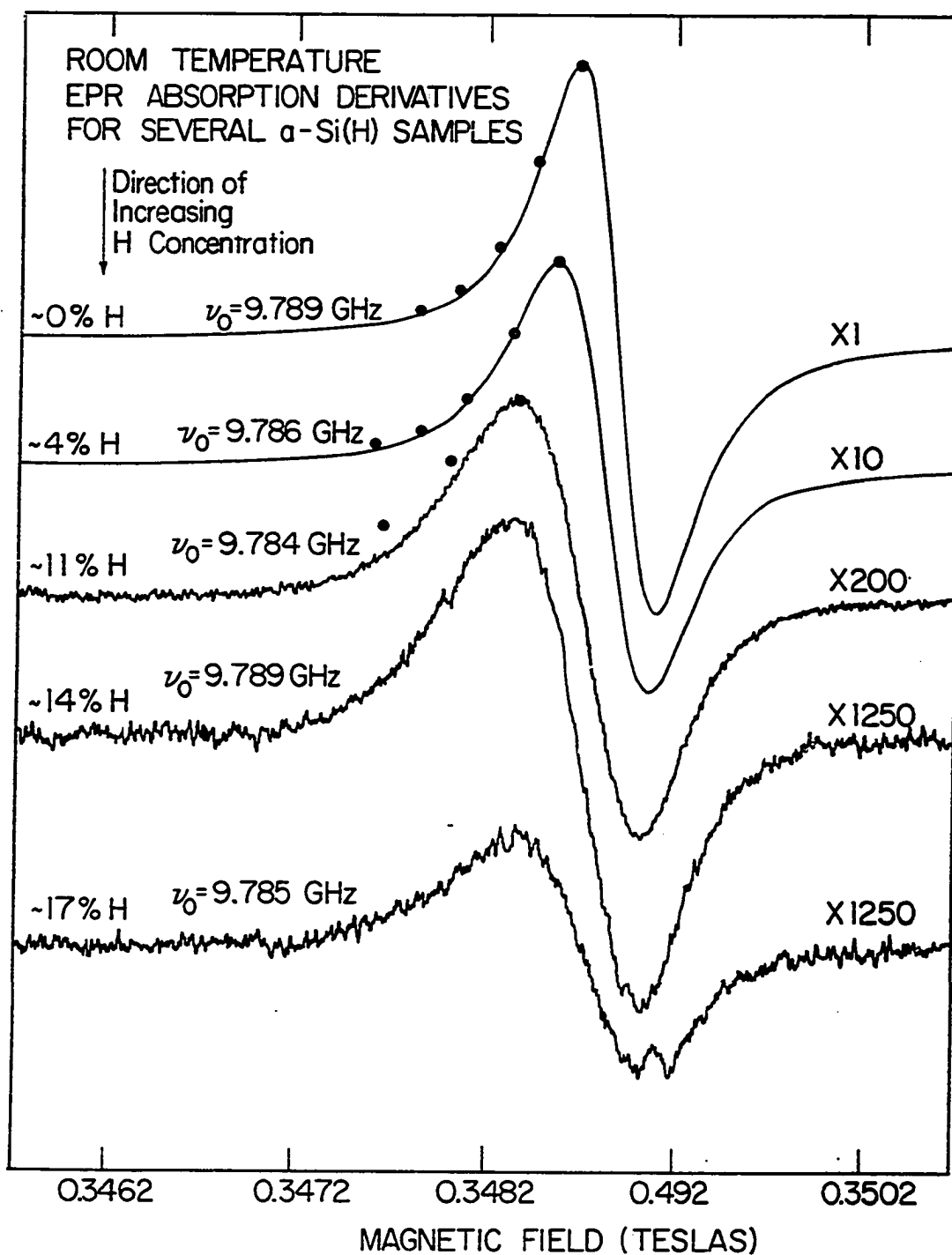
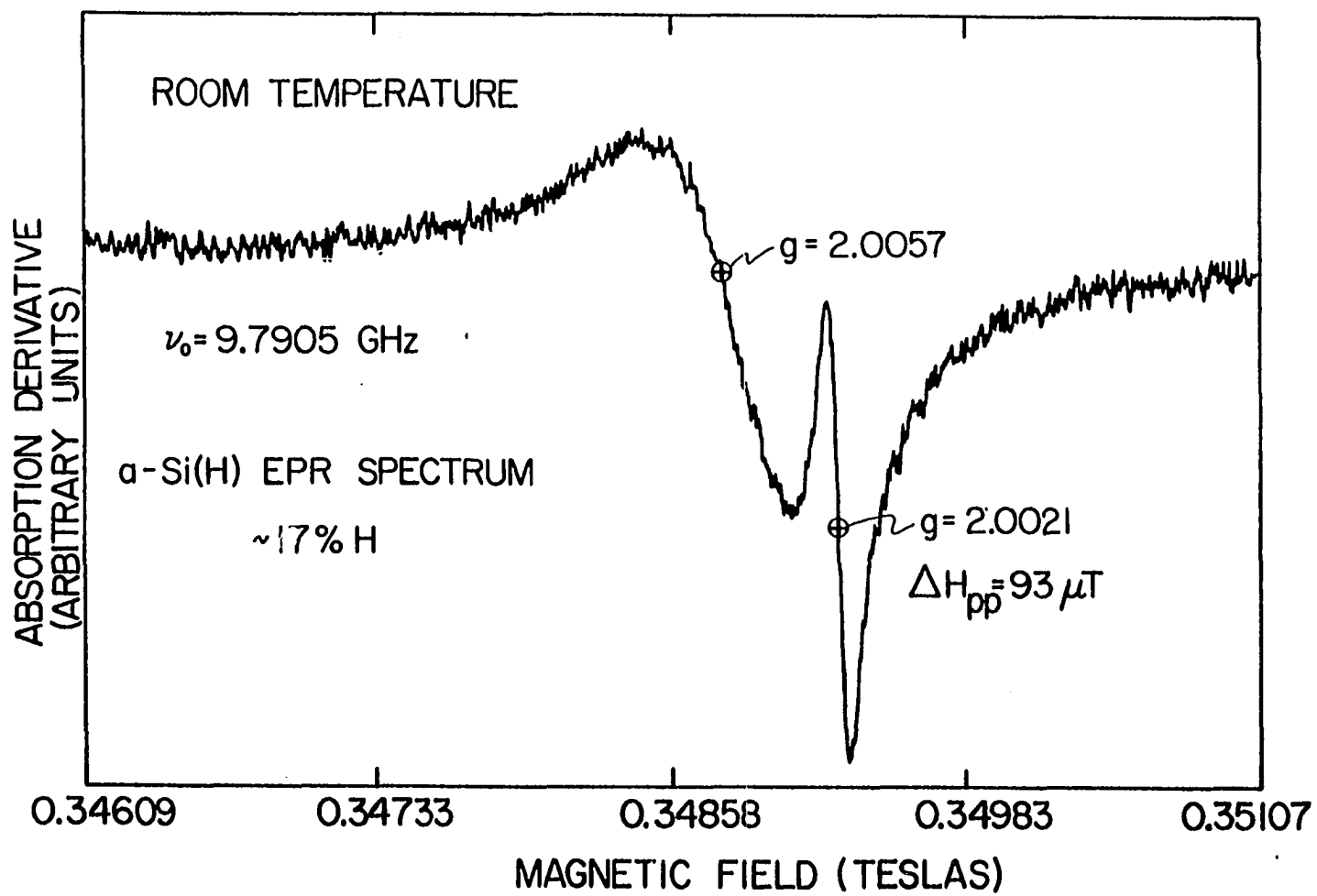


Fig. 22. The dangling bond signal for the 17% H sample is shown at 196 mW of microwave power; this enhances the very narrow line with respect to the dangling bond resonance due to preferential saturation of the latter. This very narrow line is thought to be a close cousin of the Si-E' center. See text for the structural significance of this





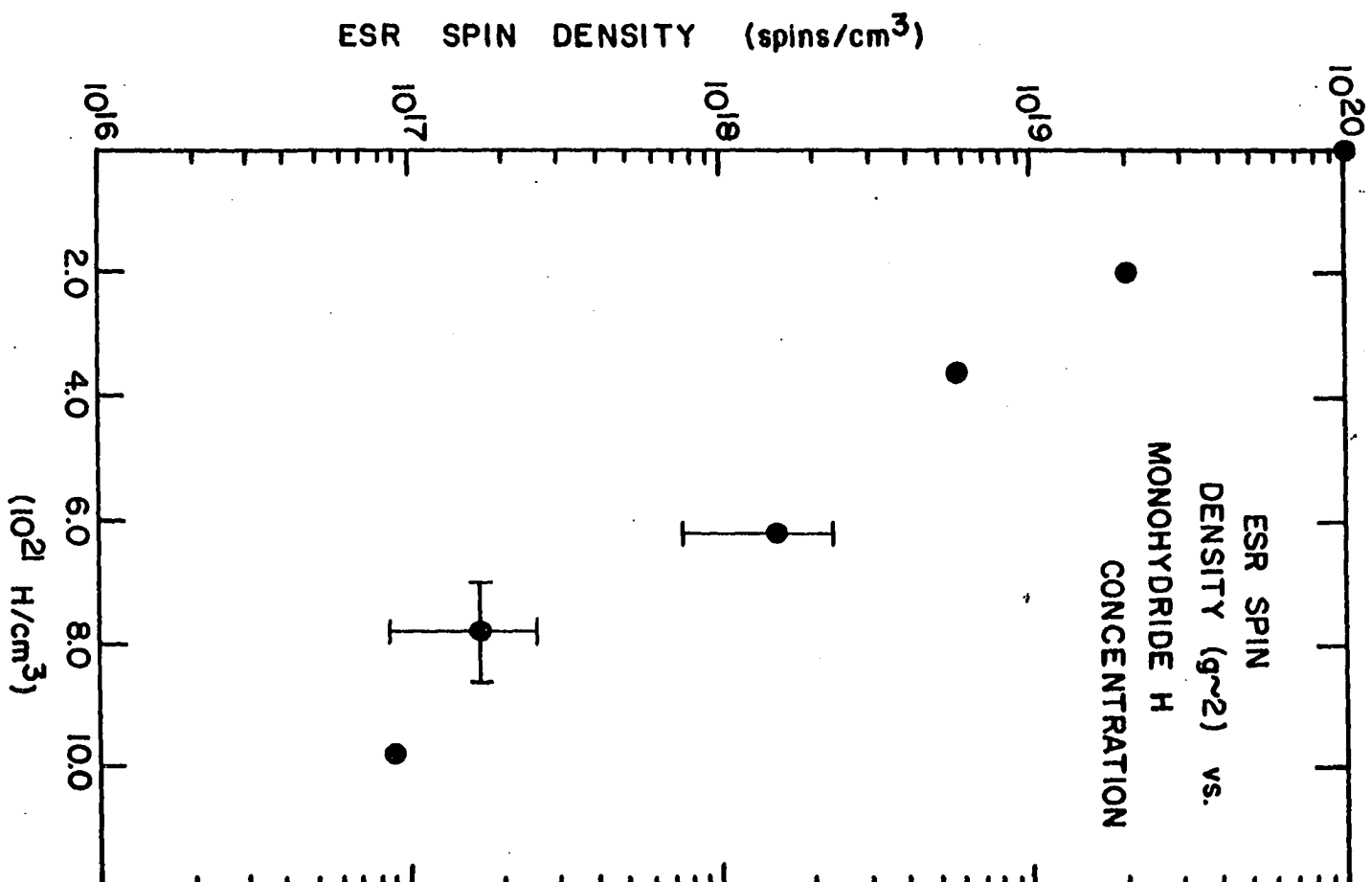
There are some differences between the resonance seen here and the work of Holzenkampfer et al. Here a  $g$  value of  $2.0021 \pm .0005$  is measured; they report a value slightly lower,  $g = 2.00010$ . The discrepancies are reconcilable if one assumes that both values are at the extremes of their respective tolerances, still the differences are probably real. Further, the linewidths here are smaller by a factor of 2-3; perhaps this is due to exchange effects with neighboring defects.

The above discrepancies notwithstanding, the existence of considerable oxygen contamination in the highest H content film is consistent with our earlier conclusions regarding H clustering. If one assumes that the H clusters are on the surfaces of voids which are rather fissure-like, significant migration of  $O_2$  throughout the bulk of the film could occur.

Saturation studies were executed on the dangling bond resonances of the low H concentration samples, see section III.D.3. The  $T_{1e}$  estimates from the saturation studies were  $6.9 \times 10^{-8}$  s and  $1.3 \times 10^{-6}$  s for the 4% and 7% H samples, respectively. If one uses the parameters from the NMR  $T_1$  fits to calculate  $T_{1e}$  via Eq. 77 the results are  $2.4 \times 10^{-7}$  s and  $3.2 \times 10^{-6}$  or  $3.3 \times 10^{-6}$  s (depending on which fitting results are used) for the 4% H and 7% H samples, respectively. This is excellent agreement considering the approximate nature of the EPR relaxation measurement and the scarcity of NMR  $T_1$  data for the 4% H sample.

The spectra in Fig. 21 have been analyzed to determine the total concentration of dangling bonds using the methods outlined in section III.D.2; the results are summarized in Fig. 23. The error bars indicate the probable statistical error in the measurements; there are two sources of

Fig. 23. The dangling bond spin density is shown to decrease exponentially at first with increasing H concentration. The two highest H concentration points give the appearance that the dangling bond signal may level off at higher concentrations



systematic error. The first has been discussed in section III.D.2 and had to do with the fact that the lineshapes are changing as a function of H concentration. The second is probably minor: one or two of the higher concentration samples may be slightly saturated. The net effect of these systematic errors will be to slightly underestimate the dangling bond concentration in the higher H concentration samples.

In an effort to measure the dangling bond concentrations more accurately (without resorting to time consuming fitting procedures), attempts were made to numerically integrate the dangling bond signal. Difficulties soon appeared in the form of "spurious baseline drifts" (so it was thought) which, understandably, made the integration ambiguous. It was, however, discovered that this baseline effect was not due to background: another huge resonance in the sample was creating the effect. This is a completely new resonance. Further attempts at improving the dangling bond density measurements were quickly dropped in favor of exploring this new and very intense resonant absorption of microwave energy.

## 2. Wide scan EPR results

Figure 24 details the results of expanding the sweep width to .6 Tesla. Every sample in the series shows a broad resonance (width ~.1 Tesla). The two lowest H concentration samples appear to manifest a broad resonance at anomalously high g values. Figure 25 demonstrates that a very large g shift results when the 7% H sample is cooled to 77 K. Figure 26 establishes that this temperature dependent g shift is a common feature of all the samples. The trend of the g shift between room temperature and liquid N<sub>2</sub> temperature is shown in Fig. 27.

Fig. 24. A new field dependent microwave absorption is presented; the width is  $\sim 0.1$  T. There doesn't appear to be any sensible correlation with the H concentration, unfortunately. However, notice the superposed, narrower broad line in the 15% H sample; the cause of this is to be discussed later. The dangling bond resonance is visible in all samples (except the 15% H, although it is visible on a better scale). This resonance can serve as a g value marker — the frequencies of operation have been significantly shifted in some cases

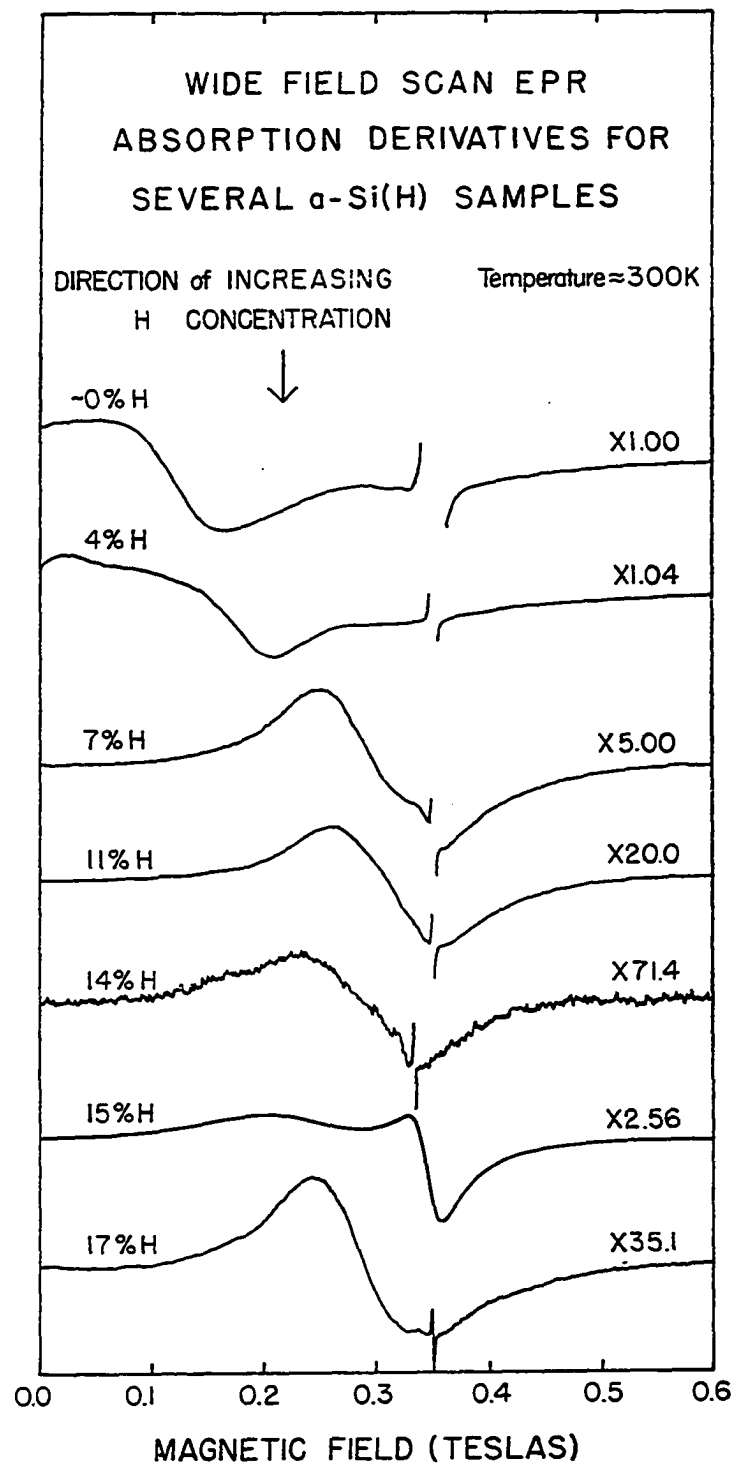


Fig. 25. The broad new EPR resonance exhibits a remarkable downfield shift with decreasing temperature; it is here exemplified by data from the 7% H sample. The dangling bond resonances are truncated but still visible; they may serve as a point of reference



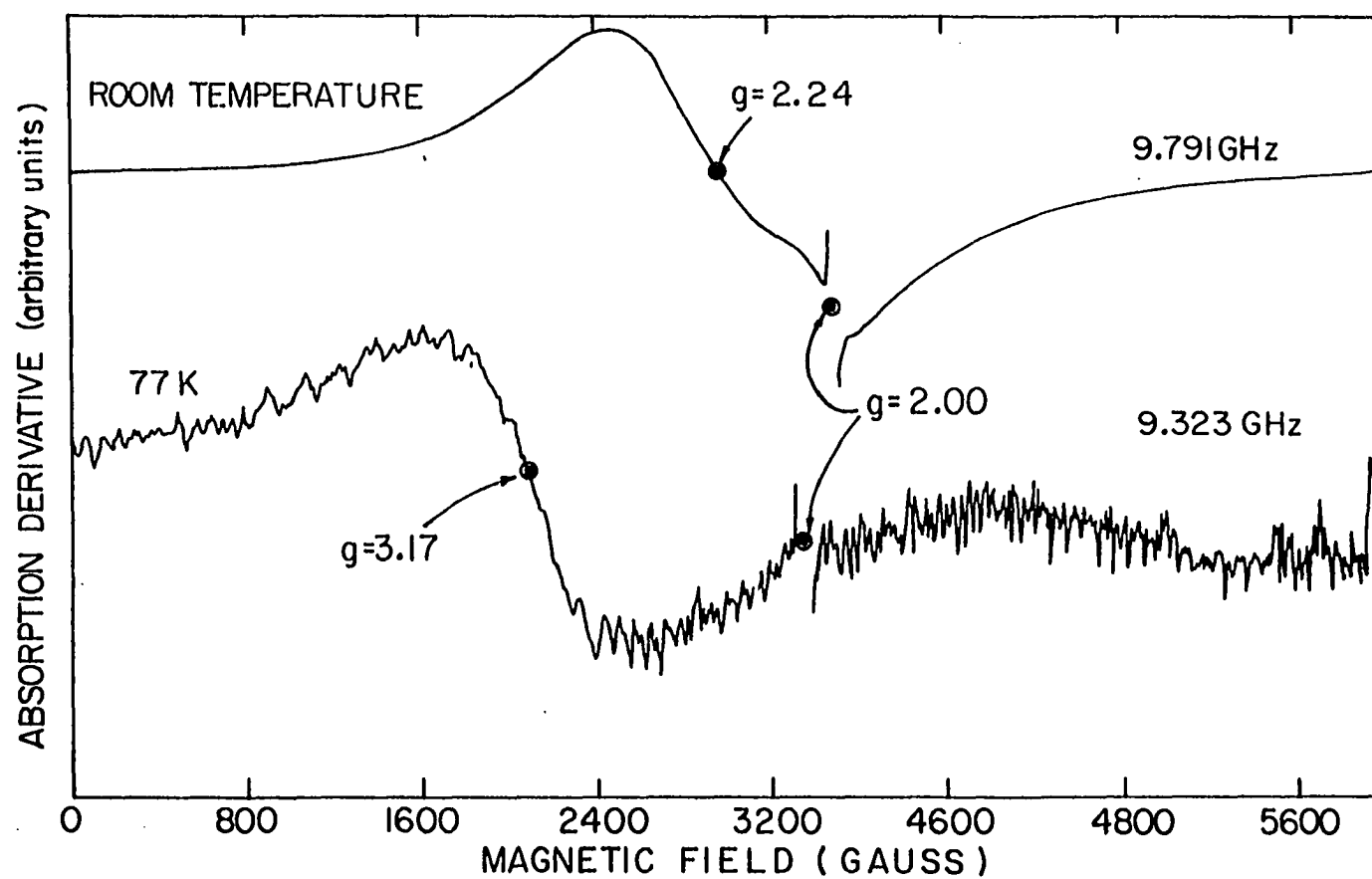


Fig. 26. The broad resonances, at liquid N<sub>2</sub> temperature, are presented for most samples in the series. Again the dangling bond resonance serves as a reference point

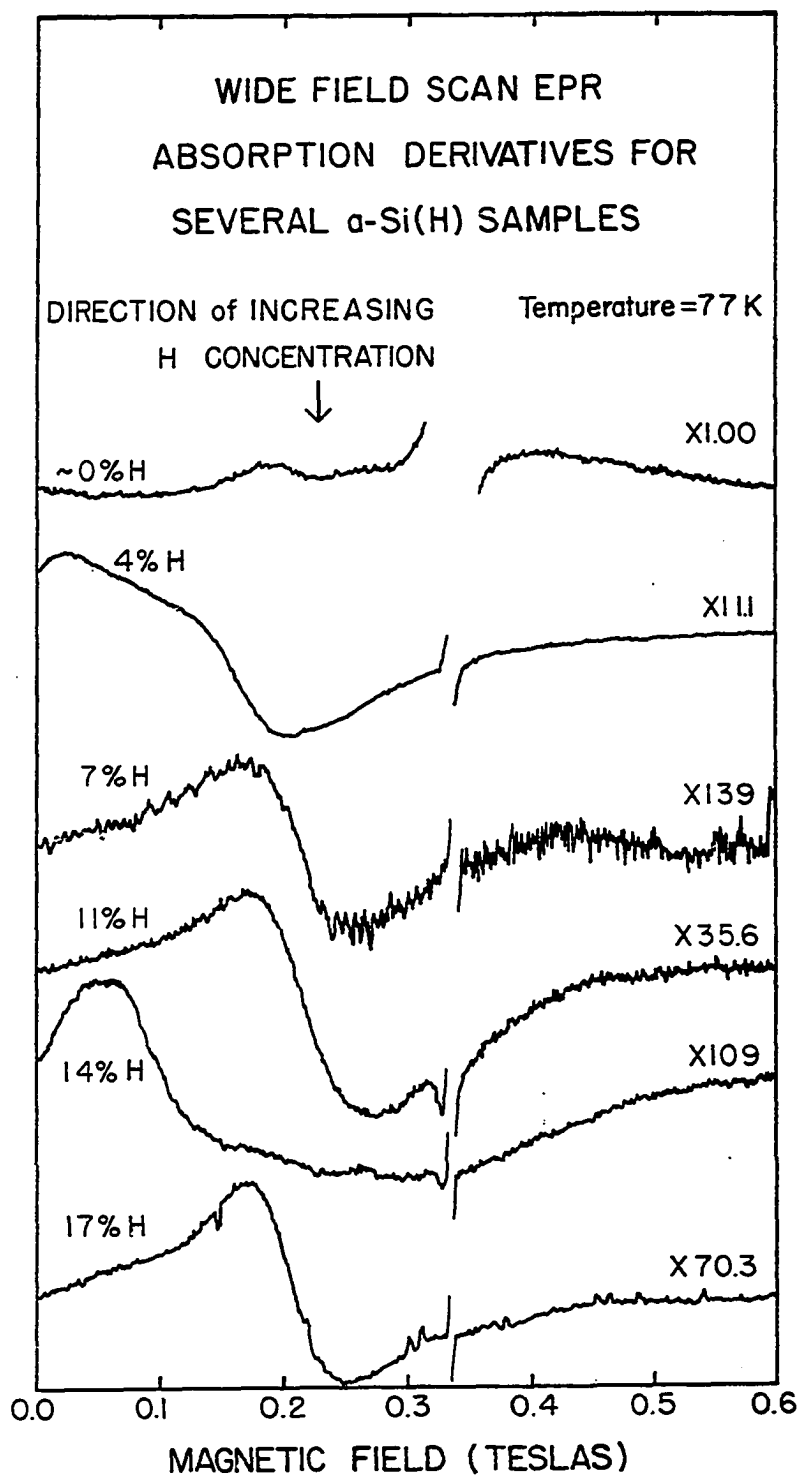
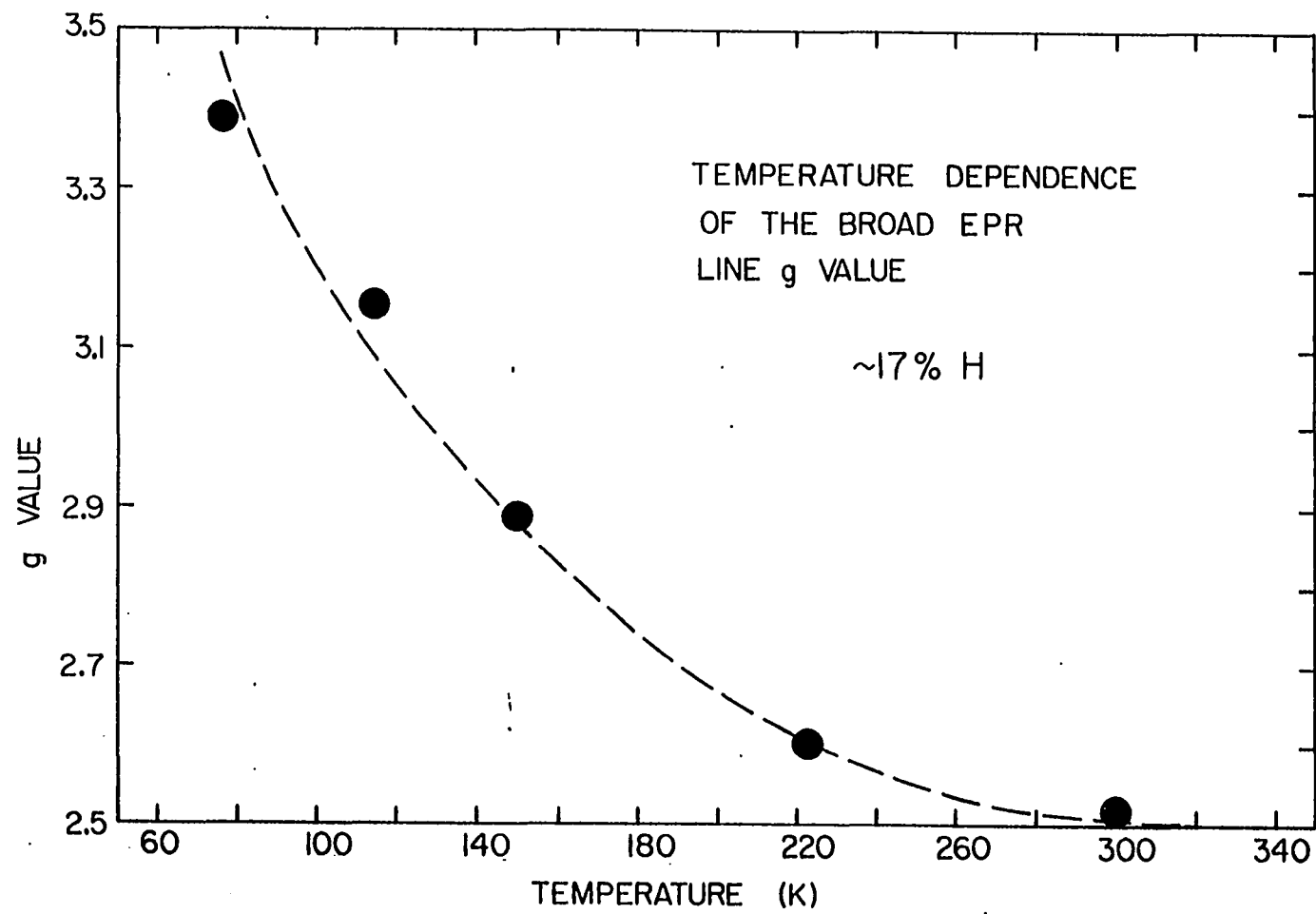


Fig. 27. Here the very strong positive g value shift with decreasing temperature is evident. The dashed line accommodates the eye to the trend



Saturation studies have been carried out on the broad resonance for several of the samples: the signal intensities appear to follow the power law discussed in section III.D.3 without any sign of saturation. This places the upper bound on the spin-lattice relaxation time at  $\sim 10^{-10}$  s; lifetime broadening of the resonance is then a possibility in trying to account for its huge width.

If one applies the principles of EPR spin counting discussed earlier to a calculation of the concentration of these centers, for example to the 7% H sample, the incredible result of  $\sim 10$  at. % is reached; this is due to the 'square of the linewidth' factor, present in the formula for the spin density. Is there some mechanism by which the integrated intensity of the absorption line may be increased because of lifetime effects?

The first suspected cause of this new broad resonance was the existence of some form of paramagnetic "dirt" in the samples. However, this can be eliminated for two reasons: First, spark source mass spectroscopic analyses have been carried out on several of the samples (see Appendix B); there were no paramagnetic impurities of significant concentration found. Second, if that many "normal" paramagnetic centers were present (excluding very tight clusters) the proton spin-lattice relaxation times would be expected to be very much smaller than they are.

After the initial discovery of this resonance, the author hoped there would be some way to account for its tremendous absorption of microwave energy in terms of some kind of coupling between one of the hopping protons of section IV.A.2.d and a dangling bond (similar to the proton rotational tunnelling phenomena found in free-radical methyl groups (188,189,190,191, 192)). Interestingly, ref. 188 discusses instances of nonexponential spin-

lattice relaxation via quantum mechanical tunnelling motion of the proton. An appropriate theory for this case has been hard to come by. Nonetheless, we have established empirically that protons are in some way involved with this microwave resonant absorption.

Several samples containing both hydrogen and deuterium had been prepared. Their wide line EPR spectra appear in Fig. 28. The approximate linewidths of the two overlapping lines are very closely in the same ratio as the hyperfine fields of H and D. This resonance which is presumably associated with D also appears in the 15% H sample signal of Fig. 24. Investigation revealed that this sample was prepared either very soon after or slightly before several deuterated samples were sputtered. It had previously been established (by proton spin counting in a presumably pure a-Si sample, no H, which had an actual H concentration of ~4%) that the sputtering target has a considerable "memory," i.e. it retains much of the reactive sputtering gas in grain boundaries from one run to the next.

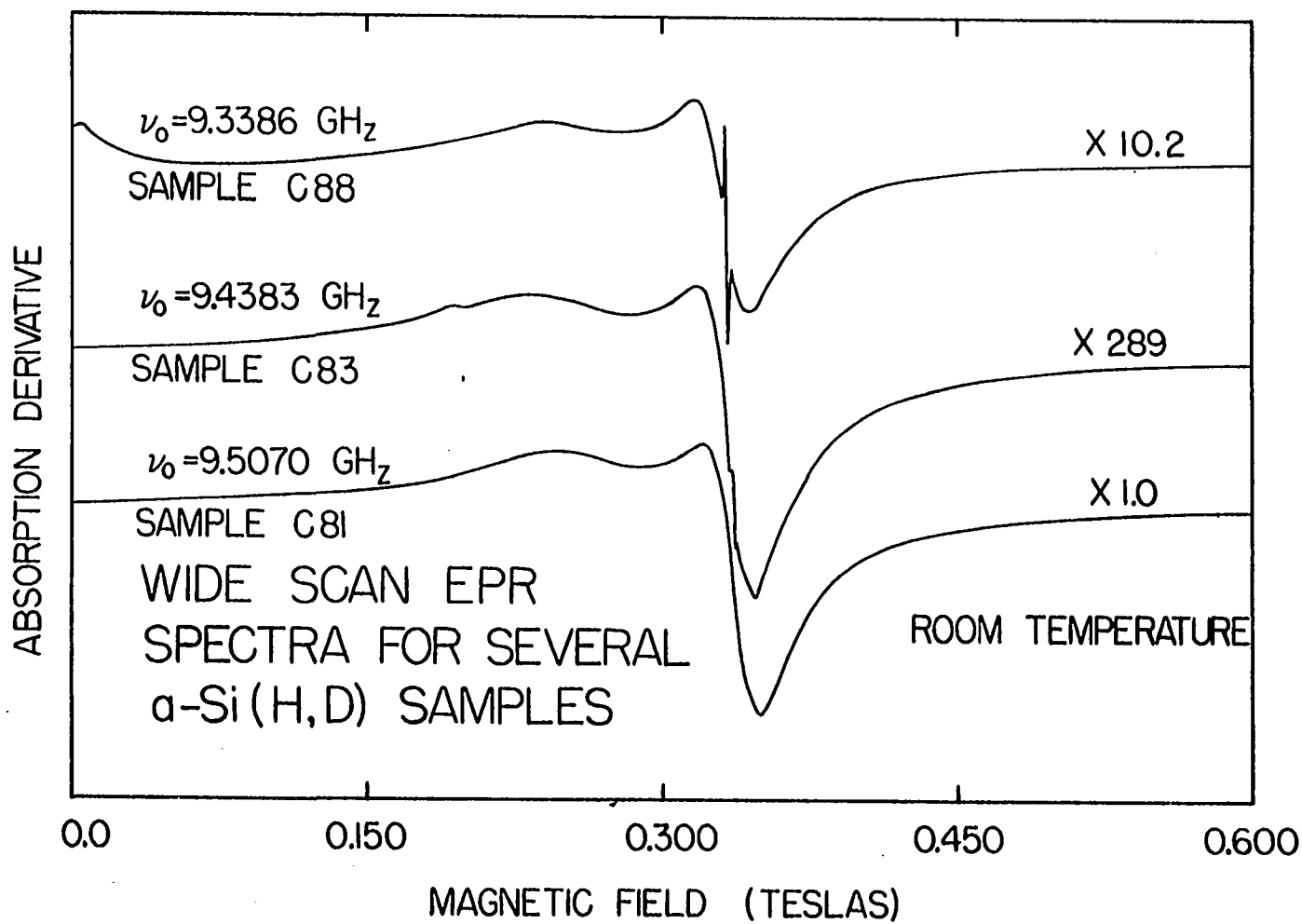
There is another remote possibility that may account for the broad EPR absorption. The dependence of the g value on temperature and the width of the resonance are consistent with resonances which have been observed in spin glass systems (193). It would seem difficult to account for the long proton  $T_1$  in this case, however.

The isotope effect present in the wide microwave resonances almost certainly establishes that generic hydrogen is associated with them. At this point further discussion would be very speculative: much more work remains to be done.

The next chapter will summarize the conclusions, and attempt to assess their implications.

Fig. 28. Here are the wide sweep EPR results at room temperature for the three samples that were deposited by rf sputtering in a plasma with hydrogen and deuterium. Each of these spectra may be decomposed into 3 distinct absorption lines. The very narrow ( $\sim 500 \mu\text{T}$ )  $g = 2.0055$  dangling bond resonance is evident in each spectrum (although for sample C81 it is not visible on this scale). The broader features are the two remaining absorption lines. An "eyeball decomposition" yields a very broad line at  $g \approx 2.5$  ( $H_0 \sim 0.27 \text{ T}$ ) with width  $\approx 90 \text{ mT}$ ; this is identified with the broad resonance apparent in the spectra of Fig. 24. The new feature apparent in these spectra is the absorption line at  $g \approx 2.04$  ( $H_0 = 0.328 \text{ T}$ ) with width  $\approx 28 \text{ mT}$ ; this narrower resonance is associated with the presence of deuterium in the material. See text for discussion





V. CONCLUSIONS, ANOMALOUS RESULTS, AND  
SUGGESTIONS FOR FUTURE WORK

A. Summary

A number of conclusions may be drawn concerning the structure, etc. of RS a-Si(H), some with substantial confidence:

1) Evidence of NMR lineshape analyses leads to the conclusion that RS a-Si(H) is a material with a high degree of intermediate range disorder. The material is actually an aggregate, in general, made up of regions of three distinct phases: an amorphous random alloy of hydrogen and silicon, which has been designated here as a-Si:H; another "phase" which is distinguished by a high degree of NET-Si-H bond clustering (where NET stands for the random a-Si:H alloy network) and is more properly recognized as a defect in the a-Si:H network structure with the designation HC (for hydrogen cluster)-which may be understood as bonded H clustered on the surfaces of microvoids (of undetermined size, yet approximately constant local H density); and a third phase which is pure amorphous silicon and simply designated a-Si.

2) The above conclusions are consistent with ir (infrared) absorption data that may be interpreted in terms of two types of Si-H bond: a closely clustered type and a randomly distributed more dilute class.

3) There is a critical combination of H partial pressure and Ar partial pressure during sputter deposition at which the film is deposited without the inclusion of the nonhydrogenated pure a-Si phase; other sputtering parameters may affect this combination in ways that are not yet clear. The critical sputtering parameters may be estimated by an interpolation between the parameters of samples C52 and C51, see Table 1.

4) Proton spin-lattice relaxation measurements in conjunction with EPR measurements on the low H concentration samples indicate the presence of clusters of material in which considerable electron hopping takes place. This is consistent with 1) above.

5) Proton spin-lattice relaxation measurements on the high H concentration samples have suggested the presence of a "three center bond" involving one hydrogen and two silicon atoms. The proton moves between two quasi-equilibrium positions near either silicon atom via phonon assisted hopping or tunnelling.

6) Very wide field sweep EPR measurements on hydrogenated and deuterated/hydrogenated amorphous silicon samples may be tentatively interpreted in support of 5) above. However, the H concentration dependence of the intensity is anomalous.

#### B. Consequences for Transport Measurements and Device Properties

It is widely recognized that one of the outstanding problems associated with the successful interpretation of transport property (or, for that matter, any physical property) measurements in the field of amorphous materials is lack of adequate material characterization--too often measurements are carried out on materials whose fundamental structural characteristics are either unknown or ambiguous, making any significant progress in either understanding the physical principles germane to amorphous materials or improving device properties of those materials a nearly random process.

A case in point is the conclusion outlined in 1) above. It had been known for some time that there seemed to be a "magic" concentration ( $\sim 10\%$ ) of hydrogen that rendered either GD or RS a-Si(H) very much better as a device material. Until now, the exact mechanism behind the "magic" was unknown. The existence of regions of pure a-Si in what was thought to be homogeneous a-Si(H) will obviously provide an obstacle to efficient conduction and drastically affect photocarrier recombination times; similarly, when the H concentration exceeds the "magic" value the incorporation of too much clustered H will be to the detriment of effective transport.

Further, the possibility of "three center bonds" will have to be taken into account when attempting to understand the band structure or anomalous carrier trapping and scattering phenomena of these amorphous materials.

It is also important to recognize that the existence of intermediate range disorder (inhomogeneity) severely confuses the effects of quantitative and point topological disorder. The proper identification of instances of intermediate range disorder may lead to preparation techniques that are better able to avoid these material inhomogeneities; this will open the way for a better understanding of the two more fundamental types of disorder mentioned above.

### C. New Directions

There are a number of follow-up studies that may illuminate several of the many areas which the present work has managed only to stumble over or timidly grope into:

1) Electron Nuclear Double Resonance (ENDOR) experiments would be of tremendous help in understanding the connections between the broad EPR resonance and the H bonded in the network of a-Si(H), possibly clarifying the existence of the hopping proton centers proposed here.

2) A detailed analysis of the nonexponential spin-lattice relaxation phenomena may yield further insight into the relaxation mechanism.

3) The frequency dependence of the spin-lattice relaxation should be investigated (this would, for instance, address the question of whether the theory of Movaghar and Schweitzer (115) is correct).

4) Lower temperature EPR work (say to 4.2 K) should help in understanding the origins of the broad line.

5) A study of the temperature dependence of the electronic spin-lattice relaxation time of the dangling bond resonance should be undertaken, in conjunction with a lineshape study as a function of H concentration.

6) The author had originally intended to perform light induced EPR experiments (with variable wavelength light), discussed in the introduction, on a series of samples of RS a-Si(H); the initial success of the NMR experiments reordered his priorities, somewhat. However, it still appears that this kind of probe would provide a very direct means of investigating carrier recombination phenomena. As will be recalled, this is probably the single most important limiting factor to the photovoltaic performance of a-Si(H). These experiments should be undertaken soon.

7) Finally, another systematic study in which the sputtering parameters are varied in a controlled fashion (particularly the DC bias) should be initiated; NMR measurements should then be made to determine a possible

correlation of any of the parameters with the incidence of the HC defects in the material. In this connection, the FFT transform spectrum of the 14% H sample is anomalous (it may be recalled that this is the sample which is inferred to have incorporated D along with H on the basis that its broad EPR is similar to those samples that had been purposefully prepared that way). The FFT spectrum has very little Gaussian component and is mostly Lorentzian. That it probably has considerable D incorporation confuses the issue, somewhat: is it possible that D will preferentially occupy the cluster sites at the expense of the H occupation of them? Or, could it be that D somehow affects the self-bias on the plasma growth surface in such a way that the deposition process is somehow gentler and clusters do not form? It is also possible, since this sample was not prepared at the same time as the rest of the series, that conditions in the sputtering chamber itself were somehow unusual. An understanding of why the FFT spectrum of this sample has an anomalously low clustered hydrogen content could very well open the door to sample preparation techniques that avoid this inhomogeneity.

It would be difficult to overemphasize the importance of characterizing samples with every conceivable tool in addition to magnetic resonance spectroscopies. It is particularly important to undertake transport property measurements in conjunction with the other characterizations; this should be done with any of the studies proposed above.

In conclusion, it is the author's hope that the present work, with its considerable failings, has served at least to outline the problem, to ask some of the right questions, and to perhaps even provide an answer or two.

## VI. LITERATURE CITED

- A. Experimental Works: Sample Preparation, General Structural Determinations and Transport Measurements of Amorphous Semiconductors (Mostly Group IV)
1. Sample preparation, infrared absorption, x-ray diffraction, Photoluminescence, Conductivity, Photoconductivity, Field Effect, Optical Absorption, and sundry methods of determining the electronic and nuclear structure of amorphous semiconductors.
    1. R. C. Chittick, J. H. Alexander, and H. F. Sterling, J. Electrochem. Soc. 116, 77 (1969).
    2. M. H. Brodsky, R. S. Title, K. Weiser, and G. D. Pettit, Phys. Rev. B 1, 2632 (1970).
    3. J. A. Sauvage and C. J. Mogab, J. Non-Cryst. Solids B-10, 607 (1972).
    4. P. G. Le Comber, A. Madan, and W. E. Spear, J. Non-Cryst. Solids 11, 219 (1972).
    5. M. H. Brodsky, D. Kaplan, and J. F. Ziegler, Appl. Phys. Lett. 21, 305 (1972).
    6. John E. Fischer and Terence M. Donovan, J. Non-Cryst. Solids B-10, 202 (1972).
    - 7a. R. J. Loveland, W. E. Spear, and A. Al-Sharbaty, J. Non-Cryst. Solids 13, 55 (1973).
    - 7b. K. Kaplan, D. Lepine, Y. Petroff, and P. Thirry, Phys. Rev. Lett. 35, 1376, (1975).
    - 8a. W. Paul, A. J. Lewis, G.A.D. Connel, and T. D. Moustakas, Solid State Commun. 20, 969 (1976).
    - 8b. A. Madan, P. G. Le Comber, and W. E. Spear, J. Non-Cryst. Solids 20, 239 (1976).
    9. W. A. Langford, H. P. Trautvetter, J. F. Ziegler, and J. Keller, Appl. Phys. Lett. 28, 566 (1976).
    10. Adam J. Lewis, Phys. Rev. B 14, 658 (1976).
    11. G.A.N. Connell and J. R. Pawlik, Phys. Rev. B 13, 787 (1976).

12. J. Chevallier, H. Wieder, A. Onton, and C. R. Guarnieri, *Solid State Commun.* 24, 867 (1977).
13. M. H. Brodsky, Manuel Cardona, and J. J. Cuomo, *Phys. Rev. B* 16, 3556 (1977).
14. T. D. Moustakas and William Paul, *Phys. Rev. B* 16, 1564 (1977).
15. D. L. Staebler and C. R. Wronski, *Appl. Phys. Lett.* 31, 292 (1977).
16. T. D. Moustakas, D. A. Anderson, and William Paul, *Solid State Commun.* 23, 155 (1977).
17. M. H. Brodsky, M. A. Frisch, J. F. Ziegler, and W. A. Lanford, *Appl. Phys. Lett.* 30, 561 (1977).
18. D. Kaplan, N. Sol, G. Velsaco, and P. A. Thomas, *Appl. Phys. Lett.* 33, 440 (1978).
19. E. C. Freeman and William Paul, *Phys. Rev. B* 18, 4288 (1978).
20. M. A. Paesler, D. A. Anderson, E. C. Freeman, G. Moddel, and William Paul, *Phys. Rev. Lett.* 41, 1492 (1978).
21. M. H. Brodsky and D. Kaplan, *J. Non-Cryst. Solids* 32, 431 (1979).
22. H. J. Stein, *Phys. Rev. Lett.* 43, 1030 (1979).
23. H. J. Stein and P. S. Peercy, *Appl. Phys. Lett.* 34, 604 (1979).
24. D. Ewald, M. Milleville, and G. Weiser, *Philos. Mag. B* 40, 291 (1979).
25. A. Madan, S. R. Ovshinsky, and E. Benn, *Philos. Mag. B* 40 259 (1979).
26. D. E. Carlson, C. W. Magee, and A. R. Triano, *J. Electrochem. Soc.* 126, 688 (1979).
27. J. C. Knights, B. Lucovsky, and R. J. Nemanich, *J. Non-Cryst. Solids* 32, 393 (1979).
28. R. H. Williams, R. R. Varma, W. E. Spear, and P. G. Le Comber, *J. Phys. C* 12, L209 (1979).
29. D. A. Anderson, G. Moddel, R. W. Collins, and W. Paul, *Solid State Commun.* 31, 677 (1979).
30. B. von Roedern, L. Ley, M. Cardona, and F. W. Smith, *Philos. Mag. B* 40, 433 (1979).



31. J. Perrin, I. Solomon, A. Bourdon, J. Fontenille, and E. Ligeon, *Thin Solid Films* 62, 327 (1979).
32. A. K. Ghosh, T. McMahon, E. Rock, and H. Wiesmann, *J. Appl. Phys.* 50, 3407 (1979).
33. J. A. McMillan and E. M. Peterson, *J. Appl. Phys.* 50, 5238 (1979).
34. J. C. Knights and R. A. Lujan, *Appl. Phys. Lett.* 35, 244 (1979).
- 35a. F. R. Jeffrey, H. R. Shanks, and G. C. Danielson, *J. Appl. Phys.* 50, 7034 (1979).
- 35b. F. R. Jeffrey, The Effects of Hydrogen Content on Reactively Sputtered Amorphous Silicon Films. Unpublished Ph.D. thesis, Library, Iowa State University, Ames, Iowa, 1979.
36. G. Lucovsky, R. J. Nemanich, and J. C. Knights, *Phys. Rev. B* 19, 2064 (1979).
37. A. J. Leadbetter, A.A.M. Rashid, R. M. Richardson, A. F. Wright, and J. C. Knights, *Solid State Commun.* 33, 973 (1980).
38. Zimmer S. Jan, Richard H. Bube, and John C. Knights, *J. Appl. Phys.* 51, 3278 (1980).
39. D. L. Staebler and C. R. Wronski, *J. Appl. Phys.* 51, 3262 (1980).
40. J. C. Bruyere, A. Deneuville, A. Mini, J. Fontenille, and R. Danielou, *J. Appl. Phys.* 51, 2199 (1980).
41. W. Fuhs and M. Milleville, *Phys. Status Solidi* B98, k29 (1980).
42. B. von Roedern and G. Moddel, *Solid State Commun.* 35, 467 (1980).
43. Franklin H. Cocks, Alan J. Scharman, Phillip L. Jones, and Stuart F. Cogan, *Appl. Phys. Lett.* 36, 909 (1980).
- 44a. G. Muller, F. Demond, S. Kalbitzer, H. Damjantschitsch, H. Mannsperger, W. E. Spear, P. G. Le Comber, and R. A. Gibson, *Philos. Mag. B* 41, 571 (1980).
- 44b. U. Voget-Grote, W. Kummerle, R. Fischer, and J. Stuke, *Philos. Mag. B* 41, 127 (1980).
45. E. E. Haller, B. Joos, and L. M. Falicov, *Phys. Rev. B* 21, 4729 (1980).
46. R. Messier, S. V. Krishnaswamy, L. R. Gilbert, and P. Swab, *J. Appl. Phys.* 51, 1611 (1980).

- 47a. H. Shanks, C. J. Fang, L. Ley, M. Cardona, F. J. Demond, and S. Kalbitzer, *Phys. Status Solidi B*: 100, 43 (1980).
- 47b. H. R. Shanks and L. Ley, *J. Appl. Phys.* 52, 811 (1981).
- 48. A. Madan, S. R. Ovshinsky, W. Czubytl, and M. Shur, *J. Electr. Mat.* 9, 385 (1980).
- 49. Hideki Matsumura, Yoshinobu Nakagome, and Seijiro Furukawa, *Appl. Phys. Lett.* 36, 439 (1980).
- 50. C. J. Fang, L. Ley, H. R. Shanks, K. J. Gruntz, and M. Cardona, *Phys. Rev. B* 22, 6140 (1980).
- 51. P. Hey, N. Raouf, D. C. Booth, and B. O. Seraphin, *AIP Conf. Proc.* No. 73, p. 58 (American Institute of Physics, New York, 1981).

## 2. Magnetic Resonance Spectroscopies applied to amorphous semiconductors

### a. Electron spin resonance works

- 52. M. H. Brodsky and R. S. Title, *Phys. Rev. Lett.* 23, 581 (1969).
- 53. S. Hasegawa and S. Yazaki, *Solid State Commun.* 23, 41 (1977).
- 54. P. A. Thomas, M. H. Brodsky, D. Kaplan, D. Lepine, *Phys. Rev. B* 18, 3059 (1978).
- 55. S. Hasegawa, T. Kasajima, and T. Shimizu, *Solid State Commun.* 29, 13 (1979).
- 56. R. S. Title, M. H. Brodsky, and J. J. Cuomo, in *Proc. of the Int. Conf. on Amorphous and Liquid Semiconductors*, ed. by W. E. Spear (G. G. Stevenson, Dundee, 1977) p. 424.
- 57. J. C. Knights, in *Proc. of the Int. Conf. on Amorphous and Liquid Semiconductors*, ed. by W. E. Spear (G. G. Stevenson, Dundee, 1977) p. 433.
- 58. J. R. Pawlik and W. Paul in *Proc. of the Int. Conf. on Amorphous and Liquid Semiconductors*, ed. by W. E. Spear (G. G. Stevenson, Dundee, 1977) p. 437.
- 59a. T. Yonehara, T. Saitoh, H. Kwarada, T. Hirata, M. Kakumu, and I. Ohdomari, *Phys. Lett.* 78A, 192 (1980).
- 59b. A. P. Malozemoff and S. C. Hart, *Phys. Rev. B* 21, 29 (1980).

60. S. G. Bishop and P. C. Taylor, in Proc. of DOE Program Review of Photovoltaics Subcontractors, unpublished (Denver, 1981).

b. Light induced electron spin resonance experiments

61. Daniel J. Lepine, Phys. Rev. B6, 436 (1972).
62. I. Solomon, Solid State Commun. 20, 215 (1976).
- 63a. J. C. Knights, D. K. Biegelsen, and I. Solomon, Solid State Commun. 22, 133 (1977).
- 63b. I. Solomon, D. K. Biegelsen, and J. C. Knights, Solid State Commun. 22, 505 (1977).
64. David K. Biegelsen and John C. Knights, in Int. Conf. on Liquid and Amorphous Semiconductors, ed. by W. E. Spear (G. G. Stevenson, Dundee, 1977) p. 429.
65. A. Friedrich and D. Kaplan, J. Electr. Mat. 8, 79 (1979).
66. G. Mendz, D. J. Miller, and D. Haneman, Phys. Rev. B 20, 5246 (1979).
67. E. A. Schiff, AIP Conference Proceedings No. 73 (American Institute of Physics, New York, 1981) p. 233.

c. Nuclear Magnetic Resonance works

68. J. A. Reimer, R. W. Vaughan, and J. C. Knights, Phys. Rev. Lett. 44, 193 (1980).
69. W. E. Carlos and P. C. Taylor, Phys. Rev. Lett. 45, 358 (1980).
- 70a. M. E. Lowry, R. G. Barnes, D. R. Torgeson, and F. R. Jeffrey, in Nuclear and Electron Resonance Spectroscopies Applied to Materials Science, Kaufmann and Shenoy, editors (Elsevier North Holland, Inc., New York, 1981).
- 70b. Jeffrey A. Reimer, Robert W. Vaughan, and John C. Knights, in Nuclear and Electron Resonance Spectroscopies Applied to Materials Science, Kaufmann and Shenoy, editors (Elsevier North Holland, Inc., New York, 1981).
- 70c. F. R. Jeffrey, P. De Bois Morphy, and B. C. Gerstein, Phys. Rev. B 23, 2099 (1981).
71. M. Lowry, F. R. Jeffrey, R. G. Barnes, and D. R. Torgeson, Solid State Commun. 38, 113 (1981).

72. F. R. Jeffrey and M. E. Lowry, J. Appl. Phys. 52, 5529 (1981).
73. W. E. Carlos, P. C. Taylor, S. Oguz, and W. Paul, in AIP Conference Proceedings No. 73 (American Institute of Physics, New York, 1981) p. 67.
74. J. A. Reimer and J. C. Knights, in AIP Conference Proceedings No. 73 (American Institute of Physics, New York, 1981) p. 78.
75. F. R. Jeffrey, M. E. Lowry, M.L.S. Garcia, R. G. Barnes, and D. R. Torgeson, in AIP Conference Proceedings No. 73 (American Institute of Physics, New York, 1981) p. 83.
76. Jeffrey A. Reimer, Robert W. Vaughan, and John C. Knights, Solid State Commun. 37, 161 (1981).
77. Jeffrey A. Reimer, Robert W. Vaughan, and John C. Knights, Phys. Rev. B 24, 3360 (1981).
78. Jeffrey A. Reimer, in 9th Int. Conf. on Liquid and Amorphous Semiconductors, Grenoble, France (published as a supplement to J. Phys. (Paris) 42, 1981).
79. H. R. Shanks, F. R. Jeffrey, and M. E. Lowry, in 9th Int. Conf. on Liquid and Amorphous Semiconductors, Grenoble, France (published as a supplement to J. Phys. (Paris) 42, 1981).
- 80a. W. E. Carlos and P. C. Taylor, in 9th Int. Conf. on Liquid and Amorphous Semiconductors, Grenoble, France (published as a supplement to J. Phys. (Paris) 42, 1981).
- 80b. J. A. Reimer, P. Dubois Murphy, B. C. Gerstein, and J. C. Knights, J. Chem. Phys. 74, 1501 (1981).
81. Jeffrey A. Reimer, Robert W. Vaughan, John C. Knights, and Rene A. Lujan, submitted to Appl. Phys. Lett. (1981).
82. Jeffrey A. Reimer, Robert W. Vaughan, and John C. Knights, Phys. Rev. B 23, 2567 (1981).
83. W. E. Carlos and P. C. Taylor, Phys. Rev. B 25, 1435 (1982).

#### B. Amorphous Materials: Models, Theory, and Philosophy

84. P. W. Anderson, Phys. Rev. 109, 1492 (1958).
85. Morrel H. Cohen, J. Non-Cryst. Solids 2, 432 (1970).
86. P. W. Anderson, Phys. Rev. Lett. 34, 953 (1975).

87. R. A. Street and N. F. Mott, Phys. Rev. Lett. 35, 1293 (1975).
88. N. F. Mott, E. A. Davis, and R. A. Street, Philos. Mag. 32, 961 (1975).
- 89a. D. Adler and E. J. Yoffa, Phys. Rev. Lett. 36, 1197 (1976).
- 89b. Marc Kastner, David Adler, and H. Fritzsche, Phys. Rev. Lett. 37, 1504 (1976).
90. Stephen J. Hudgens, Phys. Rev. B 14, 1547 (1976).
91. N. F. Mott, Philos. Mag. 36, 413 (1977).
92. B. Movaghar and L. Schweitzer, Phys. Status Solidi B: 80, 491 (1977).
93. R. Fisch and D. C. Licciardello, Phys. Rev. Lett. 41, 889 (1978).
94. David Adler, Phys. Rev. Lett. 41, 1755 (1978).
95. S. R. Elliott, Philos. Mag. B 38, 325 (1978).
96. B. Movaghar, L. Schweitzer, and H. Overhof, Philos. Mag. B 37, 683 (1978).
97. D. Kaplan, I. Solomon, and N. F. Mott, J. Phys. (Paris) Lett. 39, L51 (1978).
98. R. A. Street, Phys. Rev. B 17, 3984 (1978).
99. R. Bachus, B. Movaghar, L. Schweitzer, and U. Voget-Grote, Philos. Mag. B 39, 27 (1979).
100. S. R. Elliot, Philos. Mag. B 39, 349 (1979).
101. J. D. Joannopoulos, J. Non-Cryst. Solids 32, 241 (1979).
102. G. A. Baraff, E. O. Kane, and M. Schluter, Phys. Rev. Lett. 43, 956 (1979).
103. Stanford R. Ovshinsky, J. Non-Cryst. Solids 32, 17 (1979).
104. M. Pollak, M. L. Knotek, J. Non-Cryst. Solids 32, 141 (1979).
105. Douglas C. Allan and J. D. Joannopoulos, Phys. Rev. Lett. 44, 43 (1980).
106. K. H. Johnson, H. J. Kolari, J. P. de Neufville, and D. L. Morel, Phys. Rev. B 21, 643 (1980).

- 107. G. P. Johari, *Philos. Mag. B* 41, 41 (1980).
- 108. J. H. Davies, *Philos. Mag B* 41, 373 (1980).
- 109. William Paul, *Solid State Commun.* 34, 283 (1980).
- 110a. W. Y. Ching, Daniel J. Lam, Chun C. Lin, *Phys. Rev. B* 21, 2378 (1980).
- 110b. Lester Guttman, W. Y. Ching, and Jagamath Rath, *Phys. Rev. Lett.* 44, 1513 (1990).
- 111. B. Movaghar, B. Reis, and L. Schweitzer, *Philos. Mag. B* 41, 141 (1980).
- 112. P. John, I. M. Odeh, M.J.K. Thomas, M. J. Tricker, and J.I.B. Wilson, *Phys. Status Solidi B*: 103, K141 (1981).
- 113. M. I. Klinger and V. G. Karpov, *Solid State Commun.* 37, 975 (1981).
- 114. B. Movaghar and L. Schweitzer, in *AIP Proceedings No. 73*, (American Institute of Physics, New York, 1981) p. 73.
- 115. B. Movaghar and L. Schweitzer, *J. Phys. C*: 14, 5185 (1981).
- 116. Mark S. Conradi and R. E. Norberg, *Phys. Rev. B* 24, 2285 (1981).

C. Communications Dealing with or Relating to Devices  
Made from Amorphous Semiconductors

- 117a. D. M. Chapin, C. S. Fuller, and G. L. Pearson, *J. Appl. Phys.* 25, 676 (1954).
- 117b. S. R. Ovshinsky, *Phys. Rev. Lett.* 21, 1450 (1968).
- 118a. J. Lindmeyer and C. Y. Wrigley, National Science Foundation report no. 43090, National Science Foundation, Washington, D.C. (1974)
- 118b. W. E. Spear and P. G. Le Comber, *Solid State Commun.* 17, 1193 (1975).
- 119. W. E. Spear, P. G. Le Comber, S. Kinmond, and M. H. Brodsky, *Appl. Phys. Lett.* 28, 105 (1976).
- 120. D. E. Carlson and C. R. Wronski, *Appl. Phys. Lett.* 28, 671 (1976).
- 121a. C. R. Wronski, D. E. Carlson, and R. E. Daniel, *Appl. Phys. Lett.* 29, 602 (1976).

- 121b. Stanley W. Angrist, Direct Energy Conversion, 3rd edition (Allyn and Bacon, Boston, 1976).
- 122. D. E. Carlson, J. I. Pankove, C. R. Wronski and P. J. Zanzucchi, Thin Solid Films 45, 43 (1977).
- 123. M. Taniguchi, M. Hirose, and Y. Osaka, J. Cryst. Growth 45, 126 (1978).
- 124. J. O. White, T. R. Kirst, and J. Tauc, Appl. Optics 17, 2427 (1978).
- 125. S. R. Ovshinsky and Arun Madan, Nature 276, 482 (1978).
- 126. David L. Staebler, J. Appl. Phys. 50, 3648 (1979).
- 127. K. W. Boer, J. Appl. Phys. 50, 5356 (1979).
- 128. Yoshihiro Hamakawa, Surf. Sci. 86, 444 (1979).
- 129. Joseph J. Loferski, Surf. Sci. 86, 424 (1979).
- 130. Henry Ehrenreich and John H. Martin, Phys. Today, Sept. (1979).
- 131. Y. Imamura, S. Ataka, Y. Takasaki, C. Kusano, T. Hirai, and E. Maruyama, Appl. Phys. Lett. 35, 349 (1979).
- 132. K. Graff and H. Fischer, Topics in Appl. Phys. 31, 173 (1978).
- 133. D. A. Anderson, G. Moddel, and William Paul, J. Electr. Mat. 9, 141 (1980).
- 134. J. C. Knights, in AIP Conf. Proc. No. 31, (American Institute of Physics, New York, 1976) p. 296.
- 135. R. A. Gibson, P. G. Le Comber, and W. E. Spear, Appl. Phys. 21, 307 (1980).
- 136. D. H. Auston, P. Lavallard, N. Sol, and D. Kaplan, Appl. Phys. Lett. 36, 66 (1980).
- 137. R. A. Lemons, Appl. Phys. Lett. 36, 919 (1980).
- 138. Hiroshi Hayama and Masakiyo Matsumura, Appl. Phys. Lett. 36, 754 (1980).
- 139a. L. A. Coldren, M. A. Bosch, and J. A. Rentschler, Appl. Phys. Lett. 36 688 (1980).
- 139b. R. N. Hall, General Electric Technical Information Bulletin no. 80CRD274 (General Electric Corporate Research and Development, Schenectady, New York, 1981).

- 139c. F. R. Jeffrey, Solar Energy Research Institute, Golden, Colorado private communication (1982).

D. Review Articles and Books Dealing  
with Amorphous Semiconductors

140. Aleksandr Ivanovich Gubanov, Quantum Electron Theory of Amorphous Conductors, transl. from the Russian by A. Tybulewicz (Consultants Bureau, New York, 1965).
141. David Adler, CRC Critical Reviews 2, 317 (1971).
142. M. H. Brodsky, J. Vac. Sci. Technol. 8, 125 (1971).
143. A. K. Jonscher, J. Vac. Sci. Technol. 8, 135 (1971).
144. Robert M. Hill, Thin Solid Films, 51, 133 (1978).
145. R. M. Hill and A. K. Jonscher, J. Non-Cryst. Solids 32, 53 (1979).
146. S. R. Elliott, Nature 277, 85 (1979).
147. J. M. Ziman, Models of Disorder (Cambridge University Press, Cambridge, 1979).
148. N. F. Mott and E. A. Davis, Electronic Processes in non-crystalline Materials, 2nd ed. (Clarendon Press, Oxford, 1979).
149. Topics in Applied Physics Vol. 36, Amorphous Semiconductors, edited by M. H. Brodsky (Springer-Verlag, New York, 1979).
150. Yoshio Waseda, The Structure of Non-Crystalline Materials: Liquids and Amorphous Solids (McGraw-Hill, New York, 1980).

E. Fundamental Solid State Physics References

151. J. M. Ziman, Principles of the Theory of Solids (Cambridge University Press, Cambridge, 1972).
152. Neil W. Ashcroft and N. David Mermin, Solid State Physics (Holt, Rinehart, and Winston, New York, 1976).
153. Charles Kittel, Introduction to Solid State Physics, 4th ed. (John Wiley & Sons, Inc., New York, 1971).



154. L. M. Falicov, Group Theory and Its Physical Applications (University of Chicago Press, Chicago, 1966).

#### F. References Related to the Theory of Magnetic Resonance

155. James D. Macomber, The Dynamics of Spectroscopic Transitions (John Wiley and Sons, New York, 1976).
156. Charles P. Slichter, Principles of Magnetic Resonance, 2nd edition (Springer-Verlag, New York, 1978).
157. Richard P. Feynman, Statistical Mechanics (W. A. Benjamin Inc., Reading, Mass., 1972).
158. Maurice Goldman, Spin Temperature and Nuclear Magnetic Resonance in Solids (Oxford University Press, New York, 1970).
159. G. E. Pake and T. L. Estle, The Physical Principles of Electron Paramagnetic Resonance (W. A. Benjamin Inc., Reading, Mass., 1973).
160. Eugene Merzbacher, Quantum Mechanics, 2nd edition (John Wiley and Sons, Inc., New York, 1970).
161. L. D. Landau and E. M. Lifshitz, Quantum Mechanics: Non-relativistic Theory (Pergamon Press, New York, 1976).
162. Thomas C. Farrar and Edwin D. Becker, Pulse and Fourier Transform NMR (Academic Press, New York, 1971).
163. A. Abragam, The Principles of Nuclear Magnetism (Oxford University Press, New York, 1961).
164. Melvin Schwartz, Principles of Electrodynamics (McGraw-Hill Book Co., New York, 1972).
165. Ryogo Kubo, Statistical Mechanics (North-Holland, New York, 1978).

#### G. Magnetic Resonance Experimental Methods References

166. Charles P. Poole Jr., Electron Spin Resonance: A Comprehensive Treatise on Experimental Techniques (Interscience Publishers, New York, 1967).
167. M. L. Martin, G. J. Martin, and J.-J. Delpuech, Practical NMR Spectroscopy (Heyden, Philadelphia, 1980).

168. John L. Conway and R. M. Cotts, Rev. Sci. Instrum., 48, 656 (1977).
169. T. J. Lowe and C. E. Tarr, J. Sci. Instrum. 1, 320 (1968).
170. D. J. Adduci, P. A. Hornung, and D. R. Torgeson, Rev. Sci. Instrum., 47, 1503 (1976).
171. R. G. LeCander, BIONIC, unpublished computer program, available from D. R. Torgeson, Physics Department Iowa State University, Ames, IA (1980).
172. D. J. Adduci, P. A. Hornung, and D. R. Torgeson, Rev. Sci. Instrum. 48, 661 (1977).
173. D. V. Jensen, Ames Lab Virtual Interactive Network (ALVIN), unpublished computer program, available through the Instrumentation Group, Ames Laboratory of USDOE, Ames, IA (1978).
174. Paul D. Murphy, Peak 15 (a multipeak fitting routine), available through D. V. Jensen, Instrumentation Group, Ames Laboratory of USDOE, Ames, IA (1979).
175. Paul D. Murphy, Fourier Data Analysis Program: FA1, Ames Laboratory document # IS-4769 UC-32, Ames Laboratory USDOE, Ames, IA (1981).

#### H. Miscellaneous Magnetic Resonance and Amorphous Materials References

176. Charles W. Myles, C. Ebner, and Peter A. Fedders, Phys. Rev. B 14, 1 (1976).
177. W. E. Blumberg, Phys. Rev. 119, 79 (1960).
178. N. Bloembergen, Physica XV, 386 (1949).
179. M. E. Lowry with R. J. Schoenberger, FITMAN: A generalized fitting and graphing routine, unpublished computer program, available through D. R. Torgeson, Physics Dept. Iowa State University, Ames, IA (1982).
180. G. E. Jellison Jr. and S. G. Bishop, Phys. Rev. Lett. 40, 1204 (1978).
181. H. E. Rorschach Jr., Physica 30, 38 (1964).
182. J. C. Gourdon, P. Fretier, and J. Pescia, J. Physique Lett. 42, L-21 (1981).

183. D. K. Paul and S. S. Mitra, Phys. Rev. Lett. 31, 1000 (1973).
184. A. Lewis, Phys. Rev. Lett. 29, 1555 (1972).
185. S. Hasegawa and S. Yazaki, Thin Solid Films, 55, 15 (1978).
186. M. L. Knotek, in AIP Conf. Proc. No. 31, ed. G. Lucovsky and F. L. Galeener (American Institute of Physics, New York, 1976).
187. E. Holzenkampfer, F. -W. Richter, J. Stuke, and U. Voget-Grote, J. Non-Cryst. Solids 32, 327 (1979).
188. M. Punkkinen and S. Clough, J. Phys. C: 7, 3403 (1974).
189. S. Clough and B. J. Mulady, Phys. Rev. Lett. 30, 161 (1973).
190. S. Clough, J. R. Hill, and T. Hobson, Phys. Rev. Lett. 33, 1257 (1974).
191. S. Clough and J. R. Hill, J. Phys. C: 8, 2274 (1975).
192. S. Clough and T. Hobson, J. Phys. C: 7, 3387 (1974).
193. A. P. Malozemoff and S. C. Hart, Phys. Rev. B 21, 29 (1980).
194. J. L. Vossen and W. Kern ed., Thin Film Processes, (Academic Press, New York, 1978).
195. Brian Chapman, Sputtering and Plasma Etching, (Wiley-Interscience, New York, 1980).

## VII. ACKNOWLEDGEMENTS

Any success that this work has enjoyed is due in no small part to the generous assistance I have received from many people.

By his ready accessability, and rich sense of humor, Professor Richard G. Barnes has created a vigorous, yet relaxed, laboratory atmosphere in which the never ceasing exchange of ideas (scientific and otherwise) has both provided the motivation to press on and the seeds of thought for much of "the physics" presented here. The breadth and depth of his familiarity with the physics literature has greatly eased the burden of pursuing this research in a (hopefully) scholarly fashion. Professor Barnes has not only been my mentor in matters of experimental physics; he has also patiently taught me the art of scientific writing, of which the inadequacies evident here are completely mine.

David R. Torgeson has taught me more about laboratory electronics and the fundamental physics essential to the experimental realization of magnetic resonance investigations than would have been possible with the attendance of any number of formal classes, and he has done so with much exhuberance and characteristic Norwegian "humor" (he will understand the quotes).

Dr. Frank R. Jeffrey introduced me to the reactive sputtering technique, the many mysteries of amorphous silicon-hydrogen alloys, and the joys of racing an M-scow sailboat. His expert preparation of the samples for this study and help in some of the analysis of the FFT NMR data are greatly acknowledged.

Dr. Maria L.S. Garcia has contributed generously of her time in the many measurements of NMR relaxation times and also helped in shaping the interpretation of the data by vigorously playing the "devil's advocate" in discussion. Her friendship during this collaboration has been a respite from the sometime drudgery of a prolonged measurement campaign in which work would often proceed into the "wee hours" on an overlapping shift basis.

Howard R. Shanks' involvement with a-Si(H) research over the years has been of benefit to me by virtue of his willingness to share many insights into the material structure and properties; our collaboration and that of F.R.J. (above) has made a significant portion of this work possible.

Professor F. Borsa has helped me to understand relaxation phenomena in general and been a willing critic of some of my subsequent ideas with regard to a-Si(H).

Professor B. N. Harmon has also given freely of his time in discussion of some of the theoretical aspects of my earlier interpretations of the data.

James D. Losse has given generously of his friendship and of his time in the solution of mathematical physics problems associated with this work.

The patience and understanding of my wife, Deb, has been a comfort throughout the course of this research; her performance as M-scow racing crew and "sailing buddy" has particularly helped buoy my spirits in the provision of much needed diversion.

To my Father I am grateful for introducing me to my avocation--sailing.

Finally, the expert and timely services of my typist Ms. Maxine Bogue are gratefully recognized.

## VIII. APPENDICES

## A. Thin Film Deposition Techniques for Amorphous Silicon-hydrogen Alloys [a-Si(H)]

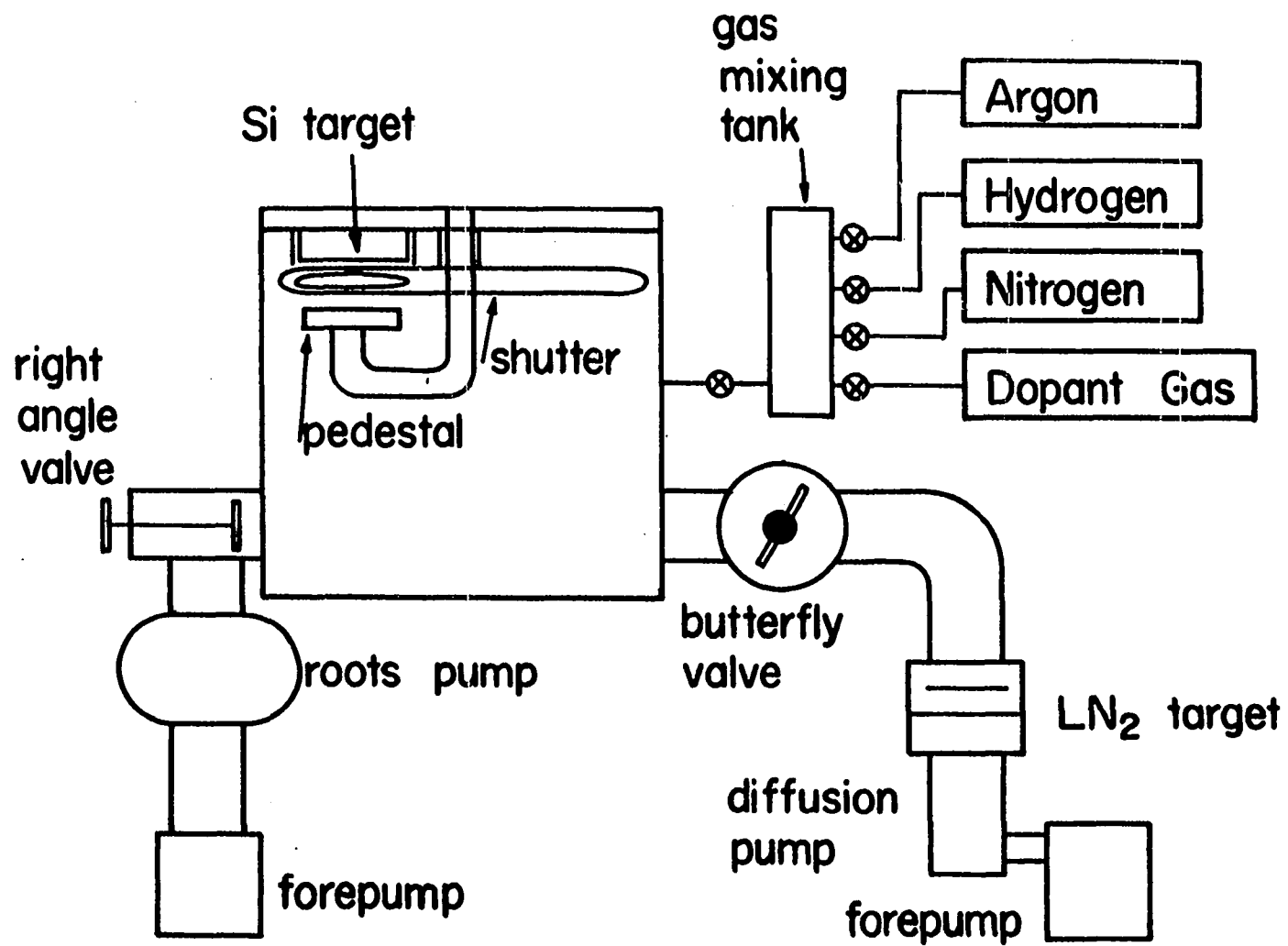
This section is meant to serve as a brief introduction to the many currently employed methods of producing a-Si(H) alloys. There are several excellent references (194, 195) that treat thin film processes in general. Here, the reactive sputtering method will be dealt with first and most extensively, since the samples used in this study are a product of this method.

1. Reactive Sputtering (RS)

Although this was not the first method of preparation for a-Si(H) thin films, it may be the most versatile. This method utilizes argon as the major "sputtering vehicle." The principles of operation for this sputtering system (see Fig. 29) may be grasped by outlining the sample preparation steps:

a. The first step is usually one of cleaning the chamber, target, and substrate. This is accomplished by "sputter etching" and high vacuum degassing. The sputter etching step is completed by evacuating the chamber to approximately  $10^{-3}$  torr and allowing a steady state injection of Ar gas into the chamber in the presence of a high power rf excitation ( $\sim 13$  MHz in this case). This rf excitation is capacitively coupled through the target housing and substrate holder and is sufficient to ionize the Ar which then forms a very energetic plasma. This plasma then etches everything it comes into contact with by literally scouring the surfaces with a continual pelting of high energy ions. It should be pointed out that the etching

Fig. 29. A schematic diagram of the rf capacitively coupled sputtering system used to prepare the relatively sputtered (RS) a-Si(H) and a-Si(H,D) samples for this study. See text for details of the systems operation





takes place on surfaces that maintain a position bias. By changing the direction of the bias, one may then sputter etch clean the target or the substrats. After the sputter etch cycle, the chamber is allowed to degass at approximately  $10^{-8}$  torr.

b. After sufficient degassing the chamber pressure is brought up to  $10^{-3}$  torr by steady state injection of Ar, once again in the presence of the rf field. In the deposition mode, the substrate is held at ground, producing a large DC bias. The Ar plasma etches the high purity polycrystalline target, thereby introducing Si into the plasma. The applied DC bias then energetically favors the deposition of Si unto the substrate (it must be noted that some Ar is also trapped in the film growing on the substrate--see Appendix B for details of the Ar contamination--the concentration is relatively small due to the unreactive nature of the Ar ion).

c. There are several variable parameters of sample preparation using this technique. Most importantly,  $H_2$  gas is leaked into the chamber in controlled variable amounts. This feature allows one to study the material as a function of H concentration only. As discovered by Jeffrey et al. (35a), and discussed in the introduction, the rf power incident into the plasma greatly effects the concentration of undesirable  $SiH_2$  centers in the resulting film. The substrate may be externally heated with this arrangement, however the samples produced for this study were deposited on unheated substrates. Dopant gases (for the production of either n or p type material) are also available for injection into the sputtering system. Finally, several aspects of the chamber geometry and other parameters effect the deposition rate; ref. 35b should be consulted for details.

d. Table 1 should be consulted for details of the sputtering parameters for a given sample.

## 2. Glow Discharge (GD)

This method involves the decomposition of Silane,  $\text{SiH}_4$ , into a Si-H plasma often in the presence of a noble gas. The excitation is usually an rf discharge. The s-Si(H) film condenses from the plasma in a manner similar to the RS technique. However, the use of Silane as the Si source necessarily puts constraints upon the atomic ratio of incorporated H. More H may be added to the plasma with a resulting increase in H concentration in the deposited film; whereas, decreases in the H concentration are difficult to reliably achieve without altering some other independent parameter (e.g., the substrate temperature or amount of noble gas diluent). Typical H concentrations are 10-20%. Chittick et al. (1) were the first to produce a-Si(H) with this method using an inductively coupled rf chamber. Spear and Lecomber (118b) improved upon this technique, as did the Xerox group (134) with the modification of capacitive coupling of the rf which, of course, allowed for a DC bias to be applied.

## 3. Chemical Vapor Deposition (CVD)

This labels a rather broad class of deposition techniques which rely upon the "thermal cracking" of Silane to achieve the atomic constituents necessary for the a-Si(H) deposition. Reference 149 should be consulted as a guide to this technique. One striking feature of films prepared using this technique is the low concentration of H (<1%) when monosilane (as opposed to the higher silanes) is used. As noted in the introduction,

the CVD processes have lately received much attention through the successes of the solar photovoltaic cells fabricated with material (139c).

#### 4. Evaporation

The evaporation of Si is usually achieved by use of an electron beam, in an ultra high vacuum chamber. Hydrogenation may be achieved by evaporation in the presence of H (32) or by post deposition exposure to an H plasma (18). As mentioned in the introduction, this method, along with pure Si sputter deposition, have served to produce control samples that allowed investigators to observe independently the effects of H incorporation.

#### 5. Ion plating

This, as the name suggests, is an electrochemical process, and is included merely to demonstrate the breadth of preparation methods that yield a-Si(H) thin films. Reference 43 should be consulted for details.

#### B. Mass Spectroscopic Analysis of Several RS a-Si(H) Samples

The mass spectroscopic analyses are presented for two RS a-Si(H) samples and one RS a-Si(H,D) sample. Table 1 should be consulted for details of the sample preparation in each case.

Table 4. Spark source mass spectroscopic analysis for sample C52

00000 SPARK SOURCE MASS SPECTROMETRIC ANALYSIS 00000																DATE 10/21/82			
PERIODIC TABLE DISPLAY																REQUESTED BY: MARK LOWRY			
ANALYTICAL GROUP: III-WORK LABEL 392																FUND: 03222			
SAMPLE IDENTIFICATION: 51H-C52																			
MAJOR ELEMENTS: S1																			
IA	IIA	IIIA	IVA	VA	VIA	VIIA	VIII	IB	IIB	IIIB	IVB	VB	VIB	VIIIB	0				
LI	BE														NE				
	<.03														<.2				
HA	MG				VALUES ARE IN PPM ATOMIC						AL	SI	P	S	CL	AR			
200	30				REFERENCE IS S1 = 10000000						200		10	200	70	80000			
K	CA	SC	TI	V	CR	MN	FE	CO	NI	CU	ZN	GA	GE	AS	SE	KR			
80	300	<.8	4	<.0	<.2	<.4	<.00	<.7	<.2	10	300	<.0	<.9	<.3	<.2	<.2			
RB	SR	Y	ZR	NB	MO	TC	RU	RH	PD	AG	CD	IN	SN	SB	TE	XE			
<.4	<.8	<.1	<.8	<.4	<.2		<.1	<.3	<.7	1	<.6	<.1	<.0	<.2	<.02	<.2			
CS	BA		WF	TA	W	RE	OS	IR	PT	AU	HG	TL	PB	BI					
<.82	<.4		<.3	<.1	<.40	<.0	<.28	<.7	<.10		<.3	<.2	20	<.2					
FR	HA	ACTINIDES		TH															
	<.1			<.2															
			LA	CE	PR	ND	PM	SH	EU	GD	TO	DY	HO	ER	TM	LU			
			<.7	<.8	<.4	<.2		<.1	<.7	<.3	<.8	<.2	<.3	<.2	<.4	<.1			
SUMMARY DATA-NOTE THAT VALUES ARE ROUNDED TO 2 SIGNIFICANT DIGITS IN SUMMARY REGARDLESS OF PRECISION EXCEPT FOR 10 HIGHEST IMP.																			
TOTAL CONCENTRATION OF ELEMENTS IDENTIFIED = 110000																			
TOTAL CONCENTRATION OF ELEMENTS AS UPPER LIMIT = <100																			
CONCENTRATION OF ELEMENTS IDENTIFIED/UPPER LIMIT FOR GROUPS:																			
IA	IIA	IIIA	IVA	VA	VIA	VIIA	VIII	IB	IIB	IIIB	IVB	VB	VIB	VIIIB	0				
200	300		4.0												80000				
<.42	<1.2	<2.1	<3.8	<2.5	<.42	<.13	<.00	11	300	210	90.0	11000	4800	2100	<.2				
										<.86	<.04	<.59	<.26	<.18					
TEN HIGHEST IMPURITIES																			
				S 200	AL 200	HA 200	ZN 300	CA 300	P 2000	D 5000		N 10000		AR 80000					
ANALYST: <i>[Signature]</i>																			
REMARKS: PLATE # 2500B																			
<i>semiquantitative survey C, N, &amp; O are probably due to surface contamination. This report supersedes that dated 8/4/82 for this sample. Such error is assignment of Ca to Ar lines.</i>																			
PEOPLE INPUT: CLARENCE NESS HOURS: 6 CATHY BRUNSTING BOB CONZENIUS 1																			

Table 5. Spark source mass spectroscopic analysis for sample C51

0		1		2		3		4		5		6		7		8		9		10		11		12		13						
SPARK SOURCE MASS SPECTROMETRIC ANALYSIS 00000																																
PERIODIC TABLE DISPLAY																																
ANALYTICAL GROUP III-YORK LABEL 392																																
SAMPLE IDENTIFICATION: 5TH-C61																																
MAJOR ELEMENT: SI																																
DATE 102/19/82																																
REQUESTED BY: MARK LOWRY																																
FUND: 03222																																
IA	IIA	IIIA	IVA	VA	VIA	VIIA	VIII	IB	IIB	IIIB	IVB	VB	VIB	VIIIB	O																	
LI	BE														B	C	N	O	F	NE												
70	420000														10000	6000	3000	300	420													
VALUES ARE IN PPM ATOMIC REFERENCE IS SI = 1000000																																
80	CA	SC	Ti	V	CR	MN	FE	CO	NI	CU	ZN	GA	GE	AS	SE	BR	KR															
100	100	<.5	3.0	<.6	<1	<.3	<20	<.7	<2	80	18	.20	<.2	.3	<.7	10	5															
RB	SR	Y	ZR	MO	MO	TC	RU	RH	PD	AG	CD	IN	SN	SB	TE		HE															
<.2	<.2	<.2	<.2	<.2	<1	<1	<1	<.3	<.4	.91	<.2	<.07	.10	<.1	<.02	<.007	<.3															
CE	BA														HC	TL	PD	B1														
<.0	<.2														1.0	<.1	<.3	<.0														
FR	HA														U																	
	<.8														<.6																	
SUMMARY DATA-NOTE THAT VALUES ARE ROUNDED TO 2 SIGNIFICANT DIGITS IN SUMMARY REGARDLESS OF PRECISION-EXCEPT FOR 10 HIGHEST IMP.																																
TOTAL CONCENTRATION OF ELEMENTS IDENTIFIED = 27000																																
TOTAL CONCENTRATION OF ELEMENTS AS UPPER LIMIT = 210000																																
CONCENTRATION OF ELEMENTS IDENTIFIED/UPPER LIMIT FOR GROUPS :																																
IA	IIA	IIIA	IVA	VA	VIA	VIIA	VIII	IB	IIB	IIIB	IVB	VB	VIB	VIIIB	O																	
120	110	110	110	110	110	110	110	110	110	110	110	110	110	110	110	110	110	110	110	110	110	110	110	110	110	110	110	110				
<.19	<10000	<.85	<.01	<3.0	<6.0	<1.4	<64	51	18	<.24	<.075	<.13	<.70	<.0049	<23																	
TEN HIGHEST IMPURITIES																																
CU 80 K 80 NA 70 S 100 CA 100 F 300 O 3000 N 6000 AR 7000 C 10000																																
ANALYST : <i>[Signature]</i>																																
REMARKS : PLATE # 2500A																																
<i>Ammonia to be used for survey</i>																																
<i>C, N, 40 are probably due to</i>																																
<i>surface contamination.</i>																																
<i>This report prepared at that</i>																																
<i>date 2/4/82 due to error in</i>																																
<i>assignment of Ca to Ar line</i>																																
PEOPLE INPUT: CLARENCE HESS HOURS: 5																																
CATHY BRUNSTING																																
GDB CONZEMUS																																

0		1		2		3		4		5		6		7		8		9		10		11		12		13	
<p>***** SPARK SOURCE MASS SPECTROMETRIC ANALYSIS *****</p> <p>PERIODIC TABLE DISPLAY</p> <p>ANALYTICAL GROUP III-WORK LABEL 357</p> <p>SAMPLE IDENTIFICATION SIR-C-81</p> <p>MAJOR ELEMENTS SI</p>																											
<p>DATE 106/19/81</p> <p>REQUESTED BY: MARK LOVY</p> <p>FUNO: 03222</p>																											
IA	IIA	IIIA	IVA	VA	VIA	VIIA	VIII	IB	IIB	IIIB	IVB	VB	VIB	VIIIB	0												
LI <.06	RE <.06									B <1	C 3000	N N	O 300	F 40	NE <2												
<p>VALUES ARE IN PPM ATOMIC REFERENCE IS SI = 1000000</p>																											
NA 40	MG 30									AL 200	SI 200	P <20	S 30	CL 30	AR <600												
K <400	CA 100	SC <20	TI <20	V <30	CR <3	MN 5	FE 500	CU <5	NI 7	CO 30	ZN 13	GA <.9	GE <.4	AS 2	SE 21												
RB 52	SR 52	Y 5	ZR <1000	NB 5	MO <20	TC 5	HU 5	RH <1	PD <10	AG <.3	CD <2	IN <.4	SN <2	SB <.7	TE 5												
CS <.4	BA 1		HF <30	TA 5000	W 30	RE 5	OS <7	IR 10	PT 5	AU <.9	HG <.9	TL <.6	PB 10	BI <.6													
FR 5	RA 5	ACTINIDES-5			YH 5	U 5																					
		LA 5	CE 10	PR 5	ND 10	PM 5	SM 5	EU 5	GD 5	TB 5	DY 5	HO 5	ER 5	TM 5	YB 5												
<p>SUMMARY DATA-NOTE THAT VALUES ARE ROUNDED TO 2 SIGNIFICANT DIGITS IN SUMMARY REGARDLESS OF PRECISION-EXCEPT FOR 10 HIGHEST IMP.</p> <p>TOTAL CONCENTRATION OF ELEMENTS IDENTIFIED = 9200</p> <p>TOTAL CONCENTRATION OF ELEMENTS AS UPPER LIMIT = 22300</p> <p>CONCENTRATION OF ELEMENTS IDENTIFIED/UPPER LIMIT FOR GROUPS :</p>																											
IA 40	IIA 130	IIIA <20	IVA <1000	VA 5000	VIA 30	VIIA 50	VIII 520	IB 30	IIB 13	IIIB 200	IVB 2700	VB 200	VIB 300	VIIIB 70	0 <610												
<430	<3.6	<20	<1000	<29	<21	<4.8	<35	<1.2	<2.5	<2.9	<6.9	<20	<7.3	<2.1													
<p>TEN HIGHEST IMPORTANCES</p> <p>HIGHEST RARE EARTHS ARE : 1 ND 130 2 CE 10</p>																											
<p>ANALYST : <i>Robert J. Longinus</i></p> <p>REMARKS : PLATE # 2476C</p> <p><i>Significant detection survey</i></p> <p><i>The following elements should be considered upper limits due to the Nb probe contribution</i></p> <p><i>V, Cr, Cl, C, O, F, Mg, Al, Fe, Cu, Ta, Fe, Zn</i></p>																											
<p>PEOPLE INPUTS: CLARENCE NESS CATHY BRUNSTING BOB CONZENIUS</p> <p>HOURS: 5</p>																											

### C. Results of the Nonexponential Spin-lattice Relaxation Analysis

Here the results of computer optimized (179) least squares fitting the nonexponential NMR spin-lattice relaxation data are presented. The magnetization recovery data for each lattice temperature has been fit assuming only two distinct spin temperatures, Eq. 75. Due to low signal-to-noise ratios, the results from the fits for the 4% H sample are not presented. Except for anomalous structure in the 17% H results at approximately 100 K, the results may be very tentatively interpreted in terms of the interplay between the two types of relaxation mechanisms: the "hopping electrons" (section IV.A.2.c) and the "hopping protons" (section IV.A.2.d).

These results will be presented graphically in Figs. 30-33 for the 7-17% H samples; brief discussion will be given in the captions.

Fig. 30. The nonexponential spin-lattice relaxation of the 7% H a-Si(H) sample is analyzed. The vertical scale on the left is a logarithmic relaxation time scale (for  $T_{1a}$  and  $T_{1b}$ ); while, the scale on the right is a linear scale for representation of the ratio of fast relaxing spins to the total ( $R = M_{oa}/M_o$ ). The results for the  $T = 4.2$  K point (not graphed) are:  $T_{1a} = 11.4$  S,  $T_{1b} = 380$  S, and  $R = 8.8\%$ . The mild upward trend of  $T_{1a}$  ("■") around  $T \sim 100$ -300 K may indicate the presence of some of the "hopping proton" type relaxation centers that predominate in the high H concentration regime. The down turn of  $T_{1a}$  above  $\sim 300$  K and the behavior of  $T_{1b}$  is, of course, consistent with the "hopping electron" type of relaxation.



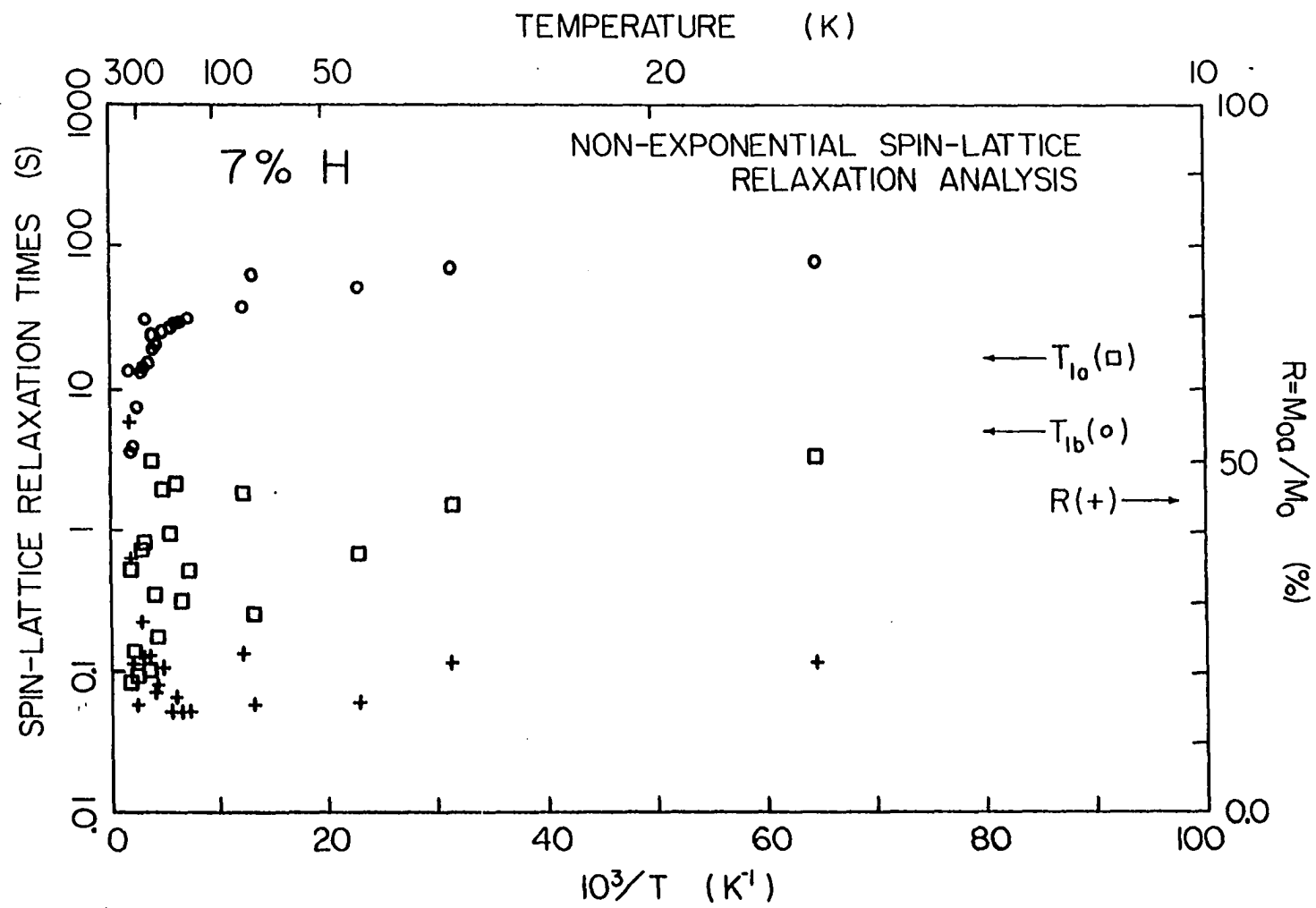


Fig. 31. The nonexponential spin-lattice relaxation of the 11% H a-Si(H) sample is analyzed. The vertical scale on the left is a logarithmic relaxation time scale (for  $T_{1a}$  and  $T_{1b}$ ); while, the scale on the right is a linear scale for representation of the ratio of fast relaxing spins to the total ( $R = M_{0a}/M_0$ ). The results for the  $T = 4.2$  K point (not graphed) are:  $T_{1a} \lesssim 0.5$  S,  $T_{1b} = 313$  S, and  $R \lesssim 9\%$ . The apparent downturn in  $T_{1a}$  at  $T \approx 100$ -300 K may be evidence for the existence of "hopping electron" centers; while the behavior of  $T_{1b}$  is consistent with the "hopping proton" type of relaxation

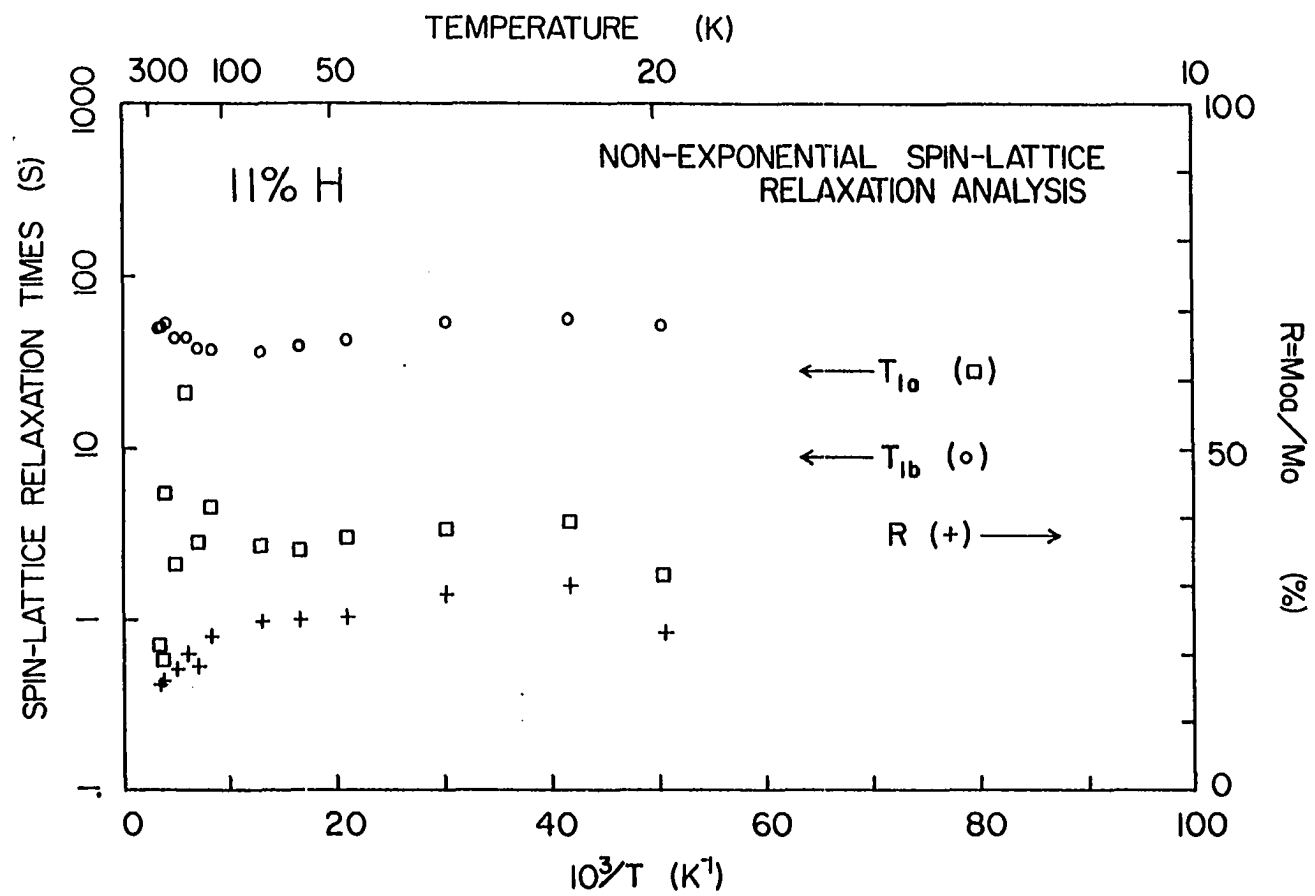


Fig. 32. The nonexponential spin-lattice relaxation for the 14% H sample is analyzed. The vertical scale on the left is a logarithmic relaxation time scale (for  $T_{1a}$  and  $T_{1b}$ ); while, the scale on the right is a linear scale for representation of the ratio of fast relaxing spins to the total ( $R = M_{0a}/M_0$ ). The results for the  $T = 4.2$  K point (not shown) are:  $T_{1a} = 2.0$  S,  $T_{1b} = 33$  S, and  $R = 7.5\%$ . Here there is no apparent downturn in  $T_{1a}$  at higher temperatures (as was the case in Fig. 31). Both  $T_{1a}$  and  $T_{1b}$  appear to be consistent with the "hopping proton model"

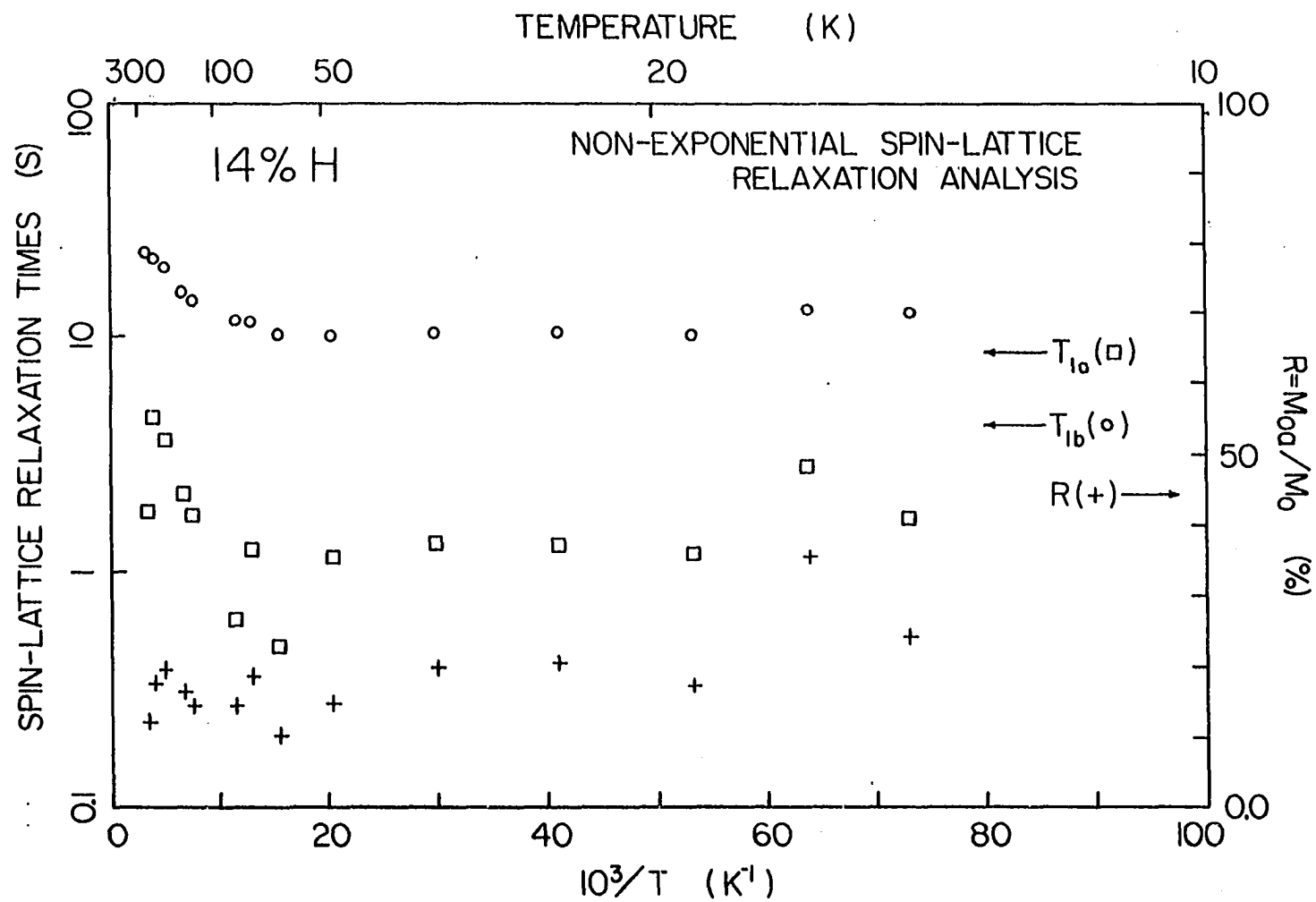


Fig. 33. The nonexponential spin-lattice relaxation for the 17% H sample is analyzed. The vertical scale on the left is a logarithmic relaxation time scale (for  $T_{1a}$  and  $T_{1b}$ ); while, the scale on the right is a linear scale for representation of the ratio of fast relaxing spins to the total ( $R = M_{0a}/M_0$ ). The results for the  $T = 4.2$  K (not shown) are:  $T_{1a} = 1.1$  S,  $T_{1b} = 6.5$  S, and  $R = 19\%$ . Here there appears to be some anomalous structure in the form of a minimum in  $T_{1a}$  and  $R$  at  $T \approx 100$  K. Could this reflect some structure in the phonon density of states?

